Third Harmonic Generation in

Liquid Core Optical Fibres

Dissertation

for the acquisition of the academic title

Doctor rerum naturalium (Dr. rer. nat.)

submitted to the council of the

Faculty of Physics and Astronomy

of the

FRIEDRICH-SCHILLER-
UNIVERSITÄT
JENA

by M.Sc. Kay Schaarschmidt

born in Karl-Marx-Stadt, Germany, on October 6th in 1988

Reviewers:

1. Prof. Dr. Markus A. Schmidt, Jena

2. Dr. Falk Eilenberger, Jena

3. Dr. Micheal H. Frosz, Erlangen

Day of disputation: 07.07.2022

Abstract

The objective of this thesis is to investigate third harmonic generation in liquid core fibres. Such fibres are formed by injection of liquid into a hollow, solid cladding by capillary forces. Carbon disulphide and tetrachloroethylene are identified as most promising liquid candidates. Such liquids offer a strong nonlinearity whose major contribution is non-instantaneous arising from the molecular structure. The effect of this material response during harmonic generation is investigated numerically by solving coupled evolution equations and causes distinct spectral shifts and broadening of both harmonic and fundamental wave.

Both liquids offer excellent transparency and a high index of refraction enabling intermodal phase matching in a step-index geometry without requiring a complex microstructure. Aspects of fibre design and experimental realisation are presented in detail. Using sub-picosecond pump pulses of different duration the harmonic is generated in a higher order fibre mode and resulting signals are analysed in the spectral domain.

Modification of the fibre cross-section towards an elliptical core is investigated. Besides the induced birefringence, harmonic generation in further sets of higher order modes is possible due to their transformation of electric fields. Design considerations of spatially modified fibres were confirmed experimentally and adaptive phase matching by controlling fibre temperature could be realised.

Feasibility of long term exposure of liquid filled fibres to high average powers of femtosecond pulses is demonstrated underpinning that liquid core fibres withstand practical applications beyond laboratory use.

Finally, possible routes to enhance the currently achieved conversion efficiencies for tetrachloroethylen of $2 \cdot 10^{-5}$, and carbon disulphide of 10^{-7}, are identified and future prospects of this fibre platform are discussed.

Deutsche Zusammenfassung

Gegenstand dieser Arbeit sind Flüssigkernfasern zur nichtlinearen Erzeugung der dritten Harmonischen durch intensive Pumppulse. Diese Fasern bestehen aus einem festen Mantel und einer durch Kapillarkräfte eingebrachten Flüssigkeit. Als vielversprechendste Kandidaten wurden Kohlenstoffdisulfid und Tetrachloroethylen näher betrachtet. Ein großer Anteil der hohen Nichtlinearität hat seinen Ursprung in der molekularen Struktur und führt zu einer nicht-instantanen Materialantwort. Der Einfluss dieser wird mittels numerischer Simulationen von gekoppelten Schrödinger Gleichungen untersucht und zeigt sich unter anderem durch spektrale Verschiebung und Verbreiterung während der Propagation beider Wellen.

Beide Flüssigkeiten bieten neben hervorragender Transparenz einen hohen Brechungsindex um die Bedingungen zur Phasenanpassung für intermodale Frequenzkonversion in Stufenindex Fasern ohne Mikrostrukturierung zu erfüllen. Das Design der Fasern ist im Detail beschrieben und wird erstmalig experimentell umgesetzt. Mittels verschiedener Pulsdauern wird die Harmonische in Moden höherer Ordnung erzeugt und die resultierenden Spektren beider Wellen analysiert.

Weiterführend wird die Modifikation der Fasergeometrie hin zu einem elliptischen Kern beschrieben. Neben doppelbrechenden Eigenschaften konnte so die Kopplung zu weiteren Moden durch Transformation der elektrischen Felder erhöht und experimentell bestätigt werden. Die grundlegende Möglichkeit zur adaptiven Phasenanpassung durch aktive Temperatursteuerung der Faser wird aufgezeigt.

Langzeitversuche mit hohen Durchschnittspumpleistungen konnten im Rahmen der Arbeit zudem die Beständigkeit von Flüssigkernfasern für Anwendungen über den Laboreinsatz hinaus bekräftigen.

Abschließend werden Ansätze zur Verbesserung der Konversionseffizienz, die im Falle von Tetrachloroethylen im Bereich um $2 \cdot 10^{-5}$ und im Falle von Kohlenstoffdisulfid bei 10^{-7} liegt, in Aussicht gestellt.

List of Abbreviations

AD	anomalous dispersion
CDS	carbon disulphide, CS_2
eLCF	elliptical liquid core fibre
FWHM	full width at half maximum
FOD	fourth order dispersion
GDD	group delay dispersion
GVD	group velocity dispersion
GVM	group velocity mismatch
HOM	higher order mode
IOR	index of refraction
LCF	liquid core fibre
MFD	modefield diameter
ND	normal dispersion
NLP	nonlinear phase
PM	phase matching, phase matched
ROP	ratio of polarisation
SIF	step-index fibre
SPM	self-phase modulation
TCE	tetrachloroethylene, C_2Cl_4
TH	third harmonic
THG	third harmonic generation
TOC	thermo optical coefficient
TOD	third order dispersion
XPM	cross-phase modulation
ZDW	zero dispersion wavelength

List of Symbols

f_R	molecular fraction		β	propagation constant
J_i	i^{th} modal overlap integral		β_i	i^{th} expansion coefficient of β
L_c	coherence length		$\Delta\beta$	phase mismatch
L_D	dispersive length		η	efficiency
L_w	walk-off length		λ_0	central wavelength of pump
N	soliton number		λ_{PM}	phase matched wavelength
NA	numerical aperture		$\delta\lambda_{\text{THG}}$	wavelength offset from $\lambda_0/3$
R	response function		λ_{ZD}	zero dispersion wavelength
T_0	pulse width		ω_0	central frequency of pump
V	fibre parameter		Ω	detuning from $3\omega_0$

List of Figures

List of Tables

Content

1   Introduction

Third harmonic generation (THG) is a nonlinear process allowing conversion of a fundamental wave to three times its original frequency. It can be applied to convert intense laser pulses from near infrared to visible and ultraviolet radiation [1] or temporal switching [2]. In nonlinear microscopy interfaces of transparent media can be detected [3] and multimodal imaging [4] benefits from the THG process. Although diverse in application, substantial signal yield requires high intensities and in bulk media large pulse energies are in demand. Since high performance lasers are costly, waveguides, and fibres in particular, became an indispensible tool making nonlinear optics accessible at moderate energy levels. Transverse field confinement to the scale of the radiation wavelength allows for sufficient intensities and can crucially extend interaction lengths far beyond typical dimensions of nonlinear crystals or the confocal length of a focused beam.

However, THG is a phase sensitive process and exploiting fibre length is possible only if phase velocities of fundamental and harmonic wave are identical, i.e. if material dispersion is compensated. Since fibres are typically made from isotropic media, phase matching (PM) techniques known from crystal optics [5] need to be adapted. Here, higher order modes (HOMs) guided at the harmonic exhibit reduced phase velocity enabling PM to the pump wave which is typically guided in the fundamental mode.

To this end, a sufficient index contrast between core and cladding must be present to make intermodal PM possible. With the introduction of microstructured optical fibres (MOFs), numerous demonstrations of THG in MOFs [6] showed HOMs in the visible [7,8] and ultraviolet [9] in early 2000. Simultaneously, silica micro fibres, so called tapers, were investigated experimentally [10,11] and theoretically in detail [12] as well as the propagation dynamics of THG [13,14].

The conversion efficiency serves as sizable benchmark to assess performance in THG. For ultra-short pulses in the femtosecond regime the efficiency is typically of the order of 10^{-4} in silica tapers [10,15] and in MOF [16]. Highly GeO_2-doped fibres achieved efficiencies of $3 \cdot 10^{-7}$ thus far [17]. Despite efficiencies of up to 10^{-3} reported already in early work of MOFs, the modal shape with multiple lobes makes it difficult to further utilise the radiation other than in free space. Still, applications towards fluorescence sensing were demonstrated [18] and the trend towards multi-wavelength output from a

single fibre persists as a range of 300 nm was covered by more than 10 simultaneous modes in 2020 [19] in a MOF with suspended core. Thus THG in fibres holds potential for image guided surgery [20] or multiplexed fluorescence lifetime spectroscopy [21].

Upon proposing fibres to become a future source of correlated three photon states [22–24] in 2011, research interest in THG was renewed as it is the inverse process sharing the same PM conditions. THG in non-uniform tapers [15], taper knot-resonators [25], and silica fibres with highly GeO_2-doped cores followed [17,26]. MOF with exposed cores [16,27] addressed post processing PM via nano-film deposition and tuning via control of ambient gas pressure was demonstrated for tapers in 2018 [28] to compensate for manufacturing inaccuracy.

Since generation of correlated photons requires launching a pump in a HOM for existing fibre structures, efforts were taken to achieve conversion among single lobed modes; to this end, an advanced, multi-component photonic crystal fibre structure was demonstrated in 2016 [29]. The drawing process is very demanding to meet the required dimensions since tuning capabilities in silica based fibres are limited. Other work proposed conversion by counter propagating pulses [30]. THG in a fundamental mode of a taper was just demonstrated experimentally [31] in 2021 by means of acousto-optic mode conversion highlighting the on-going trend in the field.

Considering the requirements for THG for both classical and non-classical regimes, an optimal fibre must provide means to achieve phase matching, offer sufficiently large nonlinearity, be tuneable ideally during operation, and be compatible with fibre packaging for convenience. Mechanical strength and straight forward manufacturing are desirable for wide spread use. Interfacing to standard single mode fibres can be accomplished by both pigtailed tapers and fibres with high GeO_2 concentration via simple fibre splices. Yet, tapers usually require diameters below $1\,\mu m$ for PM compromising mechanical strength, handling, and are susceptible to surface roughness [32], whereas highly GeO_2-doped fibres are limited by the low bulk nonlinearity of silica.

A fibre platform with potential of combining the aforementioned virtues is represented by liquid core fibres (LCFs) as argued hereafter. The replacement of silica in the core by a liquid allows introducing a greater nonlinearity to the fibre and at the same time maintains its mechanical integrity due to the silica cladding which may have standard sizes of $125\,\mu m$. Accurate models for dispersion [33] and nonlinearity [34,35] enabled convincing experimental progress in, e.g. supercontinuum generation in liquid

filled step-index fibres [36–42] and liquid filled MOFs [43–46] in both the normal and anomalous dispersive domain. LCFs provide adequate tuning potential due to their large thermo-optical coefficient [47]. Successful dispersion tuning in a LCF during operation by controlling temperature was already demonstrated [40] as well as reconfiguration of the core material by mixtures [41,42]. Further, molecular liquids exhibit a non-instantaneous nonlinear response due to orientational effects leading to new pulse dynamics [48,49] and enhanced stability in continuum generation [38,50]. Due to the temporal extent, the bandwidth of the liquid response is much lower than in silica and photon pair generation in LCFs was recently shown to mitigate noise from uncorrelated photons while still operating at room temperature [51,52].

A large number of fully integrated liquid photonic applications, combining light and liquid [53], were demonstrated for continuum [36,37] and Raman comb generation [54,55], Kerr cells [56], and integrated dye lasers [57]. Handling of LCF can hence be considered no more complex than the use of mechanically less robust softglass, chalcogenide glass, or sub-micron tapers made from silica, particularly since techniques to apply standard splice technology to LCFs already exist [58].

In view of this potential, LCFs are explored in this thesis as a new platform for THG from the experimental perspective supported by numerical simulations.

The central scientific aspects of this thesis are as follows:

- In what way is the molecular response involved in the generation of harmonics and the interaction during propagation?

- Can combinations of core fluids and fibre dimensions be selected to successfully realise THG?

- How efficient is THG in liquid core fibres in comparison to existing solutions?

- How does form birefringence affect the participating modes in THG?

- Can temperature modulation be used as tuning mechanism?

- Can long-term stability be achieved in LCF?

1.1 Structure of the Thesis

Following the introduction in chapter 1, the 2nd chapter presents the principles of waveguiding in circular step-index geometries such as liquid filled fibres and provides the tools for pulse propagation in the nonlinear regime. Functional forms of the retarded responses are provided and their contribution to the nonlinear refractive index is discussed. Theoretical aspects of phase matching and how to design waveguides to achieve intermodal third harmonic generation are summarised at the end of chapter 2.

Chapter 3 provides an overview of nonlinear pulse propagation with the focus on studying the particular effects of the molecular contribution to the nonlinearity via both self and cross phase modulation. Thereafter coupled evolution dynamics for a pump and generated harmonic wave are presented and experimental conditions are assessed.

Chapter 4 begins with selecting suitable liquids for harmonic generation in silica cladding fibres. Further, details of phase matching and waveguide design are presented and followed by experimental results. Those include harmonic generation in C_2Cl_4 and CS_2 filled fibres for different pulse durations serving as pump pulse. Spatial modifications leading to birefringence are considered and executed experimentally. Aspects of temperature tuning are illustrated and experimental evidence of their potential is presented. The chapter closes with a demonstration of power handling capabilities of these fibres.

In chapter 5 the work is summarised and possibilities for further efficiency improvement are provided and potential applications are discussed.

2 Nonlinear Wave Propagation in Dielectric Waveguides

In this chapter a compact introduction to the fundamentals of nonlinear wave propagation and third harmonic generation (THG) in dielectric waveguides is presented. Extensive derivations are largely omitted and can be reviewed in the literature cited in each subchapter.

2.1 From Maxwell's equations to an eigenvalue problem

The fundamental equations of classical electrodynamics are Maxwell's equations. If dielectrics at optical frequencies are considered, it is assumed that neither free charges nor free currents are relevant. Moreover, dielectrics are assumed to have a negligible magnetization at optical frequencies. Hence Maxwell's equations in time domain read:

$$\nabla \times \boldsymbol{E} = -\frac{\partial \boldsymbol{B}}{\partial t} \qquad\qquad \nabla \times \boldsymbol{H} = \frac{\partial \boldsymbol{D}}{\partial t} \tag{1}$$

$$\nabla \cdot \boldsymbol{D} = 0 \qquad\qquad \nabla \cdot \boldsymbol{B} = 0 \tag{2}$$

$$\boldsymbol{D} = \varepsilon_0 \boldsymbol{E} + \boldsymbol{P} \qquad\qquad \boldsymbol{B} = \mu_0 \boldsymbol{H} \tag{3}$$

Arguments are suppressed for clarity. Vectorial quantities are printed in bold letters. $\boldsymbol{E}$ and $\boldsymbol{H}$ are the electric and magnetic field, respectively, while $\boldsymbol{D}$ and $\boldsymbol{B}$ are the electric displacement current and the magnetic induction. $\nabla = \boldsymbol{e}_x \partial_x + \boldsymbol{e}_y \partial_y + \boldsymbol{e}_z \partial_z$ is the Nabla operator, ε_0 and μ_0 are the free space dielectric and magnetic permeability, and $\boldsymbol{e}_{\sim}$ represent Cartesian unit vectors. The polarization of a material is defined by the field $\boldsymbol{P}$, which contains linear and nonlinear phenomena via $\boldsymbol{P}_L$ and $\boldsymbol{P}_{NL}$.

$$\boldsymbol{P} = \boldsymbol{P}_L + \boldsymbol{P}_{NL} \tag{4}$$

The polarization of the material is described as a function of the driving electric field $\boldsymbol{E}$ and the inherent properties of the material itself. It is customary to expand this dependence in a power series with respect to $\widetilde{\boldsymbol{E}}$ in the frequency domain [59].

$$\tilde{P}_i = \varepsilon_0 \left(\underbrace{\chi_{ij}^{(1)} \tilde{E}_j}_{\text{linear}} + \underbrace{\chi_{ijk}^{(2)} \tilde{E}_j \tilde{E}_k + \chi_{ijkl}^{(3)} \tilde{E}_j \tilde{E}_k \tilde{E}_l + \cdots}_{\text{nonlinear}} \right) \tag{5}$$

Note that summation for recurrent indices is implicit. The first term describes linear interactions in a possibly anisotropic medium where the electric and polarization fields are not necessarily parallel. The second term describes nonlinear interactions of second order, e.g. second harmonic generation, sum and difference frequency generation. The third term is responsible for THG and intensity dependent refractive index changes.

Descriptions of these and higher rank tensors can be found in [60,61]. In general, every n^{th} order effect is described by the mixing of n fields via a tensor of rank $n + 1$.

In a homogenous dielectric a nonlinear wave equation can be obtained from Maxwell's curl equations for $\widetilde{\boldsymbol{E}}$ in frequency space

$$\nabla^2 \widetilde{\boldsymbol{E}} + \frac{n^2 \omega^2}{c_0^2} \widetilde{\boldsymbol{E}} = -\omega^2 \mu_0 \widetilde{\boldsymbol{P}}_{NL}, \tag{6}$$

where the index of refraction (IOR) was introduced as $n^2(\omega) = 1 + \chi^{(1)}(\omega)$ for isotropic media, such as glasses or liquids. c_0 is the velocity of light in vacuum. The solution procedure closely follows [62]. Due to the four Maxwell's equations, only two of the six field components of $\widetilde{\boldsymbol{E}}$ and $\widetilde{\boldsymbol{H}}$ are independent and Eq. (6) can be treated as a scalar equation for both $\widetilde{E_z}$ and $\widetilde{H_z}$. Since the change of the IOR due to intensity is assumed small[1], the nonlinear polarisation can be neglected at first and the problem may be separated by an ansatz of the form

$$\widetilde{E_z}(x, y, z, \omega - \omega_0) = F(x, y)\tilde{A}(z, \omega - \omega_0) \exp(i\beta_0 z), \tag{7}$$

with an arbitrary β_0, which leads to two separate equations

$$\left(\frac{\partial^2}{\partial x^2} + \frac{\partial^2}{\partial y^2} \right) F + n^2 k_0^2 F - \beta^2 F = 0 \tag{8}$$

$$\frac{\partial^2}{\partial z^2} \tilde{A} + 2i\beta_0 \frac{\partial}{\partial z} \tilde{A} + (\beta^2 - \beta_0^2)\tilde{A} = 0. \tag{9}$$

Note that, mathematically, β^2 represents a separation constant, its physical meaning is evident due to the dispersion relation presented in chapter 2.2. $k_0 = \omega_0 c_0^{-1}$ was introduced as vacuum wavenumber. To solve Eq. (8) it is customary to use polar coordinates and the ansatz $F(\rho, \varphi) = f(\rho) \cos(m\varphi + \varphi_0)$ which leads to Bessel's differential equation for the radial part [62] within the core and cladding domain. Maxwell equations are used to derive the remaining field components and upon imposing the boundary conditions for tangential fields the dispersion relation results as solvability condition for the linear algebraic system [63].

---

[1] Example of CS_2 in 3 μm core for 50 kW pulses: $\Delta n/n < 10^{-3}$

2.2 Guided Modes in Cylindrical Waveguides

Cylindrical waveguides, i.e. fibres, are of key importance in this thesis and a prominent platform for nonlinear optics providing long interaction lengths combined with strong localisation of electromagnetic fields. The shapes of these fields, also termed modes, are obtained from the eigenvalue problem given in, Eq. (8). There is a plethora of different fibres currently available, many of which require special numerical treatment to solve for modes and the respective propagation constants. Here, simple step-index fibres (SIF) are considered as implemented experimentally. Fig. 1 (a) presents a schematic of a SIF with a selection of guided modes (b) obtained by solving the eigenvalue problem. Each sub-panel shows the intensity distribution and electric field vectors. The standard nomenclature for hybrid and transverse modes is used with two indices. The first index corresponds to the azimuthal field dependence and occurs in the dispersion relation in Eq. (10) as m and can take integer values including zero. The second index is counting the number of guided modes for a particular type of mode and index m. Only modes of type HE_{mn} (including the fundamental mode HE_{11}) which show a central intensity lobe will be of interest for frequency conversion as discussed in section 2.4.3.
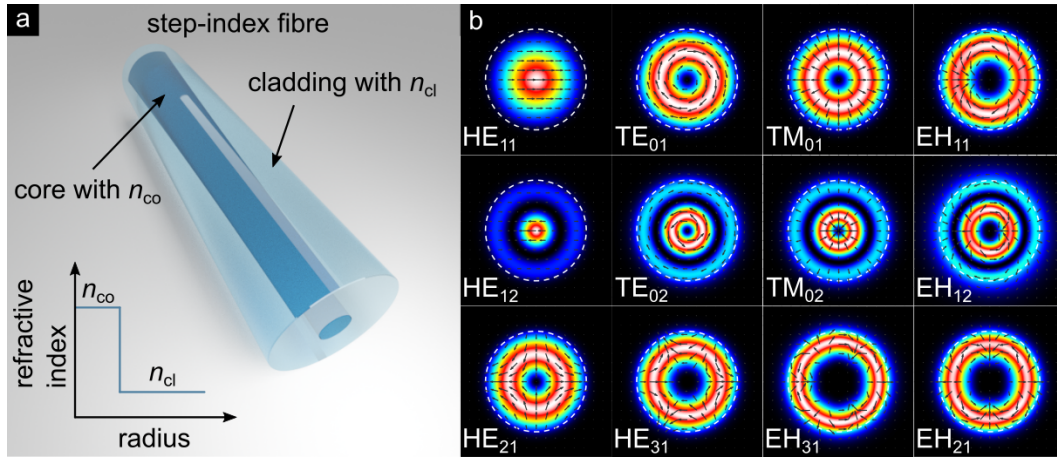
Fig. 1: (a) Step-index fibre with schematic profile of refractive index. (b) Selection of intensity profiles with electric field vectors for guided modes of hybrid type (HE_{mn} and EH_{mn}) and transverse type (TE_{0n} and TM_{0n}). Dashed circle represents the core. Fibre parameters: $n_{cl} = 1.45, n_{co} = 1.458, r_{co}/\lambda = 4$.

In free space a simple dispersion relation $k(\omega) = n(\omega)\omega c_0^{-1}$ can be obtained using a plane wave ansatz for Eq. (8). Here, k is the wavenumber that corresponds to the propagation constant in free space and c_0 is the speed of light in vacuum. For the case of fibres, Eq. (8) can be solved in polar coordinates, which is a known procedure. Explicit details are found in the respective chapters of [63–65]. Here, only the transcendental

dispersion relation for modes is given using the notation of [64], due to its importance to determine dispersive properties of fibre waveguides:

$$\left[\frac{\mathcal{J}'_m(U)}{U\mathcal{J}_m(U)} + \frac{\mathcal{K}'_m(W)}{W\mathcal{K}_m(W)}\right]\left[\frac{\mathcal{J}'_m(U)}{U\mathcal{J}_m(U)} + \frac{n^2_{cl}}{n^2_{co}}\frac{\mathcal{K}'_m(W)}{W\mathcal{K}_m(W)}\right] = \left[\frac{m\beta}{k_0 n_{co}}\right]^2\left[\frac{V}{UW}\right]^4 \qquad (10)$$

$\mathcal{J}_m$ and $\mathcal{K}_m$ represent Bessel functions of order m for the core and cladding regions such that the fields obey physical boundary conditions. The prime indicates a derivative with respect to the argument. n_{co} and n_{cl} are the core and cladding IOR. The parameters $U = r_{co}(n^2_{co}k^2_0 - \beta^2)^{1/2}$ and $W = r_{co}(\beta^2 - n^2_{cl}k^2_0)^{1/2}$ depend on the propagation constant β and the core radius r_{co}. The normalized frequency, or *V-parameter*, is given as $V = \sqrt{U^2 + W^2} = r_c k_0 NA$, where the *numerical aperture* was introduced as $NA = \sqrt{n^2_{co} - n^2_{cl}}$. Due to its complexity, Eq. (10) is solved numerically by root search algorithms to determine $\beta(\omega)$, subsequently the modal fields can be calculated. The procedure is explained in detail in chapter 5 of [63], explicit formulas for the vectorial field distribution $\boldsymbol{F}$ in SIF can be found on page 250 of [64].

Since $\beta(\omega)$ has no analytic form, its Taylor expansion

$$\beta(\omega) = \sum_{n=0}^{\infty}\frac{1}{n!}\beta_n \cdot (\omega - \omega_0)^n \quad \text{with } \beta_n = \left.\frac{\partial^n\beta}{\partial\omega^n}\right|_{\omega_0} \qquad (11)$$

at a reference frequency ω_0 is commonly employed and its relevance is apparent in Eq. (15) in the following subsection.

2.3 Nonlinear Pulse Propagation

Nonlinear pulse propagation is a long standing problem and many procedures emerged to provide means to solve for the field under a variety of conditions. Comprehensive reviews are found in [66–68] but are beyond the scope of this thesis. Here, the focus is on the generalised nonlinear Schrödinger equation (GNLSE) that proved successful in modelling experiments, see e.g. the review articles focussed on supercontinuum generation (SCG) in fibres [69,70]. A perturbative approach to derive the GNLSE closely follows [62].

To obtain the GNLSE the following assumptions are made and applied to Eq. (9):

- $\frac{\partial^2 \tilde{A}}{\partial z^2} \ll \beta_0 \frac{\partial \tilde{A}}{\partial z}$ and $\beta^2 - \beta_0^2 \cong 2\beta_0(\beta - \beta_0)$

Whereas the former represents the slowly varying amplitude approximation, the latter simplification assumes negligible backward waves in analogy to the derivation of forward Maxwell equations [68,71].

Following the perturbation approach from [62], the IOR and eigenvalues found from Eq. (10) are modified as follows:

$$n^2 \Rightarrow (n + \Delta n)^2 \approx n^2 + 2n\Delta n$$

$$\beta^2 \Rightarrow (\beta + \Delta\beta)^2 \approx \beta^2 + 2\beta\Delta\beta \tag{12}$$

and Eq. (8) is used to obtain

$$\Delta\beta(\omega) = \frac{\omega^2 n(\omega)}{c_0^2 \beta(\omega)} \frac{\iint_{-\infty}^{\infty} \Delta n(\omega)|F(x,y)|^2 dxdy}{\iint_{-\infty}^{\infty} |F(x,y)|^2 dxdy}. \tag{13}$$

Eq. (9) finally reads

$$\partial_z \tilde{A} = \mathrm{i}[\beta(\omega) + \Delta\beta(\omega) - \beta_0]\tilde{A}. \tag{14}$$

After expanding both β and $\Delta\beta$ in their respective Taylor series up to the desired order the transfer to the temporal domain yields the GNLSE in SI units used to model the evolution of a linearly polarised field with amplitude $A(z,t)$ and reads [62,69]:

$$\partial_z A = \mathrm{i} \sum_{n \geq 1} \mathrm{i}^n \frac{\beta_n}{n!} \partial_t^n A - \frac{\alpha}{2} A + \mathrm{i}\kappa A(1 + \mathrm{i}\tau_s \partial_t)\{\mathcal{R} * |A|^2\} \tag{15}$$

$A(z,t)$ is scaled in $\sqrt{W}$, α is the linear absorption coefficient in m⁻¹, and $\kappa = k_0/a_{\mathrm{eff}}$ represents the nonlinear parameter[2] of the fibre in units of m⁻³. This parameter crucially depends on material and waveguide properties due to the effective area, a_{eff}. The contribution due to the field distribution is discussed in chapter 2.4.3 p. 15 and the shock constant, τ_s, accounts for the dispersion of the nonlinearity which, in first order approximation, is equal to ω_0^{-1} of the pump field. Higher order correction terms may be included [72]. In [73] a general approach to account for dispersion of nonlinearity was introduced to meet the requirements for simulating an ultra-wide supercontinuum (SC),

---

[2] The standard nonlinear parameter is defined as $\gamma = \kappa n_2$ in W⁻¹/m, above n_2 is contained in $\mathcal{R}(t)$.

but is not of relevance for this thesis. The response $\mathcal{R}$ is detailed in the next subchapter and $*$ denotes a convolution.

Dispersion is represented by the coefficients β_n according to Eq. (11). Here, β_2 is of key importance and termed *group velocity dispersion* (GVD). In a purely linear regime, GVD causes pulses to broaden temporally as different spectral components aquire different delays with respect to the pulse centre. Further, parameter is used to distinguish two different propagation regimes, namely the normal dispersive (ND) domain for $\beta_2 > 0$, and the anomalous dispersive (AD) domain for $\beta_2 < 0$. Both give rise to complex, yet very different propagation dynamics when accompanied by nonlinearity. The interested reader is referred to excellent review articles [69,70,74] and text books on that matter [75–77].

Different schemes to numerically solve Eq. (15) were introduced and are detailed in [62,78–81]. A standard technique is the Fourier split step method which treats the linear and nonlinear terms separately in frequency and time domain, respectively.

Eq. (15) may be written in normalised units which is convenient for theoretical considerations and advantageous in numerical simulations. The procedure closely follows [82].

$$\partial_\xi U = \mathrm{i} \sum_{n \geq 2} \mathrm{i}^n \delta_n \partial_\tau^n U + \mathrm{i} N^2 U (1 + \mathrm{i} s \partial_\tau)(|U|^2 + h * |U|^2) \tag{16}$$

To obtain Eq. (16), a characteristic time, T_0, i.e. the pulse width, and dispersive length $L_D = T_0^2/|\beta_2|$ were introduced to scale propagation distance $\xi = z/L_D$ and co-moving time $\tau = (t - \beta_1 z)/T_0$. Dispersion parameters are given as $\delta_n = \beta_n/(n!\,T^{n-2}|\beta_2|)$, the amplitude $U = A/\sqrt{P_0}$ is scaled by the peak power, and $N = \sqrt{L_D n_{2,el} \kappa P_0}$ is the soliton number, defined by the electronic nonlinear IOR [83]. Its purpose is to measure the relative strength of dispersion and nonlinearity regardless of the dispersive domain. Shock is included by the parameter $s = (\omega_0 T_0)^{-1}$ and h represents a scaled version of the non-instantaneous contributions which are detailed in Eq. (20), p. 11.

Despite the generality of the normalisation procedure, characteristic scales to be deployed must be consistent with the physical problem at hand.

2.3.1 Nonlinear Response with Retardation

Except for mono-atomic gasses, the nonlinear material response consists of two constituents – the electronic effect which is instantaneous, and non-instantaneous, i.e. retarded, effects. Such effects originate from molecular vibrations (i.e. the *Raman* effect) and reorientational effects in molecular liquids, which are of central interest in this thesis. The total response, as shown in Eq. (15), is given as

$$\mathcal{R} = n_{2,el}\delta(t) + R(t), \tag{17}$$

where $n_{2,el}$ is the nonlinear IOR due to the *electronic Kerr effect* and $R(t)$ is a material specific retarded response. The time dependent nonlinear change of IOR reads [84]

$$\Delta n(z,t) = n_{2,el}I(z,t) + \int_0^\infty R(\tau)I(z,t-\tau)d\tau \tag{18}$$

and is a measure of how much a beam modulates its own, or another beams, phase during propagation. The nonlinear phase (NLP) is defined as

$$\Phi_{\text{NL}}(z,t) = \Delta n(z,t)k_0 z, \tag{19}$$

which leads to so called *self-phase modulation* (SPM) as well as *cross phase modulation* (XPM) and to the generation of new frequencies [85]. The intensity in the waveguide is defined via the amplitude and effective area: $I = |A|^2/a_{\text{eff}}$. The retarded response $R(t)$ can consist of multiple contributions, particularly in the case of molecular liquids. It is customary to assume all contributions are independent from each other [34,35,84], hence $R(t)$ can be written as superposition

$$R(t) = \sum_k n_{2,k}r_k(t). \tag{20}$$

Each effect contributes with its respective strength $n_{2,k}$ and temporal shape $r_k(t)$ which is normalised such that $\int r_k(t)dt = 1$. Generally, any response component, due to causality, fulfils the condition $r(t < 0) = 0$. It is to note that this approach is general and also applies to single component responses, such as the *Raman* response in silica that is often modelled by a single oscillator. An overview of response functions and their respective applications in modelling physical processes is given in Table 1. Note, further response functions were introduced, yet they rather serve the purpose of simplifying the response and reducing the number of model parameters required to reproduce material properties, as they do not originate from first principles. A simple exponential decay [48,50] was employed, as well as a generalised response [86] which allows to reproduce

the physical models qualitatively well with a single parameter. An extensive overview of model parameters for reorientational responses in liquids is presented in [34,35,87,88] as well as a detailed description of the beam deflection technique allowing the experimental retrieval of parameters.

Table 1: Overview of physically motivated retarded response functions $r(t)$. τ_r and τ_f are rise and fall times, respectively. Constants C are chosen such that $r(t)$ is normalised.

effect	response	Ref
Raman vibration	$\dfrac{\tau_r^2 + \tau_f^2}{\tau_r \tau_f^2} \exp\left(-\dfrac{t}{\tau_f}\right) \sin\left(\dfrac{t}{\tau_r}\right)$	[89]
diffusive and dipolar reorientation	$\dfrac{\tau_r + \tau_f}{\tau_f^2}\left(1 - \exp\left(-\dfrac{t}{\tau_r}\right)\right)\exp\left(-\dfrac{t}{\tau_f}\right)$	[34,84]
libration	$C \exp\left(-\dfrac{t^2}{2\tau_f^2}\right) \sin\left(\dfrac{t}{\tau_r}\right)$	[90,91]
	$C \exp\left(-\dfrac{t}{\tau_f}\right)\displaystyle\int_0^\infty \dfrac{\sin(\omega t)}{\omega} g(\omega)d\omega$, with $g(\omega) = \exp\left(-\dfrac{(\omega - \omega_0)^2}{2\sigma^2}\right) - \exp\left(-\dfrac{(\omega + \omega_0)^2}{2\sigma^2}\right)$	[34,92]

According to Table 1, Raman vibrations in both molecules and solids can be modelled by exponentially damped sinusoids, whereas orientational effects are modelled with under damped solutions to a driven harmonic oscillator. In case of libration, which is a molecular rocking motion, two different models exist, yet both originate from the attempt to account for inhomogeneous broadening of the response.

2.3.2 Effective Nonlinear Refractive Index and Molecular Fraction

A single, effective nonlinear IOR $n_{2,\text{eff}}$ is typically preferred over numerous response function parameters to compare materials. The intensity weighted average of the nonlinear change of the IOR [93] is used to derive (see [34] for details)

$$n_{2,\text{eff}}(z) = n_{2,el} + \frac{\int I(z,t)\int R(t')I(z,t-t')dt'dt}{\int I^2(z,t)dt} \equiv n_{2,el} + \langle n_{2,R}\rangle(z). \qquad (21)$$

Just like the NLP in Eq. (18), $n_{2,\text{eff}}$ depends on the pulse shape which is subject to changes during propagation highlighted by the explicit dependence on z. Eq. (21) is used to introduce an intensity weighted nonlinear IOR due to retardation, $\langle n_{2,R}\rangle$. It is common to express non-instantaneous contributions via a retarded, i.e. molecular, fraction

$$f_R = \frac{\langle n_{2,R}\rangle}{n_{2,el} + \langle n_{2,R}\rangle}, \qquad (22)$$

which was originally introduced by Stolen *et al.* in 1989 [89] who presented an analytical model for *Raman* scattering in silica fibres (see Table 1, first row). For silica a constant value of $f_R = 0.18$ was determined via accurate experimental data at that time due to its importance in telecommunication fibres. Albeit successful in modelling, a constant f_R is only a good approximation due to the large bandwidth of R in silica, rendering it as quasi-instantaneous response. Generally, f_R depends on the pulse shape due to $n_{2,\text{eff}}$ and therefore on z. This fact however, is intrinsic to the particular form of the GNLSE presented in Eq. (15).

2.4 Third Harmonic Generation

This subchapter provides fundamentals to phase matching (PM) and modal field overlap, two prerequisites for signal generation at the third harmonic (TH) of a pump. Finally, coupled GNLSEs are introduced that serve as numerical model in chapter 3.3.

2.4.1 Phase Matching in Third Harmonic Generation

THG, in contrast to SPM and XPM, is a phase sensitive nonlinear wave mixing process and crucially depends on the propagation constants of participating modes. Coherent build-up of TH signal requires the following condition to be satisfied

$$0 = \Delta\beta = \beta^H(3\omega) - 3\beta^P(\omega) + \Delta\beta_{\text{NL}}. \tag{23}$$

Superscripts indicate the propagation constants of harmonic and pump waves and $\Delta\beta_{\text{NL}}$ accounts for NLP shifts such as SPM and XPM. If applicable, β^H and β^P are expanded in a Taylor series (see Eq. (11)) up to 1$^{\text{st}}$ order which yields

$$\Delta\beta \cong \Delta\beta_0 + GVM \cdot \Omega + \Delta\beta_{\text{NL}}, \tag{24}$$

where the group velocity mismatch (GVM) is introduced as $GVM = 1/v_g^H - 1/v_g^P$, $\Omega = 3(\omega - \omega_P)$ represents a detuning from the pump frequency ω_p that was chosen as expansion point, and $\Delta\beta_0 = \beta_0^H - 3\beta_0^P$ is the phase mismatch at ω_P. Typically, PM is not achieved at ω_p, hence a detuning of

$$\Omega = -\frac{\Delta\beta_0 + \Delta\beta_{\text{NL}}}{GVM} \tag{25}$$

is expected which depends on dispersion and the launched power due to $\Delta\beta_{\text{NL}}$, commonly defined as $\Delta\beta_{NL} = 3\kappa n_2 P$ [14] where only SPM of the pump and XPM of the

harmonic due to the pump were accounted for. Since $\partial\Omega/\partial P = -3\kappa n_2 GVM^{-1}$, the TH signal is expected to shift with increasing pump power.

2.4.2 Practical Aspects of Phase Matching in Fibres

A convenient entity in fibre optics is the effective IOR of a guided mode $n_{\text{eff}} = \beta/k_0$, which is bounded as $n_{cl} < n_{\text{ef}} < n_{co}$. In terms of PM, $n_{\text{eff}}^P = n_{\text{eff}}^H$ must be met where nonlinear dephasing was neglected. There are three requirements for sufficient THG to occur in a waveguide; i) high refractive index contrast to support higher order modes at the harmonic – since material dispersion is inevitable, the difference of IOR of the cladding at ω_p and $3\omega_p$ needs to be exceeded to support higher order modes with elevated effective IOR that cross the fundamental pump, i.e. achieve PM, before cut off, ii) compensation of material dispersion via such higher order modes, and iii) field overlap of the interacting modes – this criterion limits the number of modes that can be exploited for harmonic generation.

Fig. 2 illustrates the first two requirements exemplarily for a generic waveguide whose material dispersion is equal to that of silica. A numerical aperture of 0.3 (0.6) is chosen in Fig. 2 (a) (Fig. 2 (b)) as an example. The y-axis is referenced to the cladding index of the harmonic frequency, such that higher order modes cut off at the dashed zero line. The bottom x-axis represents the fibres V parameter at the pump frequency and the corresponding core radius is shown at the top. Solid lines represent guided modes according to their label and frequency. Corresponding intensity distributions are shown in Fig. 2 (c). Although many more modes are guided in this waveguide system, the example is restricted to only those modes that feature a central intensity peak which enables higher mode coupling efficiency than ring shaped modes (see Fig. 1 (b)). Horizontal dashes and dot-dashes represent material indices of the core and cladding for both frequencies. PM is possible only if a higher order mode enters the highlighted green area and occurs at the intersection with the fundamental mode. Since the green area is bounded by the cladding IOR at the harmonic and the fundamental pump mode which itself is bounded by the core material index, the core-cladding index contrast must exceed the difference of cladding material indices at the respective frequencies. Mathematically, the following condition needs to be met:

$$n_{co}(\omega) - n_{cl}(\omega) > n_{cl}(3\omega) - n_{cl}(\omega) \Leftrightarrow n_{co}(\omega) > n_{cl}(3\omega) \tag{26}$$

Although it is desirable to operate in the single mode regime for the pump it can be difficult to enforce phase matching inside the grey shaded area ($V(\omega) < 2.405$). Again, the presentation of modes is restricted to HE type modes.
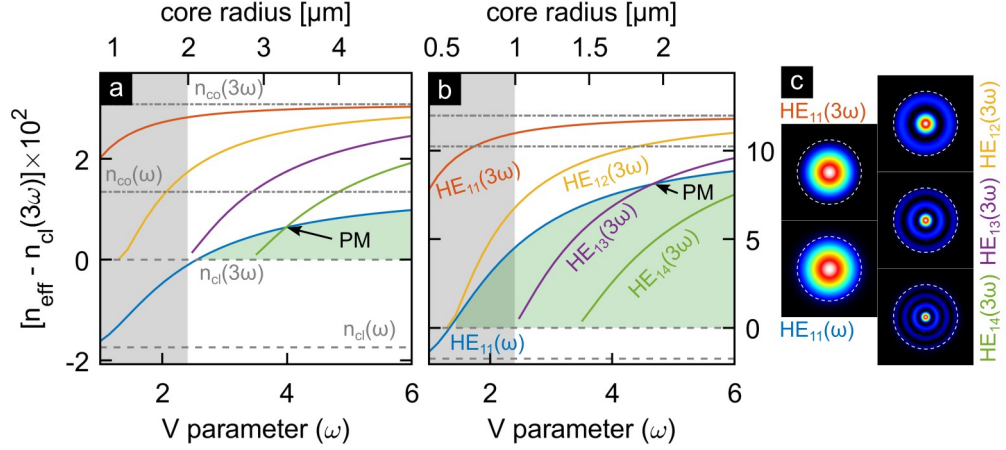
Fig. 2: Modal dispersion in step index fibre referenced to cladding refractive index at the harmonic frequency. (a) NA of 0.3, (b) NA of 0.6. Horizontal dashed (dot-dashed) lines represent cladding (core) refractive index. The upper (lower) lines correspond to the harmonic (pump) frequency. Higher order modes cut off at the dashed zero line. Phase matching is possible only if the cut off occurs within the green area – after intersecting the fundamental pump mode (blue). The grey area represents the single mode regime for the pump. (c) shows normalised modal intensity distribution according to the labels in (b). The dashed circle indicates the core size of the step index fibre.

2.4.3 Field Overlap Integrals

Nonlinear phenomena in waveguides are mediated by coupling of the respective field with the nonlinear polarization. Here, the original work by Stolen and Bjorkholm [94] is followed who introduced the following overlap integrals

$$J_{ijkl} = \iint \psi_i \psi_j \psi_k \psi_l \, dxdy, \tag{27}$$

where transverse fields ψ_i are normalised such that $\iint |\psi_i|^2 \, dxdy = 1$ and the indices may represent different fibre modes involved in the mixing process. As is customary in SIF, transverse fields can be chosen purely real valued [64] obviating a notation with complex fields. The physical dimension of J_{ijkl} is m^{-2} and associated with an effective area. For this thesis only the cases of self-phase modulation, i.e. $J_{iiii} \Rightarrow J_{\text{SPM}}$, cross-phase modulation, i.e. $J_{iijj} \Rightarrow J_{\text{XPM}}$, and third harmonic generation, i.e. $J_{ijjj} \Rightarrow J_{\text{THG}}$, are relevant. The coupling coefficients using the respective fields of pump and harmonic read:

$$J_{\text{SPM}} = \iint |\psi_{P,H}|^4 \, dxdy,$$

$$J_{\text{XPM}} = \iint |\psi_P|^2 |\psi_H|^2 \, dxdy, \qquad (28)$$

$$J_{\text{THG}} = \iint \psi_H \psi_P^3 \, dxdy.$$

Note that inverse THG is characterised by the same J_{THG} due to real valued fields.

In order to achieve modal coupling in a cylindrical SIF, the symmetry of pump and TH fields must match [95]. Assuming a pump in a HE_{11}, only hybrid modes of type HE_{1n}, EH_{1n}, HE_{3n}, and EH_{3n} yield non-vanishing overlaps in cylindrical SIF [96]. HE-modes are preferred due to their modal shape over EH modes forming ring-shaped profiles with a central node and more complex field distribution (see Fig. 1 (b)).

2.4.4 Coupled Evolution Equations for Harmonic Generation

Modelling the propagation dynamics in THG can be performed analogously to a single propagating mode using a set of coupled GNLSEs introduced to analyse XPM [97] extended by a term for THG [98,99]. It is to note that the former work discarded both dispersion and inertial effects, such as *Raman* scattering. Despite the simplifications made, the analysis in [13] is instructive. Here, however, the full dispersion, retarded nonlinear response and THG terms are retained and given in Eqs. (29) & (30) for each of the normalised modal amplitudes $U_\sim = A_\sim / \sqrt{P_P}$.

$$\partial_\xi U_P = \mathcal{D}_P U_P + \mathcal{N}_P U_P + i\jmath_H N^2 U_H U_P^{*2} \exp\{i\pi L_c^{-1} L_D \xi\} \qquad (29)$$

$$\partial_\xi U_H + L_D/L_w \partial_\tau U_H = \mathcal{D}_H U_H + \mathcal{N}_H U_H + i\jmath_H N^2 U_P^3 \exp\{-i\pi L_c^{-1} L_D \xi\} \qquad (30)$$

Normalised units are introduced as for Eq. (16): $\xi = z/L_D$, $\tau = (t - \beta_1 z)/T_0$ using the pump pulse duration T_0, dispersive length $L_D = T_0^2/\beta_2^P$, and pump soliton number $N^2 = L_D \omega_P n_{2,el} c_0^{-1} J_{\text{SPM}} P_P$. Due to this definition, prefactors of 3 and 6 arise in $\mathcal{N}_H$ for SPM and XPM compared to $\mathcal{N}_P$, moreover the prefactor for the THG term is 1/3 of the factor for SPM and inverse THG, due to the lesser number of possible field permutations[3]. The dispersive operators $\mathcal{D}_\sim$ are defined in Eq. (31), nonlinear operators are defined in Eq. (32) and (33) for pump and harmonic, respectively. The retarded

---

[3] A simpler argument: $\cos(\omega t)^3 = 3/4 \cos(\omega t) + 1/4 \cos(3\omega t)$

response is given in Eq. (34). Further, the walk-off length $L_w = T_0/GVM$ between pump and harmonic was introduced using the GVM as in Eq. (24). Note $L_w < 0$ if $GVM < 0$, i.e. the harmonic propagates faster than the pump, hence L_w may be interpreted as distance required for the pump to precede its harmonic. Similarly, the coherence length is introduced such that $L_c \Delta\beta_0 = \pi$, i.e. the distance after which pump and harmonic are out of phase and energy transfer back towards the pump is expected.

In case 2nd order dispersion may be neglected, i.e. close to a zero dispersion wavelength (ZDW, λ_{ZD}) and hence $L_D \Rightarrow \infty$, a suitable length scale may be defined either via the next non-vanishing dispersion coefficient $L'_D = T_0^n/\beta_n$ or a scale chosen according to the nonlinear process.

$$\mathcal{D}_{P,H} = i \sum_{n \geq 2} i^n \delta_n \partial_\tau^n \quad \text{with} \quad \delta_n^{(P,H)} = \frac{\beta_n^{(P,H)}}{n! \, T_0^{n-2} |\beta_2^P|} \tag{31}$$

$$\mathcal{N}_P = iN^2 (1 + is\partial_\tau)\big(\mathcal{H} * (|U_P|^2 + 2\jmath_X |U_H|^2)\big) \tag{32}$$

$$\mathcal{N}_H = iN^2 (1 + is\partial_\tau)\big(\mathcal{H} * (3\jmath_S |U_H|^2 + 6\jmath_X |U_P|^2)\big) \tag{33}$$

$$\mathcal{H}(\tau) = \delta(\tau) + n_{2,el}^{-1} \sum n_{2,k} r_k(\tau) \tag{34}$$

Each $\jmath_\sim$ represents an overlap normalised to J_{SPM} at ω_P, i.e. a_{eff}^{-2}, with subscript S for SPM, X for XPM, and H for THG, respectively.

Inspection of Eqs. (29) & (30) reveals the retarded response is accounted for in phase modulation terms only as it is included in the nonlinear operators $\mathcal{N}_{P,H}$. The source for THG, however, is a nonlinear polarisation oscillating at $3\omega_P$. Since an optical cycle is much shorter than typical rise and decay times of molecular responses, only the electronic nonlinearity contributes to THG. Therefore, THG in bulk liquids allows determining solely the electronic nonlinearity of molecular liquids [100–102]. Rau *et al.* [103] compared nonlinear susceptibilities, i.e. a nonlinear parameter proportional to the nonlinear IOR, derived from self-focussing and THG experiments. Their ratios are in good agreement with the ratio of the total nonlinearity and the purely electronic effects.

3 Simulations of Nonlinear Evolution in Retarded Media

Propagation dynamics are discussed in this chapter based on the GNLSE. After a brief introduction of linear propagation, nonlinear effects are considered. Subsection 3.2 presents spectral transformations due to phase modulation to determine effects of instantaneous and retarded nonlinearity that occur for both pump and harmonic wave. In 3.3 coupled wave dynamics are in focus to aid waveguide design for THG.

3.1 Propagation in Linear Medium with Dispersion

For the case of low powers ($N \ll 1$) a pulse will experience dispersion in a medium or waveguide during propagation whereas the spectral power distribution remains unaltered. As introduced in Eq. (11) higher orders of dispersion lead to phase accumulation depending on the frequency. Two examples are shown in Fig. 3 in the temporal (a) and spectral domain (b). The initial pulse (dashed, black) is assumed transform limited, i.e. exhibits no higher order spectral phase, and is propagated by L_D experiencing 2nd order (solid, red) or 3rd order spectral phase (solid, blue), respectively. A reduction of peak power and temporal reshaping is evident. The spectrum for all cases is shown as dashed line (left axis, in (b)) and coloured lines represent the group delay (right axis), i.e. the relative arrival times of the respective frequency and is calculated as $\tau_g = \partial_\omega \Phi(\Delta\omega)$, where Φ represents the spectral phase. The positive slope of the red curve in (b) signals a linear increase in instantaneous frequency (up-chirp) due to positive 2nd order phase ($GVD > 0$). The quadratic delay (blue) leads to simultaneous occurrence of frequency detuned waves which cause a beat signal in time domain as shown by the blue curve in (a).
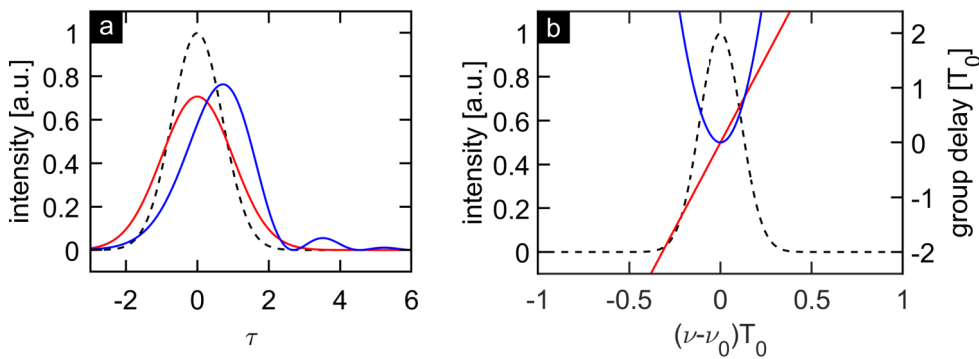
Fig. 3: (a) Temporal intensity without dispersion (dashed), 2nd order dispersion (red), and 3rd order dispersion (blue, $\delta_3 = 0.4$) after propagating L_D. (b) Spectral intensity (dashed, left axis) and group delay (colour, right axis) for pulses shown in (a).

3.2 Propagation in Nonlinear Medium without Dispersion

In this section the distinct effects of nonlinearity are investigated neglecting dispersion which in practice can be justified for intense pulses, i.e. $N^2 \gg 1$, and appropriately designed waveguides such that $L_D \gg L$, where L represents sample length. However, at first a discrepancy in terminology across research communities engaged in the field of retarded media is briefly discussed.

What determines a highly non-instantaneous configuration?

Whereas the answer to this question in the analogue spatial domain is well accepted, i.e. a highly nonlocal medium exhibits a response much wider than the excitation beam and vice versa, a local medium exhibits a response much narrower than the excitation beam [104–106], this is not the case in the temporal domain where opinions among researchers seemingly diverge. Research motivated by theory usually applies the above terminology [48,107]. In contrast, in experimental work high retardation is associated with large molecular fractions arising from longer pulses [38,39,41,108]. Fig. 4 illustrates this issue for a series of different pulse durations and a response of the form $r \propto t \cdot \exp\left(-t/\tau_f\right)$ with a ratio of nonlinearities: $n_{2,R}/n_{2,el} = 9$. Hence the maximum f_R amounts to 0.9 for the continuous wave case and is similar to molecular liquids.

Pulse durations T_0 are scanned and given in ratios of the fall time τ_f as stated in panels (a) and (b). Curves in (a) are normalised to emphasise the greater overlap of longer pulses (coloured) with the response (black, dashed) naturally leading to a larger relative contribution which is reflected in f_R in (c) as defined in Eq. (22). Importantly, f_R does not depend on the choice of scale as it relates the intensity weighted nonlinear average indices. For calculations of the NLP (b) the following definition is used in accordance with Eqs. (18) and (19): $\Phi_{\mathrm{NL}} = \Phi_0\big(|U|^2 + n_{2,R}/n_{2,el} \cdot r * |U|^2\big)$. A reduction in peak power due to stretching the pulses is accounted for in U, i.e. all pulses exhibit a constant energy which is of greater practical relevance since pulses may be stretched in time maintaining their energy via, e.g. dispersive propagation. Constant factors such as sample length, pulse energy, and nonlinear parameter are absorbed in Φ_0.

From the experimental perspective, longer pulses leading to larger f_R harness a greater part of the retarded response, i.e. provide higher sample nonlinearity, which hence may be considered a highly non-instantaneous configuration. However, the NLP presented for different pulse durations in (b) suggests the contrary. Shorter pulses

resolve the different mechanisms contributing the NLP, i.e. the NLP is altered significantly in comparison to longer pulses. The NLP resembles the case of instantaneous media for width ratios around 1 despite the delay due to the asymmetry of the response. Here, NLP for pulses of width 0.1 are noticeably altered suggesting large impact from retardation, whereas the respective molecular fraction is less than 10 % indicating the effective nonlinearity is mainly of electronic nature. Yet, the peak of NLP due to retardation is already 50 % of the global peak of the total NLP (see (b), teal curve). The peak NLP for different pulse durations is extracted from the NLP curves and is shown in (c). The coloured lines show the pure retarded (blue, dashed) and total (red, solid) NLP normalised by the overall highest NLP among the parameter range, i.e. the electronic contribution for the shortest pulse. The kink at ≈ 0.22 occurs when the two peaks from instantaneous and retarded phases are equal at $f_R \approx 0.2$. This case is close to silica fibres which are commonly considered quasi-instantaneous.
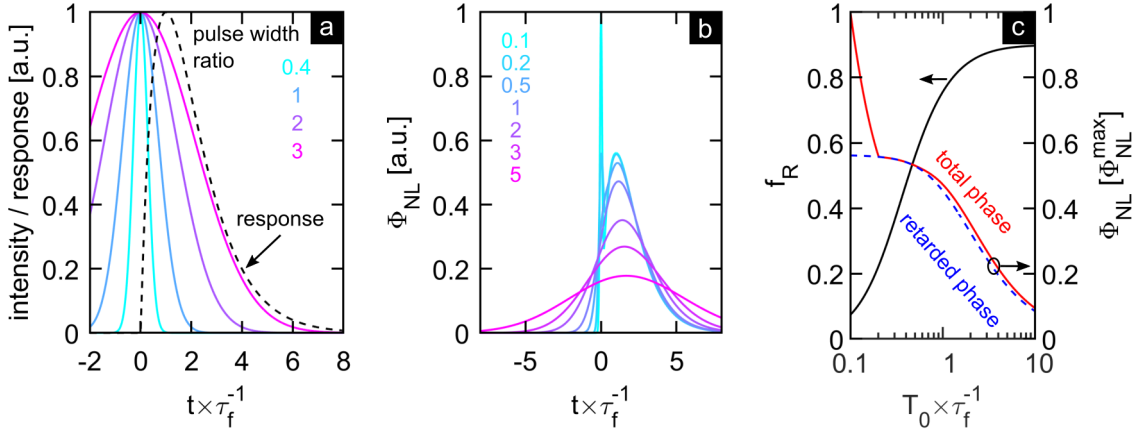
Fig. 4: (a) Response $r \propto t \cdot \exp\left(-t/\tau_f\right)$ (dashed, black) and pulses (coloured) with durations T_0/τ_f as stated versus normalised time. Curves are normalised to power. (b) NLP for pulses of equal energy and of width ratio as stated versus normalised time. Ratio of nonlinearities is $n_{2,R}/n_{2,el} = 9$ and NLP is normalised to the global peak phase. (c) Molecular fraction (black, left axis) and local peak NLP for total and retarded NLP normalised by global total peak NLP (colour, right axis). The kink for total phase (red) occurs at $T_0/\tau_f \approx 0.22$ when retarded and electronic NLP are level at $f_R \approx 0.2$.

Proposing a new standard for definitions is not the intent of this thesis, however the demand for a unified terminology across the research community in this field is emphasised. For the following analysis in this chapter relevant scales and ratios are used to characterise propagation dynamics providing insights to individual nonlinear effects.

3.2.1 Self-Phase Modulation – Impact of Electronic and Retarded Response

At first, spectral changes due to SPM are investigated for instantaneous and non-instantaneous media based on the evolution equation $\partial_\xi U = i\Phi_0 \cdot h * |U|^2 \cdot U$. Using a solution of the form $U(\tau, \xi) = U(\tau, 0) \cdot \exp(i\Phi_{NL})$ where $\Phi_{NL} = \Phi_0 \cdot h * |U|^2 \xi$ is the NLP and h is the material response scaled such that Φ_0 represents the maximum phase shift after a propagation distance $\xi = 1$. Assuming Gaussian pulses the resulting spectra and group delays for increasing NLP are presented in Fig. 5. The top row illustrates the electronic Kerr effect ($h(\tau) \propto \delta(\tau)$) exhibiting symmetrical spectral broadening (a) and an overall up-chirp across the pulse (b).
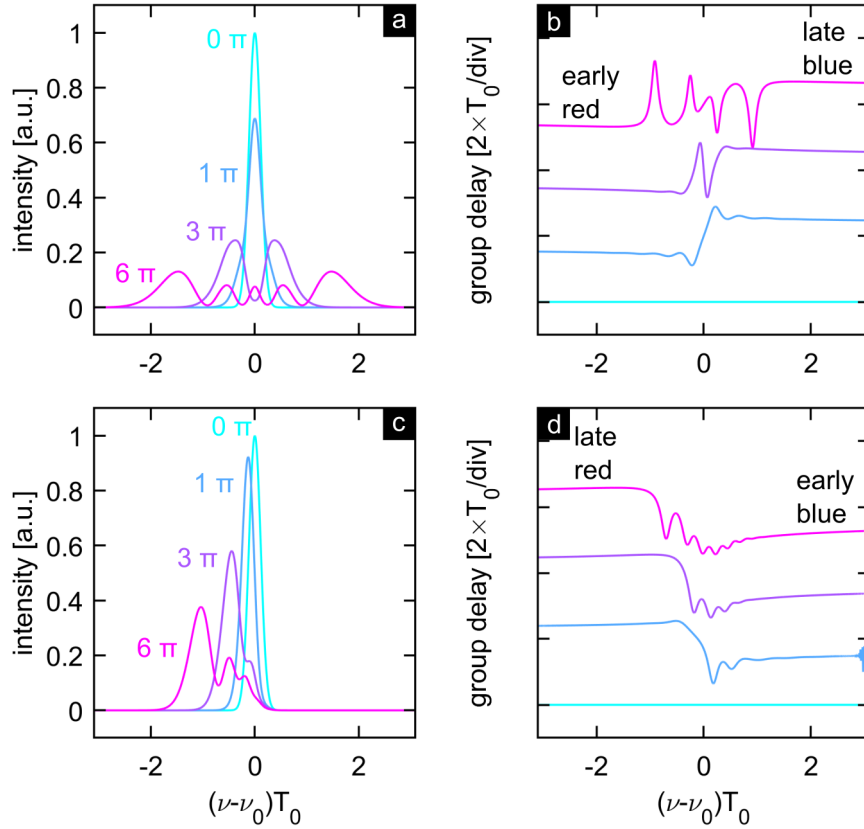
Fig. 5: Spectral broadening and group delay for instantaneous (a, b) and non-instantaneous (c, d) response $h \propto \tau \cdot \exp(-\tau/3)$ for peak nonlinear phases Φ_0 as stated in (a, c). Group delays are separated by 2T₀ for clarity.

In the bottom row spectra resulting from a non-instantaneous medium with a response $h(\tau) \propto \tau \cdot \exp(-\tau/3)$ are shown. It is to emphasize the NLPs stated in panels (a) and (c) correspond to the peak NLPs for each case, however to achieve such a peak NLP for the retarded response a $\approx$15.4-fold greater intensity, or a ratio of $n_{2,R}/n_{2,el} = 15.4$ is required. Hence the contribution to broadening is comparably small unless $n_{2,R}$ exceeds $n_{2,el}$ noticeably. Asymmetric broadening towards smaller frequency resulting in

an overall red-shift is apparent. Still in this case the frequency is down-chirped (albeit being lower overall) across the pulse contrasting the previous case of an instantaneous response.

3.2.2 Impact of the Response Functional Form

The objective of this subsection is to identify parameters the frequency down-shift is most pronounced and likely to be observed experimentally. The particular impact of the response function form is hence investigated using the over-damped oscillator response

$$r(t > 0) = \frac{\tau_r + \tau_f}{\tau_f^2} \left(1 - \exp\left(-\frac{t}{\tau_r}\right) \right) \exp\left(-\frac{t}{\tau_f}\right), \tag{35}$$

which is commonly used to model dipolar, diffusion, and collisional responses providing two parameters namely the rise and fall times τ_r and τ_f, respectively. $r(t)$ is shown in Fig. 6 (a) for a variety of rise times along with its asymptotic responses (dashed: $\tau_r \ll \tau_f$ and dot-dashed: $\tau_r \gg \tau_f$). Note time is scaled in τ_f and despite the large values of τ_r the response peaks within τ_f, i.e. its delay is still finite.

Fig. 6 (b) presents the gain associated with the response for negative frequency shifts similar to the common Raman gain in silica. The Raman gain in silica however originates from photon-phonon interaction rather than induced motion. Colours in (b) correspond to those from (a) for various τ_r.
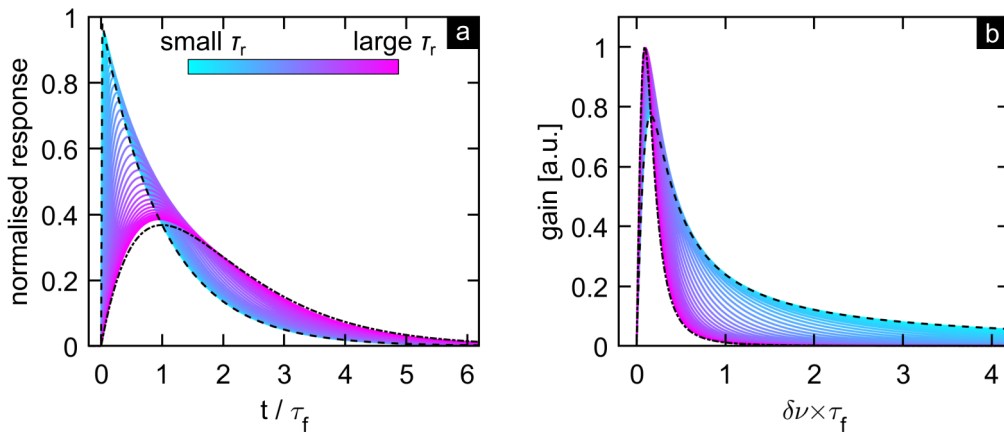
Fig. 6: (a) Shape of damped oscillator response for various rise times versus normalised time. (teal: $\tau_r \ll \tau_f$; magenta: $\tau_r \gg \tau_f$). Asymptotic responses are shown in black (dashed: $r \propto \exp(-\tau)$ and dot-dashed: $r \propto \tau \cdot \exp(\tau)$, respectively. (b) Gain for normalised red-shift from the excitation central frequency as commonly used for Raman spectra. Colours correspond to those from (a).

In the following the response parameters are scanned in units of the pulse duration and spectra due to SPM for increasing NLP are evaluated. To condense data and extract information, all spectra are analysed in terms of moments defined as:

$$\langle x^M \rangle = \frac{\int x^M |U(x)|^2 dx}{\int |U(x)|^2 dx} \tag{36}$$

Here, x represents frequency but in general may represent any physical coordinate. As it is common, moments for $M > 1$ are centred by the 1st moment which is assumed implicit in Eq. (36). In the context of normalised units, $\langle x^1 \rangle$ is associated with the shift of the central frequency $\delta\nu_{COM} \times T_0$, i.e. the spectral centre of mass (COM), and $\sqrt{\langle x^2 \rangle}$ represents the *root-mean-squared* bandwidth denoted as $\sigma = T_0 \times \langle (\nu - \nu_0 - \delta\nu)^2 \rangle^{1/2}$. The first two moments are illustrated in Fig. 7 (a) for a SPM broadened spectrum with parameters as stated in the caption.
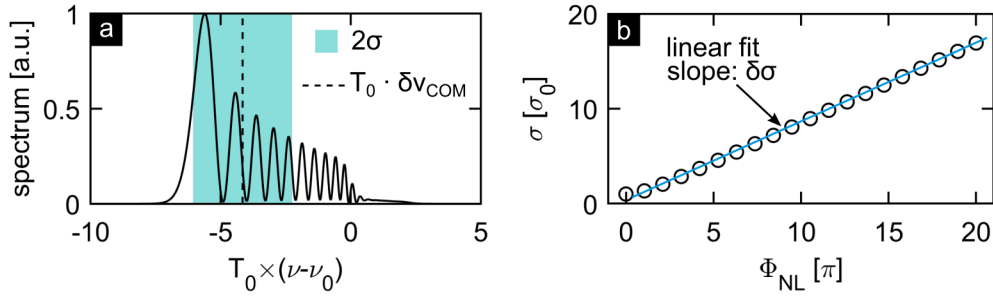
Fig. 7: (a) Illustration of spectral moments. The spectrum (solid, black) is obtained from a Gaussian pulse modified by SPM of the over-damped oscillator (Eq. (35), $\tau_r = 0.5$, $\tau_f = 3$, $\Phi_{NL} = 20\pi$). Dashes represent spectral COM and bandwidth is highlighted by the shaded area. (b) Representative example of bandwidth evolution for increasing nonlinear phase.

Both $\delta\nu$ and σ evolve with increasing NLP, yet their dynamics are well captured by a linear fit of the resulting moments versus NLP as is shown for the bandwidth exemplarily in Fig. 7 (b). The fitted parameters, i.e. the rates at which the central frequency and bandwidth change, are then scaled by the initial bandwidth and are shown in Fig. 8 (a) and (b), respectively.

It is to emphasise that the rates compensate the neglect of dispersion as those measure changes per acquired NLP rather than absolute moments whose dynamics may decline with reduced acquisition of NLP due to e.g. dispersive broadening.
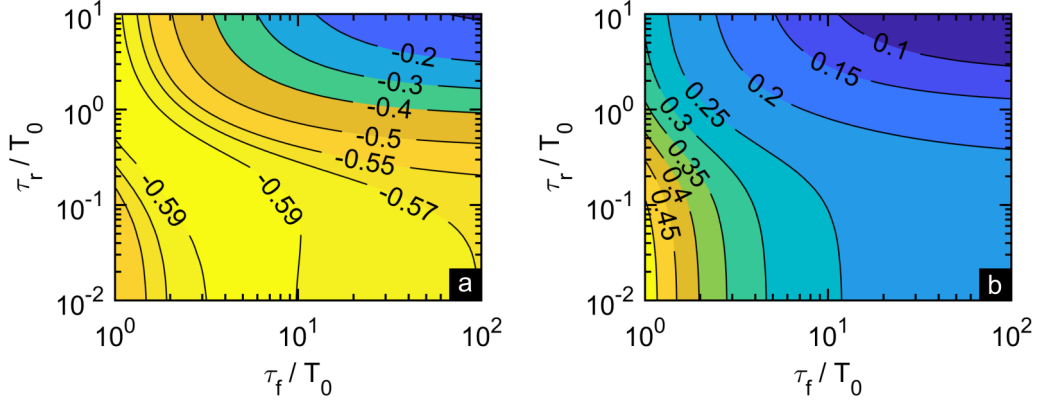
Fig. 8: Contours of evolution for 1st and 2nd spectral moment for a range of rise and fall times normalised by pulse duration. Bright yellow represents largest absolute rates. (a) Shift of central frequency and (b) increase of bandwidth each in units of σ_0/rad.

The largest absolute shift rates $\delta\nu_{\mathrm{COM}}$ from (a) are observed in a relatively wide range of parameters, whereas broadening rates $\delta\sigma$ from (b) increase for faster responses, i.e. a response more similar to an instantaneous nonlinearity, as broadening originates from the steepness of the NLP. Further, spectra exhibit an overall greater down-shift rate in frequency than broadening rate, which can lead to depletion at the initial central frequency. Although similar to soliton self-frequency shift known from anomalous dispersive silica fibres [109,110], here spectra exhibit pronounced asymmetry, i.e. spectral amplitudes of frequencies smaller than the central frequency are greater than amplitudes of larger frequencies as in Fig. 5 (c).

To better visualise the dependence throughout the large range of responses the data from Fig. 8 is shown as scatter plot in Fig. 9 for all ratios of τ_r and τ_f. Note colours are the same as above representing the vertical axis value.
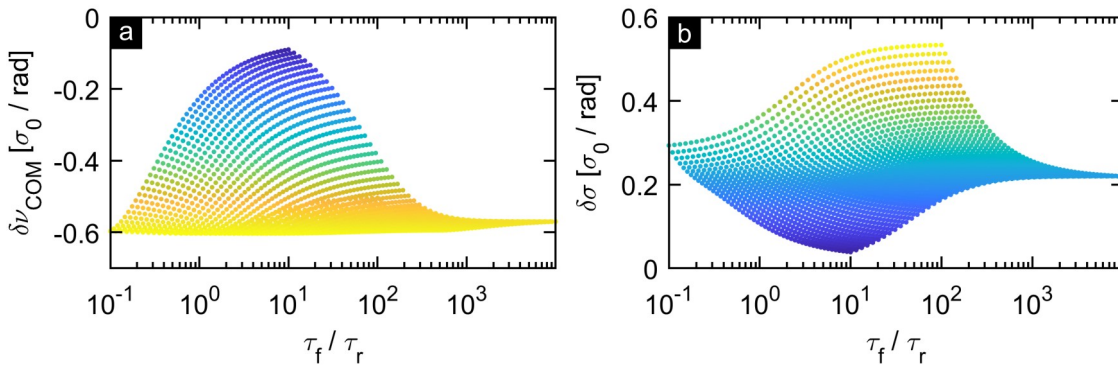
Fig. 9: Scattered representation of data from Fig. 8 versus the ratio of fall and rise time. (a) Shift rate of central frequency and (b) bandwidth enhancement rate. Vertically extended clusters denote larger susceptibility to pulse duration.

The extent of the scatter plot reveals the impact of pulse duration which is most prominent for ratios $\tau_f/\tau_r \approx 10$ but the sensitivity to pulse duration is overall larger in the range 1-10. This range is rather common in case of molecular liquids whose response consists of multiple components [35] highlighting their relevance for experimental studies. Although limited to $-0.6\,\sigma_0/\text{rad}$ for each ratio of rise and fall times there is an optimal pulse duration to achieve the largest possible red-shift as suggested by the local maximum of the shift-rate in Fig. 8 (a).

Although any response obeying causality and the implications invoked by Kramers Kronig relations [111] leads to the same qualitative behaviour, i.e. frequency down shift while broadening, the numerical study reveals quantitative impact of the functional form. To this end, inertial responses from molecular liquids are found very suitable due to their beneficial ratios of rise and fall times in general which may be probed under favourable conditions that exhibit maximal sensitivity to pulse duration.

3.2.3 Self-Phase Modulation – Effects of a Combined Response

In this section the interplay of electronic and retarded nonlinearity is studied. While the former is inevitable in any kind of medium, the contribution of the latter is a specific material property and hence may vary. To this end the spectral evolution for a response of the form $\mathcal{H}(\tau) = \delta(\tau) + \frac{n_{2,R}}{n_{2,el}} r(\tau)$ is studied for a range of ratios of the nonlinearities and pulse durations. The response functional form of CS_2 is chosen for $r(\tau)$ [87] as it is well characterised due to the relevance of CS_2 in previous work in the field of liquid photonics. Further, CS_2 exhibits the largest nonlinearity among the liquids that may be considered suitable for experiments [35] and at the same time features the largest possible ratio of inertial and electronic effects. Further considerations of the selection process of suitable core media are presented in section 4.1.

Resulting SPM spectra mediated by the response $\mathcal{H}$ are shown in Fig. 10 (b-d) for different pulse durations as illustrated in (a). The pulse durations T_0 are 0.3 (b), 1 (b) and 5 (d) in units of the rise time τ_r which for CS_2 amounts to 150 fs and is a generally accepted value for reorientational effects and hence chosen to normalise time and frequency. The prominent decay of the diffusive contribution is 1.6 ps and hence $\tau_f / \tau_r \approx 10$. The ratio of nonlinearities amounts to 17.5 for the physical response.
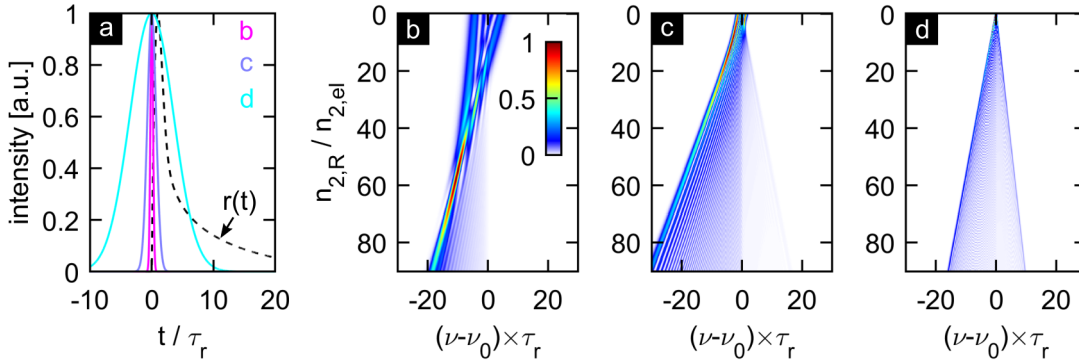
Fig. 10: Spectral broadening in the presence of the electronic effect. (a) Physical response shape of CS_2 (dashed, black) and pulses of width 0.3 (b), 1 (c), and 5 (d) in units of τ_r. Spectra are shown for the respective pulse duration in (b-d) for a nonlinear electronic phase shift of 4π accompanied by the phase shift due to retardation for increasing ratios of nonlinearities.

While scanning $n_{2,R} / n_{2,el}$ the peak power of these pulses was maintained such that the purely electronic contribution amounts to a peak phase shift of 4π i.e. the inertial effects are added to the phase, rather than competing with the electronic effect. Despite the additional phase, the bandwidth for the shortest pulse (b) is not significantly enhanced as opposed to the cases of longer pulses. In fact, a broadening reduction

occurs for pulses short enough to resolve the distinct phase contributions from electronic and inertial effect (also see Fig. 4 (b) p. 20) which eventually lead to smoother phase, that is a smaller gradient, and therefore lesser broadening.

However, regardless of the ratio of nonlinearities spectra generally broaden for larger accumulated nonlinear phases either due to higher power or further propagation.

Analogous to the previous chapter the rates of frequency shift and frequency broadening are presented in Fig. 11 (a) and (b), respectively. Throughout all cases a linear trend was observed and subsequently the rates are derived from a linear fit. The numbers in colour represent the nonlinearity ratio employed for the simulation while pulse duration was varied. The case of a purely instantaneous response is included in (b) for the broadening rate (dashed) which is independent of pulse duration and amounts to 0.86 as was found numerically and is derived in [85]. There is no centre frequency shift in case of the purely electronic nonlinearity.
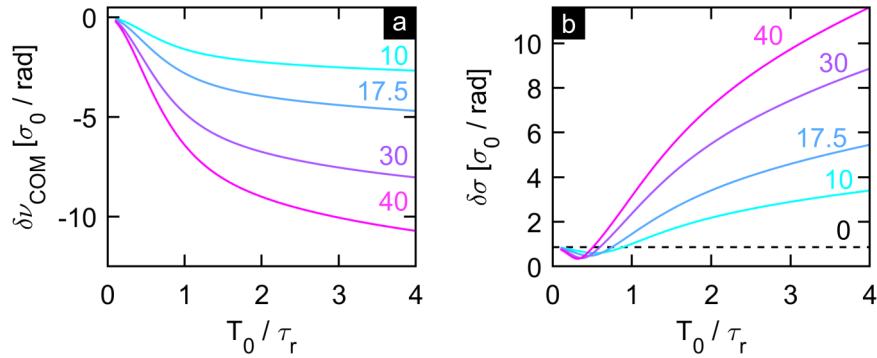
Fig. 11: Rates of central frequency shift (a) and bandwidth increase (b) versus pulse duration. Coloured numbers represent the ratio $n_{2,R}/n_{2,el}$ and 17.5 represents the case of CS_2. The dashed black line in (b) corresponds to the broadening rate of 0.86 for a purely instantaneous medium.

It is observed that both shift and broadening rates increase in absolute value for both larger retarded contribution and pulse duration overall. Since either parameter is scaled to σ_0 this is only a measure of efficiency and must not be mistaken for largest overall bandwidth which may be achieved. For a particular range of pulse durations approximately at $0.4\,\tau_r$ the broadening rate is reduced compared to the sole electronic effect despite the higher total nonlinearity – pulses partially resolve the rise time of the response leading to flatter phase.

This range of T_0, where SPM based broadening is reduced, may prove beneficial for frequency conversion processes with limited phase matching bandwidth.

3.2.4 Cross-Phase Modulation and Retardation

In this subsection the interplay of co-propagating waves is studied to provide insight to the dynamics induced by XPM for pulses with varying relative delay, or similarly, GVM leading to accumulated delays during propagation. These results are of interest in view of THG to assess the dynamics after the initial generation when pump and harmonic propagate the remaining sample length in presence of a retarded nonlinearity.

The results below deploy the solution presented by Agrawal *et al.* [112] and are obtained by evaluating spectra for waves of the form $U(\tau, \xi) = U(\tau, 0) \cdot \exp(i\Phi_{\text{XPM}})$, where $\Phi_{\text{XPM}} = \Phi_0 \int_0^\xi h * |A(\tau - \tau_d + z \cdot GVM/T_0,)|^2 dz$ represents the accumulated NLP due to the pump wave A. In the following examples T_0 of pump and probe wave are identical throughout and Φ_0 was chosen such that the electronic NLP amounts to 20π when $\xi = 1$ representing the end of the sample. The value of 20π for NLP is chosen for displaying purposes. Dispersive effects are neglected and at first $GVM = 0$, i.e. pump and probe co-propagate for various initialised delays τ_d of the pump with respect to the probe pulse centre. For $\tau_d > 0$ the NLP due to the pump wave trails behind the probe wave and vice versa for Fig. 12. All spectra are normalised to unity individually for clarity. Panel (a) shows the purely electronic effect: a delayed pump induces a positive NLP gradient, i.e. frequency down shift, whereas an advanced pump causes a negative NLP gradient leading to frequency up shift. The effect exhibits odd symmetry and the spectral modulation is mirrored. Note that due to scaled units the spectra are identical for any pulse duration.

For the remaining panels (b-h) the physical response of CS$_2$ is added and both pulse durations are varied in units of τ_r of the response as stated in each panel. It is observed that a trailing phase enhanced by the response leads to extended broadening but the temporal extend of this effect is limited similarly to the electronic effect in (a). By contrast, for an advanced pump the longer temporal interaction is evident by greater extension of spectral modulation for $\tau_r < 0$, i.e. the odd symmetry is broken. Generally the extent of up shift is reduced due to the smoother decay of NLP in all cases compared to trailing phase.

If phase is advanced by the physical time of approximately τ_r (note the range of normalised delays in (b-h) varies due to different T_0/τ_r), spectra exhibit relatively large susceptibility to pulse duration. Spectra at these delays (≈ -3 in (b-c)) are

predominantly modulated with decreasing structure towards longer pulses, i.e. (d, e). Cases (f, g) yield wider and smoother spectra than any of the other configurations shown for a delay of ≈ -1. Such spectra seem well suited for XPM induced pulse compression similar to a scheme using cross polarised pulses in CS_2 [113] exploiting a nonlinearly induced negative change of IOR.
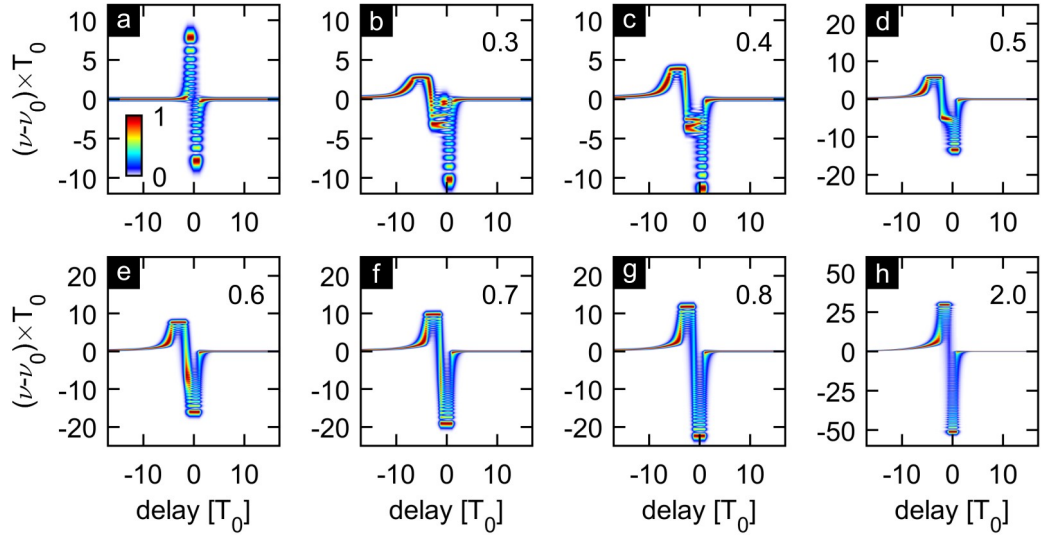
Fig. 12: Spectra of a weak probe pulse due to XPM induced phase changes for various delays of the pump pulse. Each spectrum in each panel is scaled to unity individually for clarity. For negative delays the pump is leading and for positive delays the pump trails behind the probe. The NLP due to the electronic effect is 20π in all cases. (a) is purely electronic, (b)-(h) include the retarded response of CS_2. Pulse durations in units of τ_r are given in each panel, note (a) is identical for all pulse durations due to normalised scales.

In view of experimental THG the case of non-vanishing GVM due to the difference in frequency of pump and harmonic wave is of importance. Since THG is expected to be most efficient at the pulse centre, i.e. for highest intensities, an initial delay of zero is assumed henceforth. Otherwise conditions are maintained to the above cases and at first the evolution in an instantaneous medium is illustrated in Fig. 13 for $GVM > 0$ (a) and $GVM < 0$ (b), respectively. Distance is scaled in walk off length and for the electronic nonlinearity mirror symmetric spectral modulation is observed which saturates after two walk off lengths, i.e. a temporal separation of pulses by 2 T_0. In case of an advanced pump the probe spectrum experiences frequency up shift and vice versa, both potentially able to counter, or balance, opposing shifts resulting from power dependent changes of the PM wavelength as introduced in section 2.4.1, Eq. (25) and below.
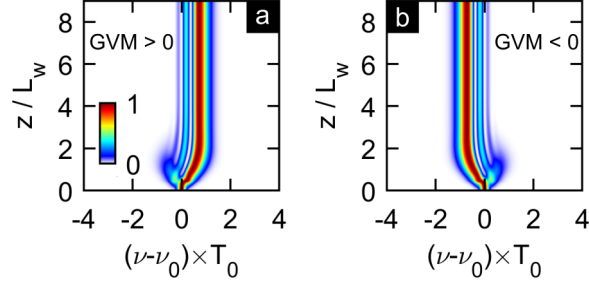
Fig. 13: Spectral evolution of a weak pulse that undergoes XPM by a strong pump in an instantaneous medium for positive GVM (a) and negative GVM (b). NLP is set to 20π and both pulse durations are identical. Distance is scaled by $L_w = T_0/|GVM|$. Each spectrum is scaled to unity individually for clarity. Spectral modification saturates at $2L_w$, i.e. a distance after which pulses are split by $2T_0$.

Including the retarded response as in Fig. 14 the modulation depends on pulse duration (numbers in panels represent T_0/τ_r) particularly in case of $GVM > 0$ (a-d), whereas a common saturation distance as in the electronic case of $\approx 2L_w$ can be observed for $GVM < 0$ (e-h). For advanced pumps, a decelerating spectral transformation is present due to the long range response, yet spectral extension stagnates. For pulse durations equal or longer than τ_r initial broadening is evident particularly for case (c) up to $2L_w$ after which the decaying NLP initiates an up shift.
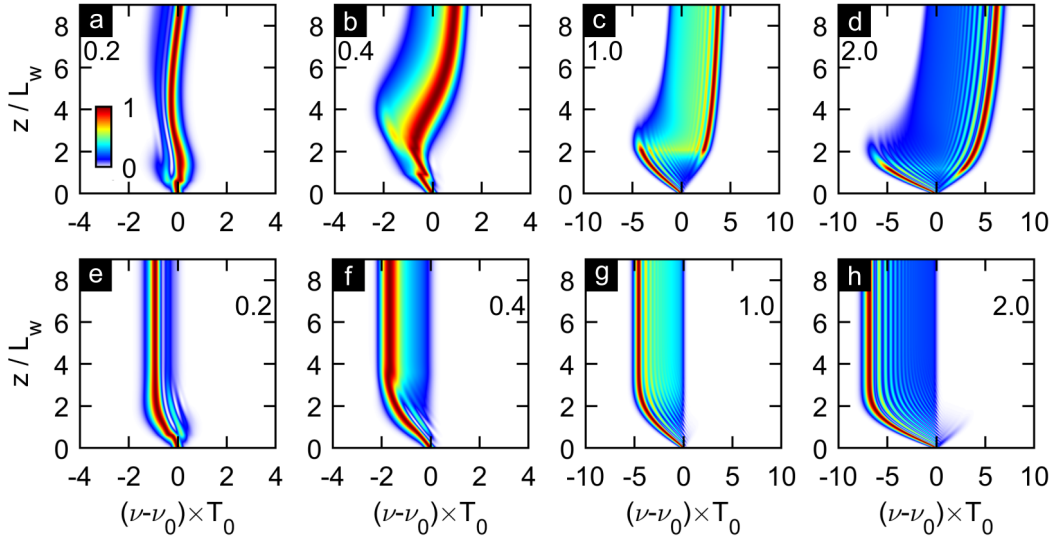
Fig. 14: Specral evolution of weak pulses due to XPM of a strong pump in a medium with retarded response as in CS$_2$. The NLP due to the electronic effect is 20π (a-d) $GVM > 0$, i.e. faster pump, and (e-h) $GVM < 0$, i.e. slower pump pulse. Pump pulse durations are stated in each panel in units of τ_r and are identical for the probe pulse. In (e-h) modification of spectra ceases after $2L_w$, whereas in (a-d) the spectral shift continues with deceleration.

3.3 Coupled Evolution Dynamics of Pump and Harmonic

Numerical solutions of coupled NLS equations are presented to gain insights into the complex THG process. Different dispersion regimes and types of nonlinearity are studied in subsection one. Part two aims at optimising the efficiency to aid experimental design consideration and subsection three presents an experimental configuration in detail.

3.3.1 Overview of Evolution Dynamics

Simulations in this section are based on Eqs. (37) and (38) which are obtained from the set introduced in chapter 2.4.4. As conversion efficiency is typically low in the cases considered, i.e. $|U_H|^2 \ll |U_P|^2$, only SPM and XPM terms due to the pump field are employed. Both THG and inverse THG terms are retained. GVD for the pump and GVM are considered whereas higher orders of dispersion are neglected.

$$\partial_\xi U_P + i\frac{\varkappa}{2}\partial_\tau^2 U_P = i(\mathcal{H} * |U_P|^2)U_P + i\jmath_H U_H U_P^{*2} \exp\{i\pi L_c^{-1}L_D\xi\} \qquad (37)$$

$$\partial_\xi U_H + L_D/L_w\partial_\tau U_H = 6i(\mathcal{H} * |U_P|^2)U_H + i\jmath_H U_P^3 \exp\{-i\pi L_c^{-1}L_D\xi\} \qquad (38)$$

Note the soliton number N is absorbed via $U_{P,H}(\tau,\xi) \to NU_{P,H}(\tau,\xi)$ and $\jmath_X \approx 1$, which is typical for experimental conditions. $\varkappa$ is either $+1$ in the ND or -1 in the AD regime.

3.3.1.1 Electronic Nonlinearity and Anomalous Dispersion

By intuition THG should be driven most efficiently with highest powers which suggests pulses unaltered by dispersion, so called solitons, ideally serve as pump. These entities are considered in the following by launching pulses of the form $U(\tau,0) = 2\,\mathrm{sech}(\tau)$, i.e. the form of a higher order soliton with $N = 2$ comparing different conditions of dispersion such as walk-off and phase mismatch (PM) represented as ratios $L_{DW} = L_D/L_w$ and $L_{DC} = L_D/L_c$, respectively. Fig. 15 shows results propagating the pulse in the AD domain without perturbations from higher orders of dispersion and retardation except for THG with coupling $\jmath_H = 0.01$. Intensity evolution in the temporal (spectral) domain is shown in the top (bottom) row in linear (logarithmic) normalised scale.

Fig. 15: Temporal (top row, linear scale, common colour bar) and spectral (bottom row, log scale, common colour bar) evolution of sech-pulse ($N = 2$, AD, $\jmath_H = 0.01$) (a, e) and the resulting TH for different PM conditions. (b, f) $L_D/L_w = 10, L_D/L_c = 0$; (c, g) $L_D/L_w = 10, L_D/L_c = 50$; (d, h) $L_D/L_w = 0, L_D/L_c = 50$.

The pump (a, e) exhibits periodic evolution with period $\pi/2$ [114,115] and the remaining panels show the harmonic. GVM causes the delay observed in (b, c). (b-d) illustrate how THG and temporal compression of the pump coincide confirming the above intuition. Note, relative extent must not be mistaken for greater efficiency as each panel is normalised. However, the spectral extent observed in (h) results from on-going XPM of co-propagating waves and modulations along z are due to mismatched phases, as is also observed in the spectrum (g). Further, in case (c, g) clear detuning is seen (down-shift as both $\Delta\beta$, GVM > 0) and PM is indicated in panel (g) which occurs once seeded by spectral expansion (temporal compression) of the pump but subsequently splits off preventing dephasing. A second burst is generated at $z = 3\pi/4$, i.e. the instance of temporal compression. Note the resulting frequency modulation due to the double pulse is present shortly after $2.5\,L_D$ but hard to observe in log-scale. The frequency up-shift as discussed in previous sections is also present for cases with mismatched group velocities and is indicated in (f). Ultimately, spectral evolution is much affected by NLP as the periodic behaviour is seen to be transferred to the harmonic if phase mismatch is present. In those cases, however, the conversion efficiency is low.

3.3.1.2 Electronic Nonlinearity and Normal Dispersion

For comparison, the cases from above are illustrated in Fig. 16 for propagation in the ND domain. Note for the case (d, h) $L_D/L_c = 0$ was chosen unlike the case of $L_D/L_c = 50$ in Fig. 15 (d, h) for displaying purposes.
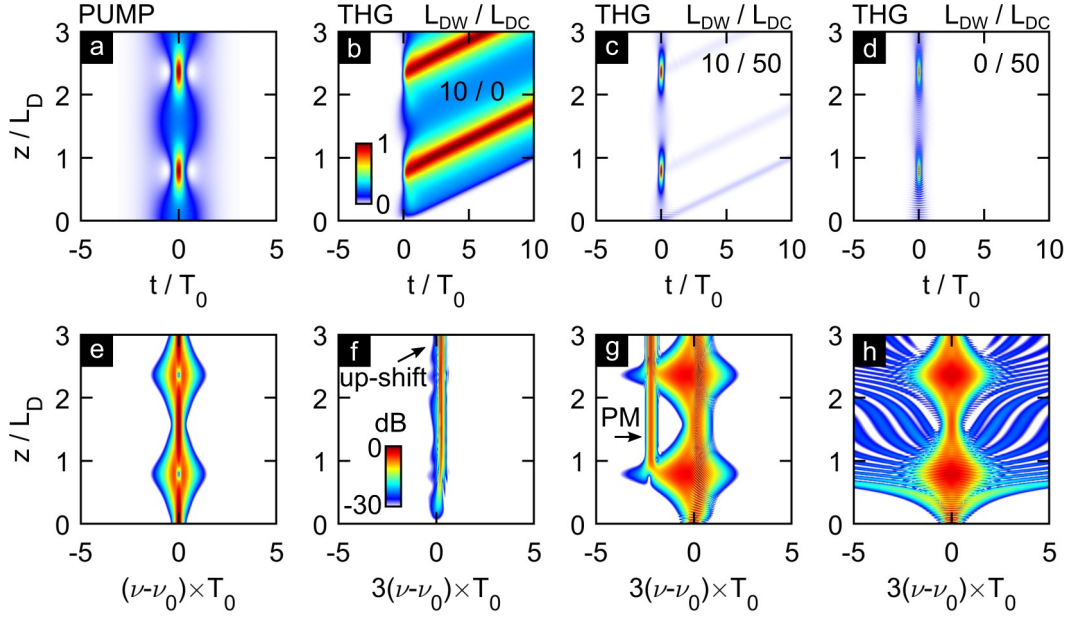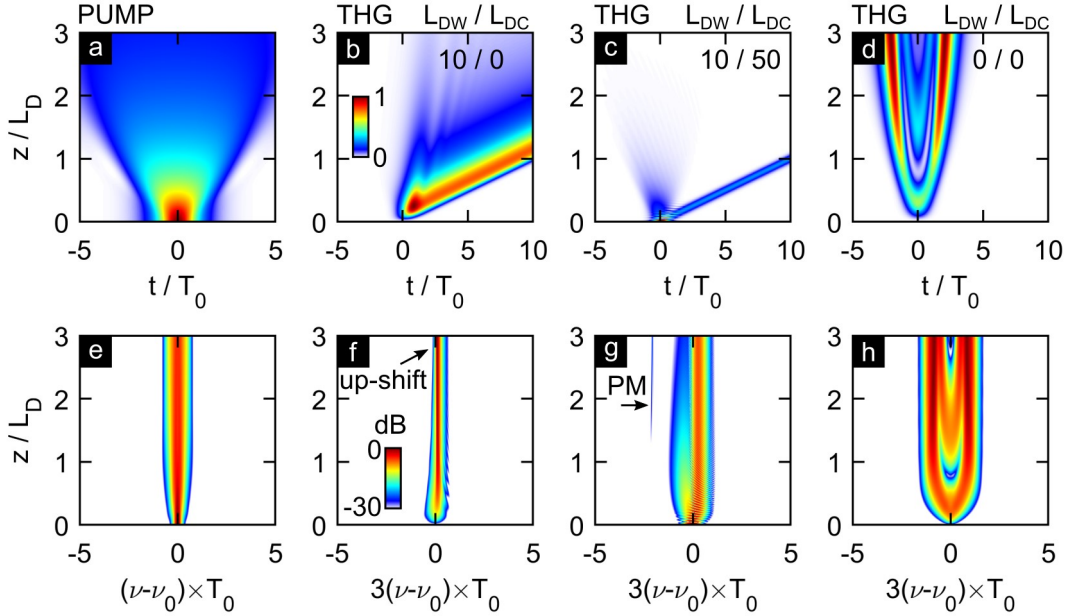

Fig. 16: Temporal (top row, linear scale, common colour bar) and spectral (bottom row, log scale, common colour bar) evolution of sech-pulse ($N = 2$, ND, $j_H = 0.01$) (a, e) and the resulting TH for different PM conditions. (b, f) $L_D/L_w = 10, L_D/L_c = 0$; (c, g) $L_D/L_w = 10, L_D/L_c = 50$; (d, h) $L_D/L_w = 0, L_D/L_c = 0$.

In contrast to the AD domain the pump pulse suffers from dispersion as seen in (a) and spectral broadening due to SPM ceases after one dispersive length due to reduction of intensity (e). Whereas frequency up-shift remains similar, no secondary THG burst is present as for the AD domain due to the lack of the pumps periodicity. The harmonic spectrum in (f) exhibits typical narrowing – the harmonic signal in temporal domain stretches which inevitably leads to bandwidth reduction, if not altered by NLP, as bandwidth is proportional to $(L \cdot GVM)^{-1}$. On the other hand, GVM may assist in preventing undesired phase shifts by temporally splitting pump from signal.

Panel (g) elucidates that signal generation at the PM wavelength occurs eventually, yet the significantly smaller seed (note the pump spectrum covers λ_{PM} in the numerical simulation due to the pulse form) leads to reduced generation, whereas phase mismatched TH rapidly splits off from the pump mitigating further back conversion.

The symmetrical shapes for (d, h) clearly indicate the dependence of phase matching on further effects, i.e. the pump GVD and SPM or XPM induced frequency shifts, yet such

dynamics can hardly be observed under experimental conditions as usually either phase or group velocities can be matched only.

3.3.1.3 Comparison of Conversion Efficiency

Typically nonlinear conversion processes are assessed in terms of their conversion efficiency defined here as the ratio of pump and harmonic pulse energy, i.e. $\eta = E_H/E_P$. The evolution of efficiency from examples above is presented in Fig. 17 for the AD (a) and ND (b) domain. Efficiencies are scaled by the largest observed efficiency which, interestingly, occurred for the case of perfect phase matching with $GVM > 0$ in the AD domain. By contrast, in the ND domain the case of matched phases and group velocities performed best, yet reached only 25% of the efficiency obtained in the AD due to dispersive pulse spreading in the range of shown examples.
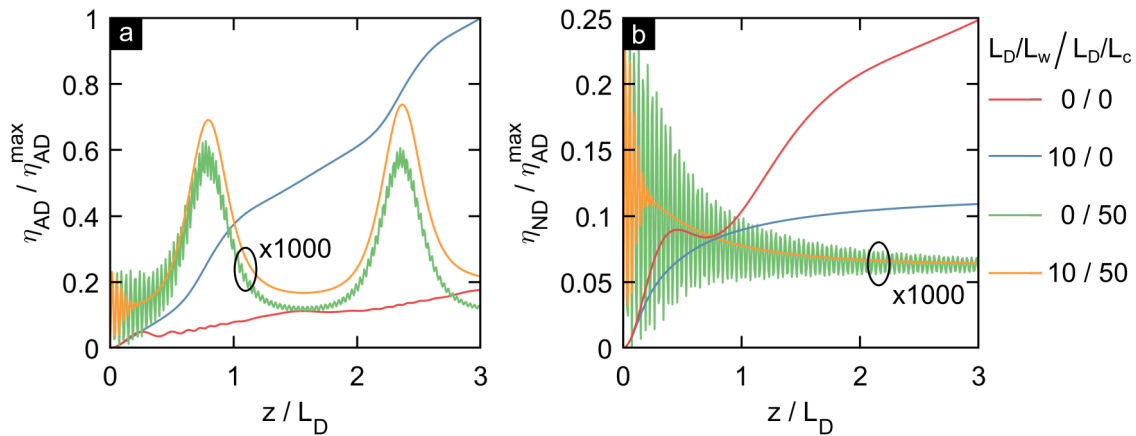
Fig. 17: Evolution of efficiency for AD (a) and ND (b) domain normalised by maximal efficiency. η is defined as ratio of pulse energies and $\eta_{AD}^{\max} = 5 \cdot 10^{-4}$. Cases including phase mismatch ($L_D/L_c = 50$) are multiplied as indicated. Legend applies to both panels.

The introductory examples show that efficiency crucially depends on phase matching and pump power evolution even in case of the relatively low maximum conversion of $\eta_{AD}^{\max} = 5 \cdot 10^{-4}$. These conditions justify the application of the *undepleted pump approximation*, i.e. neglect feedback of the harmonic. In the AD domain clear boosts in conversion are observed shortly after temporal compression took place (blue, green, yellow), for cases with sizable phase mismatch (green, yellow), back conversion occurred whereas GVM hinders reflow of energy partially due to reduced temporal overlap. For the phase matched cases (blue, red) the greater efficiency in case of GVM is attributed to lesser net dephasing due to SPM and XPM during temporal compression due to the accumulated delay. In the ND domain the situation more reflects common

expectations, i.e. best conversion is achieved if phase mismatch is zero across a large bandwidth, i.e. $\Delta \beta_0 = 0$ and GVM $= 0$.

Albeit not decaying during propagation when perturbed by THG, higher order solitons typically fission into their fundamental constituents under the emission of weak radiation that disperses; a process exploited in SCG often mediated by, e.g. third order dispersion or a retarded response. Detailing this intriguing process to its full extent is beyond the scope of this work and the interested reader is referred to the literature, e.g. [69,70] for general review, and the thesis by M. Chemnitz [116] and articles [39,49] with particular emphasis on experimental demonstration and numerical investigation of solitons in retarded media such as liquid filled fibres.

3.3.1.4 Pump Evolution with Molecular Nonlinearity and Anomalous Dispersion

In the following, selected cases of evolution in presence of retarded responses under otherwise equal conditions are considered since the pump evolution plays a crucial role in the THG process. It is to note here that the choice of a specific response necessitates the choice of a specific pulse duration as both functions are evaluated on the same grid and hence their relative widths must be considered.

Whereas T_0 was a free parameter in the former case, here the pulse duration results from two aspects of the simulation; first the grid is chosen to accommodate delays of $\pm 100\, T_0$ due to GVM in coupled equations, and second it is chosen to cover a range of $\pm 10\, \tau_f$ for the CS$_2$ response in SI units. This yields a physical pulse duration T_0 of $0.1\, \tau_f = 161\, \text{fs}$, or $284\, \text{fs}$ FWHM. Similarly, desired pulse duration and temporal response extent can be converted to the required normalised grid size. After evaluating the response in physical units it is normalised to the respective temporal simulation grid maintaining its ratio of nonlinearities.

Fig. 18 illustrates evolution of an $N = 2$ sech-pulse in the AD domain comparing CS$_2$ (a, d), C$_2$Cl$_4$ (b, e), and SiO$_2$ (c, f). In the latter case the shift of a Raman soliton is apparent, the initial compression stage extends up to L_D/N [82] after which fission takes place and the pulse decays into a soliton of greater power and shorter width under emission of residual radiation [117]. A qualitatively very similar effect is observed for molecular responses, the pulse contracts and exhibits intensity enhancement. Although in none of the examples the peak intensity is maintained, in case of C$_2$Cl$_4$ a shorter and more intense pulse emerges after fission, similarly to the case of SiO$_2$. Note that the

ratios of nonlinearities $n_{2,R}/n_{2,el}$ is almost two orders of magnitude greater than in the case of silica, yet this is not a measure of additional NLP due to the response and hence does not fully contribute to the steepness of the NLPs gradient due to the convolution in the nonlinear term. The ratio of nonlinearities in case of silica as stated in the caption results from its established molecular fraction as $f_R/(1 - f_R)$ in accordance with the nomenclature used to define N solely via $n_{2,el}$.
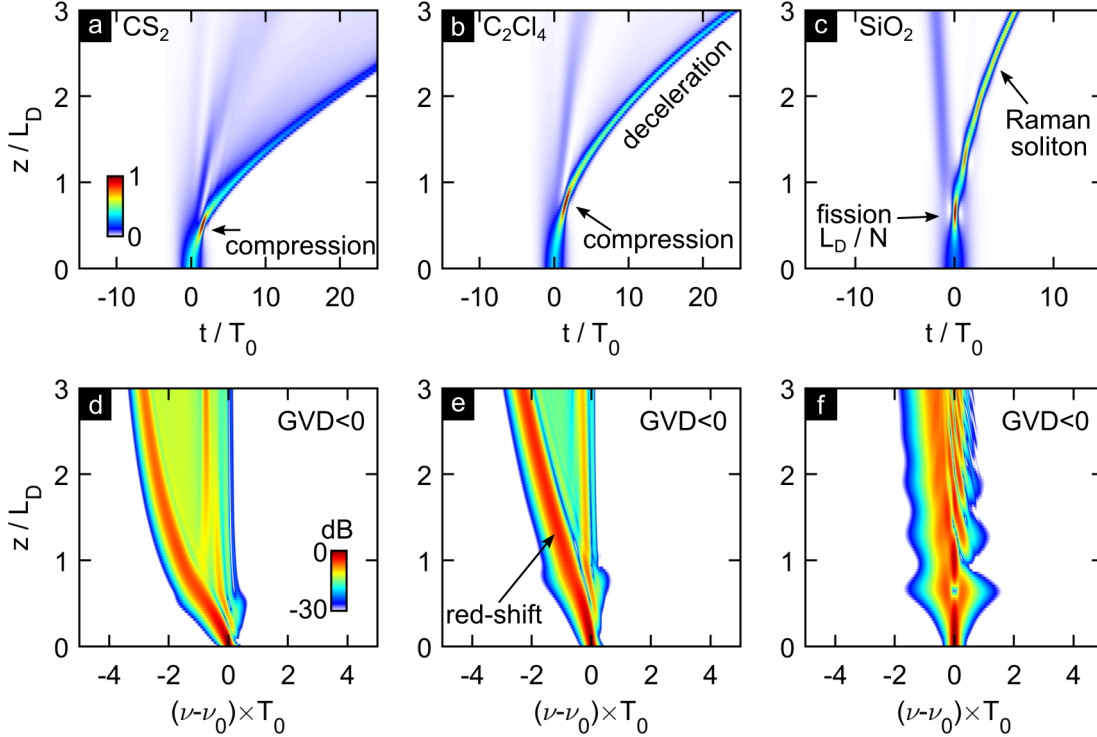
Fig. 18: Temporal (top) and spectral (bottom) evolution of a $N = 2$ soliton, $T_0 = 161$ fs in the AD domain in presence of the material response of CS_2 (a, d), C_2Cl_4 (b, e), and silica (c, f). The colour scale applies to all panels in one row. The ratios of nonlinearities $n_{2,R}/n_{2,el}$ are 17.5 (CS_2), 13.3 (C_2Cl_4), and 0.22 (SiO_2). Initial compression is indicated for all responses after which the pulse decays. All cases exhibit a red-shift, indicated exemplarily in (e) leading to deceleration of the wave. (a) and (b) exhibit similar evolution to the Raman soliton in (c) although dispersion is not fully compensated particularly for CS_2.

As was discussed in section 3.2.2 frequency down-shift due to any kind of causal response is expected and is observed accordingly. Due to the frequency shift the spectrum evolves into a region of increasing group index, i.e. lesser group velocity resulting in deceleration as indicated after the compression event. Apparently the fission length depends on the response parameters which further influence propagation beyond fission. Here the model from [39] was used for C_2Cl_4, if the model of [88] is deployed frequency down-shift is less pronounced whereas temporal spreading is similarly strong as in case of CS_2. It may be established that compression, or fission, occurs earlier for larger contribution of the nonlinearity, that is larger $n_{2,R}/n_{2,el}$ as in

case of CS_2 compared to C_2Cl_4. Further attention should be paid to the temporal axis extent. The Raman soliton emerging in the silica case shifts at an inferior rate compared to the molecular responses which is also reflected in the steeper red-shift in (e) and (d).

3.3.1.5 Pump Evolution with Molecular Nonlinearity and Normal Dispersion

Evolution dynamics of a sech-pulse with $N = 2$ launched in the ND domain are illustrated in Fig. 19 for CS_2 (a, d), C_2Cl_4 (b, e), and SiO_2 (c, f) as in the previous figure.
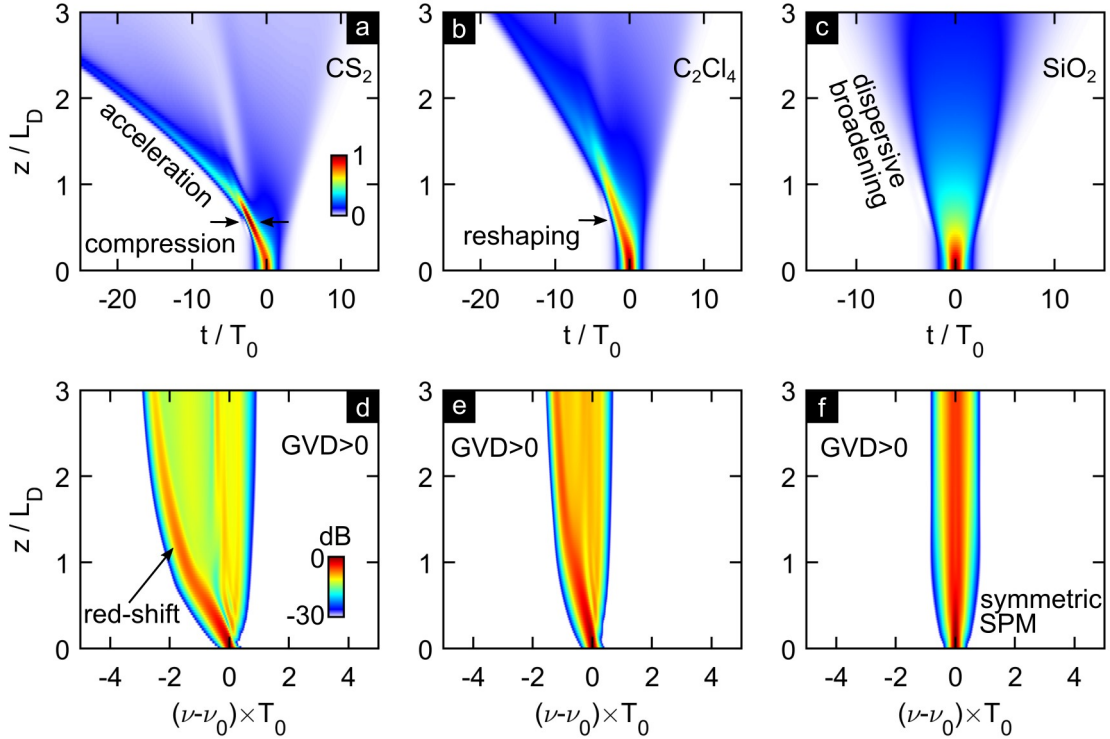
Fig. 19: Temporal (top) and spectral (bottom) evolution of a $N = 2$ sech pulse, $T_0 = 161$ fs in the ND domain in presence of the material response of CS_2 (a, d), C_2Cl_4 (b, e), and silica (c, f). The colour scale applies to all panels in one row. The ratios of nonlinearities as in Fig. 18. Initial compression is indicated in (a) forming a new intensity peak. In (b) the pulse reshapes to a peak with extended pedestal. In case of silica dispersive pulse broadening is observed.

In comparison of ND and AD domain the case of silica exhibits a major difference, as NLP and GVD no longer compensate each other a short initial stage accompanied by SPM induced broadening leads to rapid pulse spreading. In contrast, in case of molecular responses qualitatively similar dynamics as in the AD domain can be observed, particularly the spectral evolution resembles the former case, i.e. exerts a red-shift, temporal compression occurs for CS_2 more dominantly as a global intensity peak is formed on a wider pedestal. The wave with red-shifted spectrum accelerates due to declining group indices for lower frequency. These initial dynamics deviate substantially

from those of purely electronic systems and have to be ascribed to the molecular response.

3.3.1.6 Harmonic Evolution with Molecular Response and Anomalous Dispersion

In Fig. 20 a selection of PM parameters and the resulting evolution dynamics of the harmonic wave are illustrated for the case of pumping in the AD domain including the retarded response of CS_2 exemplarily as in Fig. 18 (a, d). The pump evolution is not altered from the cases shown above. The different ratios of L_D to L_W and L_C exhibit substantial impact on the TH and are stated in the panels.
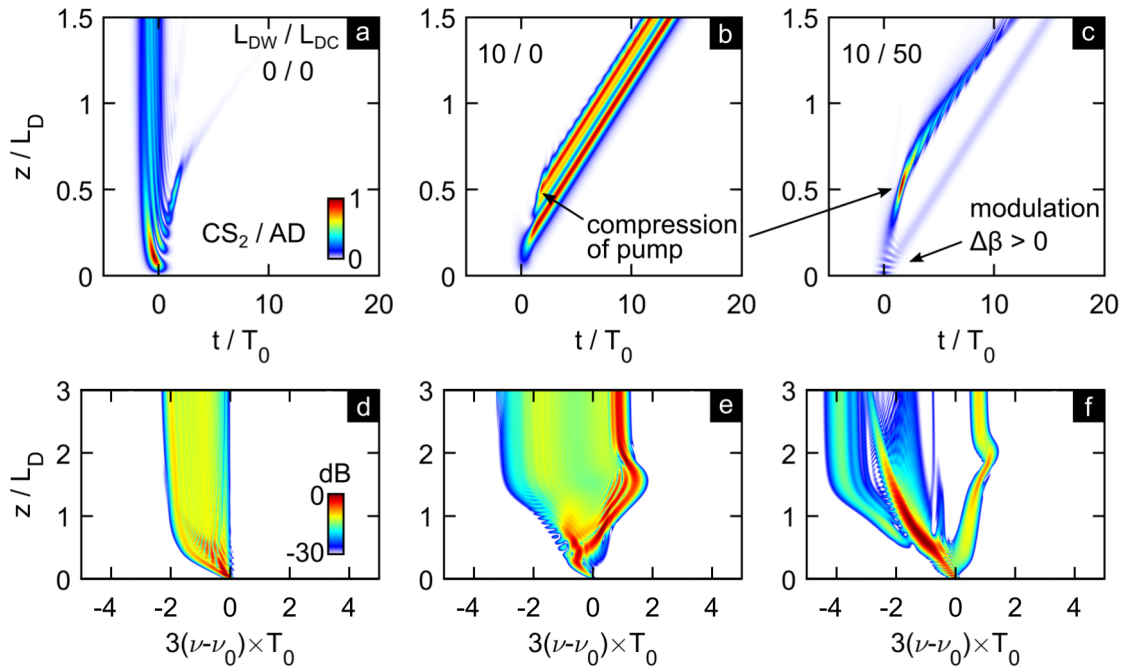
Fig. 20: Temporal (top, linear scale) and spectral (bottom, log-scale) evolution of harmonic wave pumped in AD domain by a $N = 2$ sech-pulse, $T_0 = 161\,\text{fs}$ for ratios $L_{DW} = L_D/L_W$ and $L_{DC} = L_D/L_C$ as stated in the top row. Vertical axis at top is truncated for visibility.

Whereas the spectral evolution can hardly be interpreted, the temporal domain allows for more insight into the generation dynamics. As was shown in Fig. 18 (a) the pump decelerates and compresses, the resulting intensity peaks can be observed as a delayed arm in (a), as the net GVM is actually negative due to the delayed pump. In (b) and (c) in particular, the pump's compression point is highlighted and generates a secondary TH wave after the typical initial signal. In (c) GVM is chosen such that the TH still trails the pump and propagates at approximately the same velocity, i.e. the initial and secondary wave trajectories are almost in parallel. Before, however, the indicated modulations which result from $\Delta\beta$ cease due to temporal delay. The generation efficiencies for cases (b, e) and (c, f) are much inferior to the case of perfect PM.

3.3.1.7 Harmonic Evolution with Molecular Response and Normal Dispersion

Evolution dynamics of the harmonic wave originating from a pump (see Fig. 19 (a, d)) in the ND domain are presented in Fig. 21 for the dispersive conditions stated in each panel. Due to the retarded response the pump pulse compresses initially which is evident in the temporal domain evolution in (a) and (b). Due to the red-shifting pump the net GVM is altered and the pulse walks off for GVM = 0 as in (a). An attempt of matching group velocities is shown in (c) which also leads to more XPM as the bandwidth enhancement suggests.
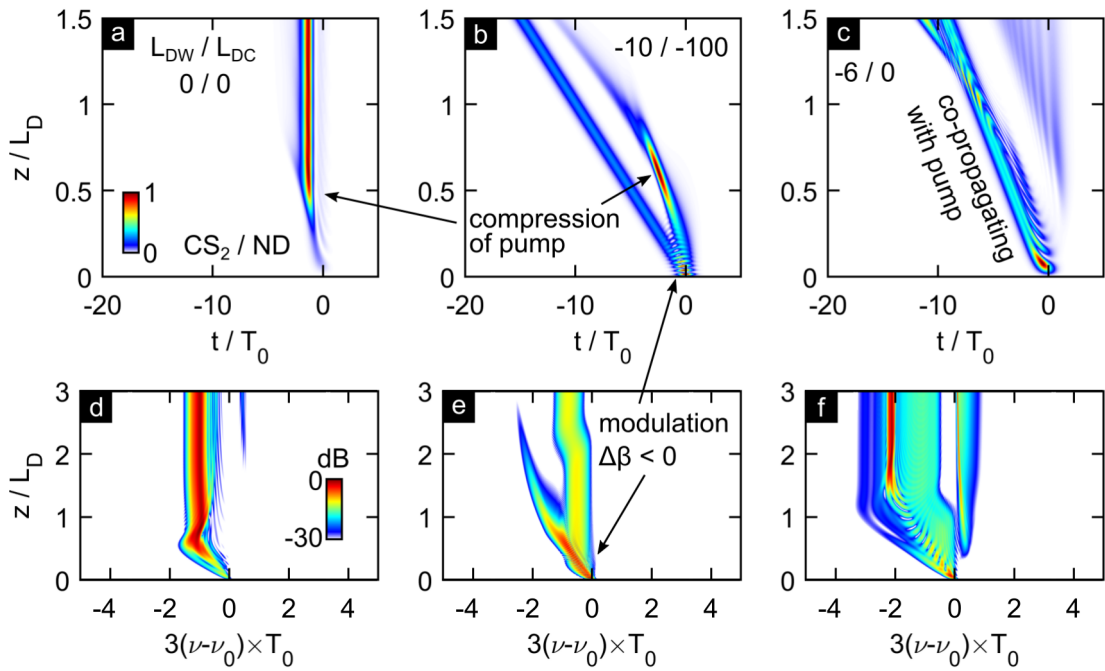
Fig. 21: Temporal (top, linear scale) and spectral (bottom, log-scale) evolution of harmonic wave pumped in ND domain by a $N = 2$ sech-pulse, $T_0 = 161$ fs for ratios $L_{DW} = L_D/L_W$ and $L_{DC} = L_D/L_C$ as stated in the top row. Vertical axis at top is truncated for visibility.

The shown dynamics provide an overview of the rich interplay even at the reduced level of complexity as higher orders of dispersion were not yet considered. Whereas dispersion of third order allows steering the pump in time domain, its impact on conversion efficiency was found to be marginal compared to phase matching. In the following section the effect of $\Delta\beta_0$ and GVM are studied in an extended range of parameters focusing on conversion efficiency.

3.3.2 Efficiency Considerations of THG with Retarded Response

To aid design considerations for experimental implementation and identify possible deviation from the established PM concept of linear dispersion, the ratios L_D/L_W and L_D/L_C are investigated in a larger range in both ND and AD domains. Sech-pulses with $N = 1$ and $N = 3$ and duration $T_0 = 161$ fs are deployed. After propagation of 2 L_D, i.e. a distance after which peak power substantially decayed in presence of GVD, the efficiency is evaluated and results are gathered in Fig. 22. The ND domain is shown on the left and AD on the right. Panels (a-d) include the retarded response of CS_2 exemplarily which is removed for examples (e, f).
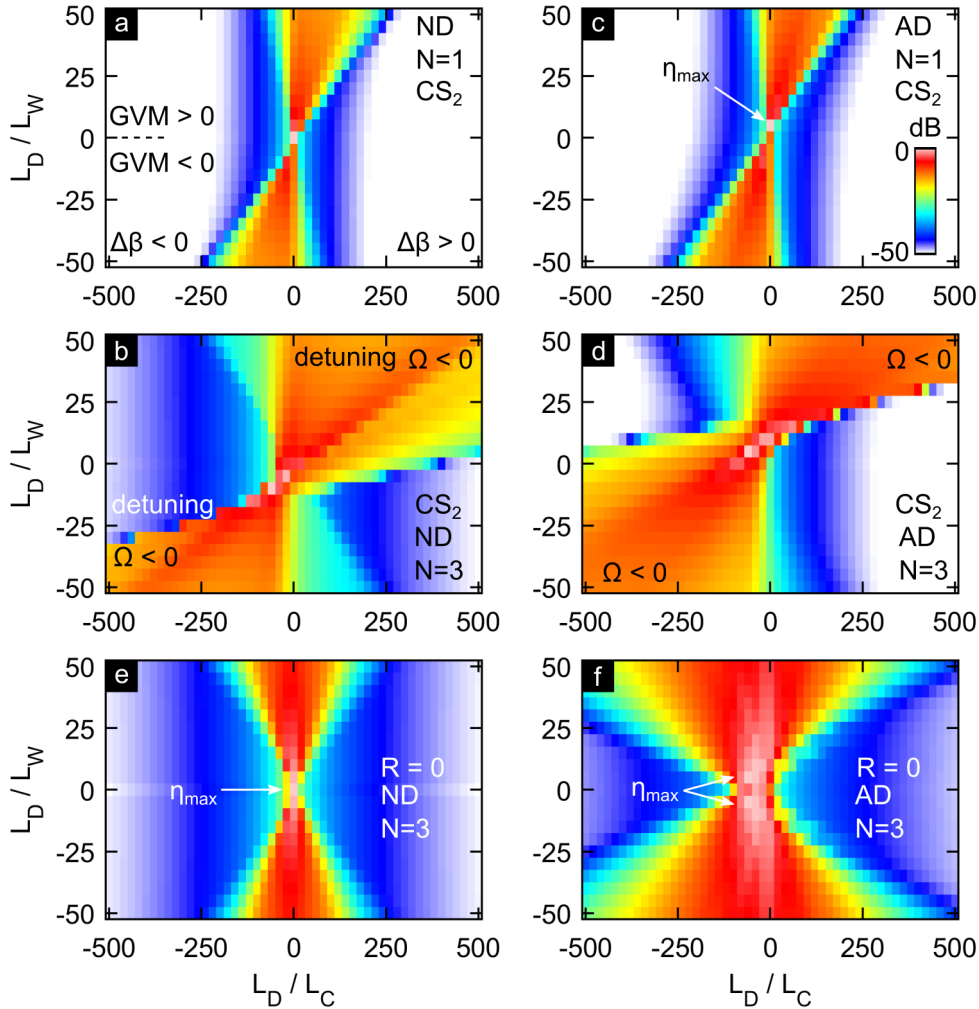
Fig. 22: Normalised efficiency η in log-scale when pumping in the ND (left column) and AD (right column) domain. (a-d) include the response of CS_2, (e-f) are purely electronic (R=0). Powers are indicated as N in each panel. The detuning, $\Omega = 3(\omega - \omega_0)$, represents the shift from the pump pulse centre angular frequency for the harmonic. Area of positive/negative group and phase mismatch is indicated in (a).

Efficiencies from above are normalised and shown in dB-scale. The colour bar in (c) applies to all panels. The respective regimes of mismatch represented by the ratios of

length scales (note L_D is always positive) are indicated in (a). A similarity among all configurations is the central peak location. Despite a small displacement towards positive GVM in case of (c) and the double hump observed in (f) a common trend of higher efficiency for reduced mismatch remains, nevertheless. The dual hump in (f) for the ideal $N = 3$ soliton indicates NLP shifts deteriorate conversion upon co-propagation.

The electronic ND case (e) forms the shape of an hourglass without preferential PM conditions when deviating from the centre unlike the cases including retardation. In both AD and ND the upper and lower triangles bend towards negative detuning from the pump central frequency which is indicated in (b, d) and is represented by $\Delta\beta/GVM > 0$. The cause is found in the pumps tendency to frequency down-shift due to the response.

Within the limits of the above analysis it may be established that despite the presence of SPM and XPM the common PM conditions should be met for optimal signal yield. Deviation from optimum should preferentially allow detuning towards lower frequency, i.e. longer wavelengths, due to enhanced spectral broadening towards lower frequencies of the pump caused by the non-instantaneous response.

3.3.3 Numerical Investigation of Experimental Conditions

In this subsection simulations are conducted in view of experimental realization – in this perspective, conditions and waveguide properties closely resembling those which are experimentally accessible are in focus. Since the previous analysis validated that established concepts of phase matching are fully applicable, the remaining waveguide properties, such as higher orders of dispersion or nonlinear overlap integrals, are determined in favour of accomplishing phase matching. The details and design considerations are presented in chapter 4 – here, one specific waveguide configuration is investigated to guide experimental execution by revealing potential impact of pulse parameters and to preview evolution dynamics. The analysis serves to provide characteristic benchmark figures that are experimentally accessible as well as confirming experimental feasibility.

The waveguide configuration of choice is a 3.4 μm core C_2Cl_4 filled fibre as deployed in section 4.3.1. Numerical simulations presented in this subsection resort to a set of coupled GNLSE scaled in the SI unit system for convenience. Dispersive properties are

described by constant expansion coefficients rather than a set of length scales which include a dependence on pulse duration.

Throughout the remaining section simulations deploy dispersive properties of the pump as listed in Table 2. Higher orders of dispersion for the harmonic were found to have negligible effect as dispersion is dominated by the linear term due to GVM.

Table 2: Simulation parameters for a 3.4 μm liquid core of C_2Cl_4 [39,118].

λ_0 [μm]	GVM [fs/mm]	β_2 [fs²/mm]	β_3 [fs³/mm]	β_4 [fs⁴/mm]	$J_{SPM} = J_{XPM}$ [μm⁻²]	J_{THG} [μm⁻²]
1.56	320	32	85	-215	0.1	0.002

3.3.3.1 Bulk Loss and Reduction of Conversion

For the practical application material absorption can limit performance in general. In order to assess its impact in the present case simulations with multiple bulk absorption values are conducted. The efficiency in terms of energy conversion is calculated and shown in Fig. 23 (a). The dashed line corresponds to the experimental bulk loss of the liquid and coloured lines show artificially increased losses and the resulting relative reduction of efficiency is given in (b). It is shown that the reduction is negligible in the experimental case (less than 2 % less conversion) and that loss as high as 30 dB/m results in less than 40 % reduction in efficiency. Although conversion rapidly saturates within the first 2 cm of the fibre ($P_0 = 3$ kW, $T_0 = 510$ fs), sample lengths suitable for convenient handling do not deteriorate conversion efficiency in practice.
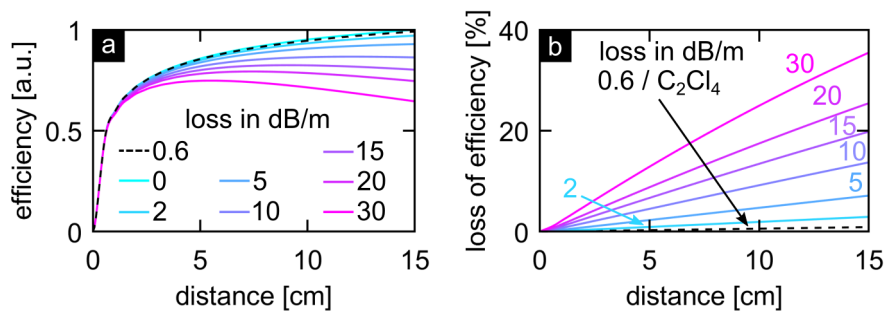
Fig. 23: Impact of loss on THG efficiency. (a) Evolution of normalised efficiency of a 3 kW sech pulse ($T_0 = 510$ fs) for different amounts of loss. 0.6 dB/m corresponds to the experimental bulk absorption of C_2Cl_4 at 532 nm. (b) Relative reduction of efficiency with respect to zero loss.

3.3.3.2 The Influence of Group Delay Dispersion

Under laboratory conditions pulses emitted from a laser need not be transform limited, i.e. their temporal shape is not optimally compressed to the minimal temporal width. Particularly beam routing, power adjustments and coupling optics, e.g. lenses, lead to accumulated spectral phase and dispersive spreading of a pulse.

Here, the effect of externally acquired second order spectral phase, i.e. group delay dispersion (GDD), on THG efficiency is investigated. Pulse propagation with varying initial pulse widths but constant peak power is simulated. GDD was applied to the pulse after initialising which leads to a reduction in peak power due to an increased width and frequency chirp. The pulse energy in each case of GDD remains constant. Due to the constant peak power pulses with initially greater length are more energetic.

In Fig. 24 (a) the full width half maximum (FWHM) pulse width which results due to GDD is shown for various initial FWHM. Note that $\pm$GDD leads to the same pulse width, yet opposite frequency chirps. The legend in (a) also applies for (b-d).

Panels (b-d) present the efficiency evaluated after propagating 10 cm for five cases of phase mismatch $\Delta\beta$. In each case the impact of GDD is noticeable and it is more pronounced for shorter pulses whose width is more strongly affected by the same amount of GDD. Apart from the initial 200 fs pulse a clear maximum in efficiency is formed for which GDD < 0 in all cases. The reason why negative GDD is preferable is due to the normal dispersive fibre ($\beta_2 > 0$), which allows balancing dispersive spreading initially as will be shown below. Despite the inherent reduction in peak power due to the initial spectral phase, more than 100 % enhancement of efficiency is possible in case of 30 fs pulses regardless of the phase matching conditions.

Albeit showing little susceptibility to GDD, the case of 200 fs pulses exhibits remarkably strong dependence on $\Delta\beta$ as the conversion efficiency drops by an order of magnitude for $\Delta\beta = -10$ mm^{-1} and even more for $\Delta\beta = -25$ mm^{-1}. The cause is the limited initial coverage of the phase matched wavelength λ_{PM}. The inertial response causes considerable initial red-shift of the pump spectrum. Therefore negative detuning, i.e. phase matching to wavelengths greater than λ_{PM}, is preferred over the opposite case and is observed even for shorter pulses, although the effect is less pronounced.
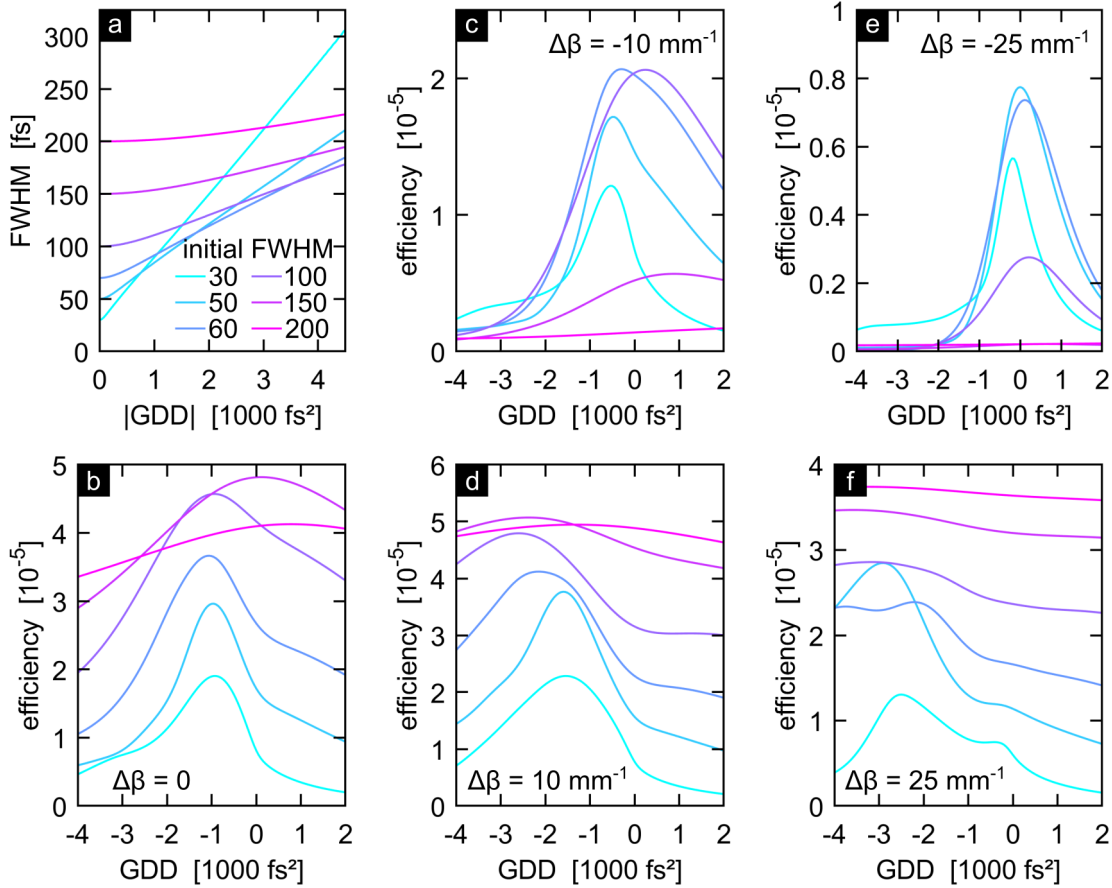
Fig. 24: Efficiency dependence on initial group delay dispersion (GDD) for various pulse widths. (a) Resulting FWHM for increased absolute GDD. The legend applies to all panels. (b-f) Efficiency at the end of a 10 cm fibre filled with C_2Cl_4 under experimental conditions. Pulses are initialised with $P_0 = 10$ kW in the ND domain (1.56 μm) and GDD is applied thereafter including intensity reduction in simulation. The phase mismatch considered is stated in panels (b-f).

According to both (b, d) an optimal GDD amounts to approximately -1000 fs^2 for pulses below 100 fs, whereas this suggest a favourable pulse duration in the range 75 fs to 90 fs (see area of multiple intersections in (a) for GDD $= 1000$ fs^2) it is to note that the pulse chirp is essential for an enhancement in efficiency. For larger positive phase mismatch (f) greater negative GDD is beneficial, yet longer pulses exhibit less pronounced maxima in efficiency.

Fig. 25 illustrates the dynamic evolution in case of $\Delta\beta = 10$ mm^{-1}. (a) and (b) show how a 30 fs pulse evolves along the fibre without (a) and with -1000 fs^2 GDD. The transform limited case exhibits rapid temporal dispersion, whereas spectral broadening (c) is saturated within the first centimetre of the fibre. In contrast, the chirped pulse exhibits lower peak power, compresses at first to a level of 4.75 kW, which is still substantially below the peak power of case (a) amounting to 10 kW, and disperses thereafter. In the spectral domain narrowing accompanied by a red-shift is present until compression completes. The evolution of efficiency (e) for the two cases (black and red)

is shown together with an unchirped pulse (blue) of identical width and peak power as the chirped pulse. THG energy steeply rises at first but soon stagnates for the unchirped pulse (black), the same pulse chirped by -1000 fs^2 (red) exhibits less steep signal increase due to the reduced peak power closely following the trajectory of the unchirped pulse of identical width until yield is substantially boosted beyond the level of the intense short pulse. The interplay of pre-compensated dispersion and spectral narrowing enhancing power density nearby λ_{PM} possibly lead to the increase of η.

The resulting THG spectra (f) are affected in location, width and overall shape by these changes in peak power, pulse chirp and duration. A reasonable explanation for the shift of the THG in case of the chirped pulse (red) with respect to the other cases is phase accumulated by XPM during the extended distance of signal generation before and after the compression point which, as shown in earlier sections, can lead to blue-shift.
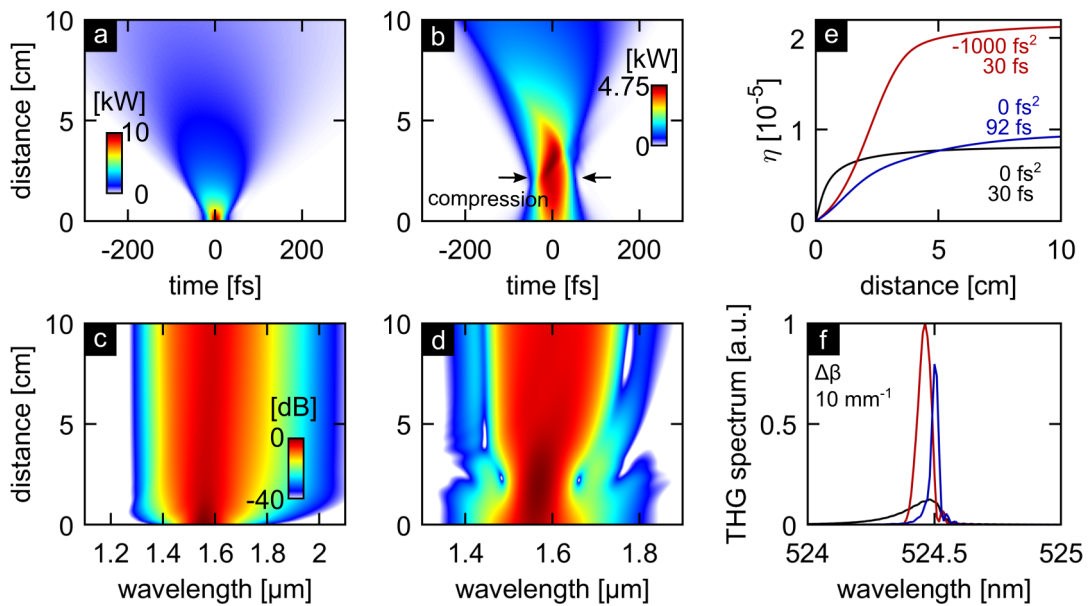
Fig. 25: Temporal and spectral evolution for a 30 fs (FWHM) pulse with GDD = 0 (a, c) and GDD = -1000 fs^2 (b, d). Colour scale from (c) applies to (d). (e) Conversion efficiency for the transform limited pulse (red), the same pulse with GDD (black) and a transform limited pulse with identical peak power and width as in case of GDD (P_0 = 3.62 kW, FWHM = 92 fs). (f) THG spectra (linear scale) resulting from the three different pulses.

3.3.3.3 Power Dependent Spectral Evolution

The dynamic evolution along the waveguide is difficult to access experimentally. Recording the evolution by cutting the fibre to shorter lengths leaves an open end in case of liquid core fibres. Evaporation is inevitable and steady experimental conditions can hardly be achieved. An alternative approach to investigate nonlinear dynamics is recording output spectra for successively increased powers. Modelling results for experimentally available laser systems are presented in Fig. 26 to assess feasibility and characteristic spectral features in experiments.
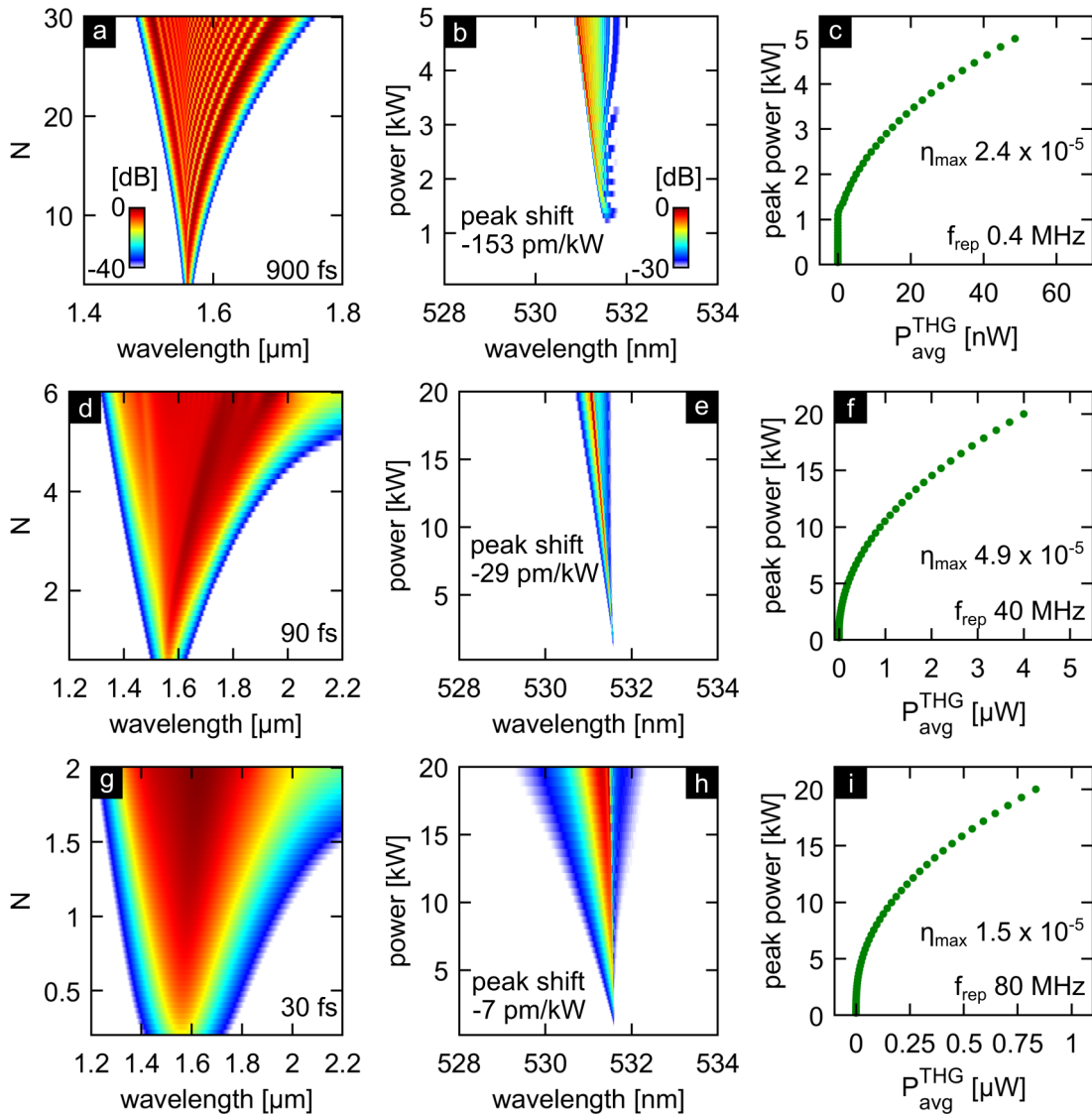
Fig. 26: Numerically obtained power spectral evolution during THG in a 15 cm long C_2Cl_4 LCF with parameters as in Table 2 and $\Delta\beta = 25.3$ mm^{-1} to match the experimental λ_{PM}. Columns represent pump spectra (left), TH spectra (centre), and average power of TH (right) for pump pulses of 900 fs (top), 90 fs (centre), and 30 fs (bottom) assuming the respective repetition rates of the pump lasers. Vertical axes (left and centre) are identical and represent soliton number and peak power, respectively. Colour scale applies to each panel in respective column.

For experiments lasers delivering pulses of 30 fs, 90 fs, and 900 fs (FWHM) are available. Considering the given fibre dispersion and typical power levels readily achieved in prior work on SCG in liquid filled fibres, panels (a, d, g) present the expected dynamics of spectral broadening. The vertical axes show the respective power as soliton number (equivalent peak powers are given in centre column) to assess the relative contributions of dispersion and nonlinearity in these cases. The relatively stronger dispersive effects lead to smooth spectral broadening in the normal dispersive domain ($\lambda_{ZD} = 1.95\ \mu m$) for 30 fs and 90 fs, whereas rather clean SPM structure can be observed in the case of 900 fs pulses whose dispersive length scale substantially exceeds the sample length. The expected trend to red-shift is also present.

Spectra of the generated harmonic (b, e, f) are centred near 532 nm initially due to $\Delta\beta = 25\ mm^{-1}$ providing phase matching at a red-shifted wavelength similar to the experimental configuration discussed in the next chapter. Further, all spectra exhibit a shift towards shorter wavelength for increasing powers, although Eq. (25) suggests the opposite. As established in section 3.2.4 propagation subsequent to generation leads to XPM which more than compensates the opposite detuning. The particular rates at which the harmonic shifts are given in the panels. The rate is highest for the longest pulse maintaining its intensity throughout the sample producing a long-tailed trailing NLP. Intensities of the short pulses are reduced more rapidly also due to higher spectral broadening rates.

For all cases, an efficiency of the order $1 - 5 \times 10^{-5}$ is expected for the fibre configuration. Since damage thresholds in terms of both peak power and fluence are largely unexplored, it is hardly possible to unambiguously identify the optimum pulse. Panels (c, f, i) show the expected average powers of the TH signal accounting for the respective laser repetition rates. The average power is of importance since direct measurements are preferentially performed with power meters based on sensitive photo diodes. More sensitive equipment such as photo multipliers seem unnecessary even in case of the longest pulses. Power levels of 10-20 nW are detectable with standard equipment and can be reached at peak powers of 2 kW – 3 kW suggesting that each pump pulse configuration is promising to achieve THG experimentally.

4 Third Harmonic Generation in Liquid filled Step Index Fibres

This chapter is devoted to the experimental part of the thesis. Considerations towards waveguide design are in focus of the first subsection. The selection process of core liquids is described first followed by a phase matching analysis in 4.1 utilising methods outlined in chapters 2.2 and 2.4. Details of the experimental setup are provided in 4.2. Subsection 4.3 comprises studies conducted in fibres with circular core. To that end, lasers delivering pulses with different durations in the sub-picosecond domain were selected to target propagation regimes with different amounts of molecular contribution to the nonlinearity as will be discussed in the respective sections. An analysis of core ellipticity and the resulting birefringence is presented in section 4.4. The potential of active tunability during operation by external temperature control is explored in 4.5. Finally, the accomplished long-term durability of liquid filled fibres is presented in 4.6 highlighting their future prospects in applications.

4.1 Liquid Core Materials

Despite the large number of liquids that are available to form liquid core fibres (LCFs), wide transparency for the desired pump and harmonic range cannot be achieved with every liquid. For successful harmonic generation experiments, both reliable pump sources and detection for both the pump and harmonic spectral ranges are necessary. Since material absorption towards the ultraviolet limits the harmonic spectral range to greater than 400 nm, the most promising pump sources operate in the telecom domain. This spectral range around 1.56 μm can be accessed with mature laser technology and detection equipment, whereas the resulting harmonics are in the visible range that also allows for convenient and sensitive detection of signals.

The requirements for liquid candidates can be established as follows:

1) High transparency in both visible and near infrared

2) Large molecular contribution to the nonlinearity

3) High refractive index compared to silica

4) Ideally well characterized optical properties

Since the focus is on studying the molecular contribution in the harmonic generation process, the molecular structure is important to consider. Symmetrical molecules exhibit an isotropic polarisability and their nonlinear response is dominated by the electronic

effect. In contrast, elongated molecules exhibit an anisotropic polarisability which will lead to a time dependent dipole that experiences torque in the excitation field. This molecular motion is the origin of non-instantaneous nonlinear responses.

Among others, carbon disulphide (CDS, CS_2) exhibits an extraordinarily large molecular contribution to its nonlinearity and therefore was in focus of recent and former nonlinear frequency generation experiments. Further, the response of CS_2 is a role model of a non-instantaneous response and thoroughly characterised [34,87]. Tetrachloroethylene (TCE, C_2Cl_4) is a promising candidate also which to date was much overlooked but its response was recently characterised as well [88] and already exploited in supercontinuum generation experiments [39]. Benzene derivatives such as toluene ($C_6H_5CH_3$) and nitrobenzene ($C_6H_5NO_2$) also exhibit a high molecular nonlinearity [35] and recently served as nonlinear fibre core material, e.g. in Refs. [42,44,54,119–121].

4.1.1 Absorption in Selected Nonlinear Liquids

To fully exploit the propagation lengths provided by the fibre geometry, absorption in the liquid core material must be kept minimal. Losses in CS_2 and C_2Cl_4 were characterised from the visible to short-wave-infrared without further treatment of the chemicals after withdrawal from their repository. Absorption measurements are based on spectrally resolved transmission data acquired for variable path lengths of the bulk liquids in silica cuvettes. Fig. 27 presents transmission data referenced to an empty path.
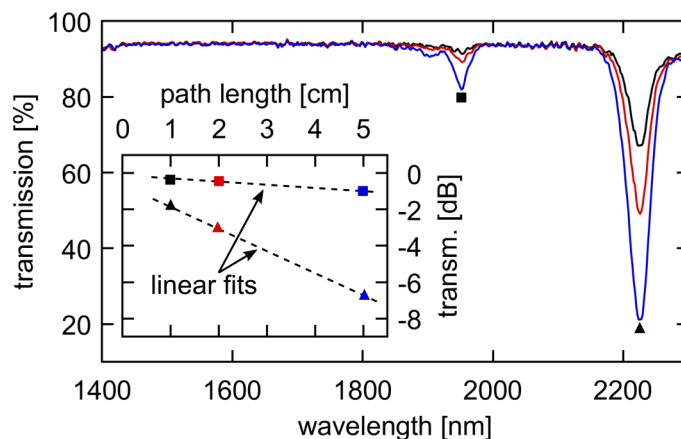
Fig. 27: Transmission data versus wavelength for CS_2 filled cuvettes with path lengths of 1 cm (black), 2 cm (red), and 5 cm (blue). A triangle (square) indicates the transmission dip at 2224 nm (1950 nm) which is shown in the inset versus path length. Dashed lines represent linear fits whose slopes correspond to absorption in dB/cm multiplied by -1.

For this example data of CS_2 is chosen using 1 cm, 2 cm, and 5 cm path length. Absorption can be retrieved by fitting a linear function for each individual wavelength as indicated in the inset exemplarily. Triangles (squares) represent data at 2224 nm (1950 nm) and the negative slope corresponds to absorption of 125 dB/m (12 dB/m).

The full range of data is shown in Fig. 28 including the absorption of CS_2 (orange) and C_2Cl_4 (blue) along with highly nonlinear benzene derivatives, toluene ($C_6H_5CH_3$, black) and nitrobenzene ($C_6H_5NO_2$, red). The latter two are scaled by 0.1 for better visibility, as their absorption coefficient was determined to be notably higher [122] particularly in the near infrared when compared to CS_2 and C_2Cl_4. Molecules containing C-H bonds exhibit infrared absorption due to stretching, bending and deformation modes whose overtones reach into the near infrared and are not considered further due to these losses. Although such absorption can be manipulated, i.e. pushed towards longer wavelength by exchanging hydrogen with heavier atoms [122], the impact of deuteration on dispersion is not fully researched and introduces further complications for practical use, such as deterioration by atmospheric water vapour.
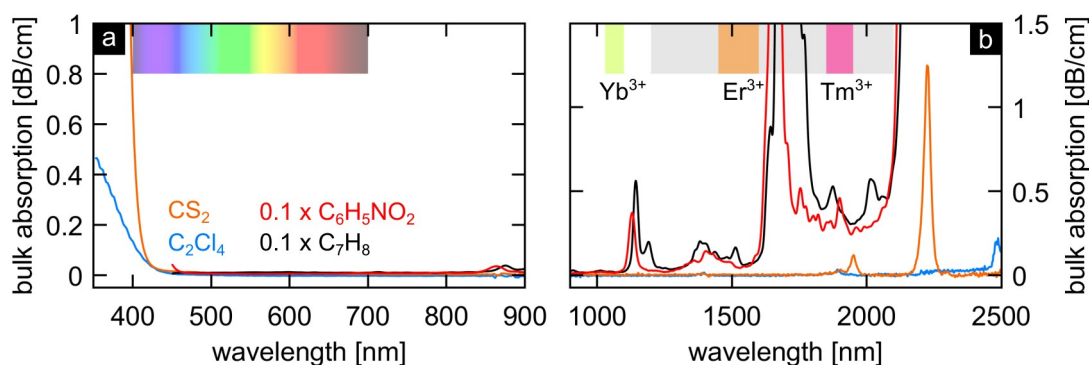
Fig. 28: (a, b) Liquid absorption for C_2Cl_4 (blue), CS_2 (orange), toluene (C_7H_8, black), and nitrobenzene ($C_6H_5NO_2$, red). Curves for toluene and nitrobenzene are scaled by 0.1 for better visibility, data taken from [122]. Note different y-axis limits for (a) and (b). Grey area in (b) corresponds to the visible light range shown in (a). Typical bandwidths of common laser ions are shown in (b).

It must be noted this list of liquid candidates is by no means exhaustive but already takes into account further constraints listed above, e.g. the sufficiently high IOR which rules out alcohols and ketones which also show limited transmission in the near-infrared.

4.1.2 The Nonlinear, Non-instantaneous Response in Molecular Liquids

As outlined in chapter 2.3.1 the nonlinear response in molecular liquids is a superposition of multiple effects commonly modelled by the functional forms given in Table 1. The latest response models for CS_2 [34,123] and C_2Cl_4 [88] are illustrated with all their constituents in Fig. 29 (a) and (b), respectively. Note, in case of C_2Cl_4, no collisional contribution is necessary to achieve good agreement between measurement and modelling in [88]. Generally, librational motion exhibits shorter decay times and accounts for the initial peak of the response whereas collisions between dipoles and the diffusive reorientation represent the slow decaying tail of the total response. Responses in (a) and (b) are normalised by the respective $n_{2,el}$ of the liquid revealing the enhancement of the nonlinear contribution to the IOR. CS_2 exhibits extraordinarily large molecular contributions among the molecular liquids characterised so far [124].

To assess its impact on the nonlinearly induced change of the IOR, Δn, and similarly the nonlinear phase (NLP, see Eq. (18) and Eq. (19) on p. 11) is evaluated for pulse durations deployed in experiments. The results are shown as red curves in panels (c) – (e) for CS_2 and (f) – (h) for C_2Cl_4 along with the initial pulse shape as dashes. Blue curves represent the instantaneous detuning from the carrier frequency due to phase modulation. The change of IOR is again normalised by the purely electronic effect and exhibits substantial changes trailing the pulse even in case of pulses with full width half maximum (FWHM) of 30 fs (c and f). For increasing pulse durations (90 fs in (d) and (g)) local minima in Δn are less pronounced as the pulse width approaches the rise times of the inertial effects (commonly set to 100 fs or 150 fs). Finally, in case of 900 fs (panels (e) and (h)), Δn is fully dominated by inertial contributions exhibiting a decaying tail of NLP. In contrast to purely electronic effects the detuning $\delta\omega \propto -\partial_t \Phi_{NL}$ is negative at the pulse centre and not symmetrical across the pulse shape but red-shifted. It is to mention that the pulse chirp, i.e. $\partial_t \delta\omega$, can be inferred from the detuning and on average remains positive across the pulse as in case of a purely electronic response. Yet, copropagating pulses, i.e. a pump and radiation created via THG, may alter their respective phase via XPM as was discussed in chapter 3.
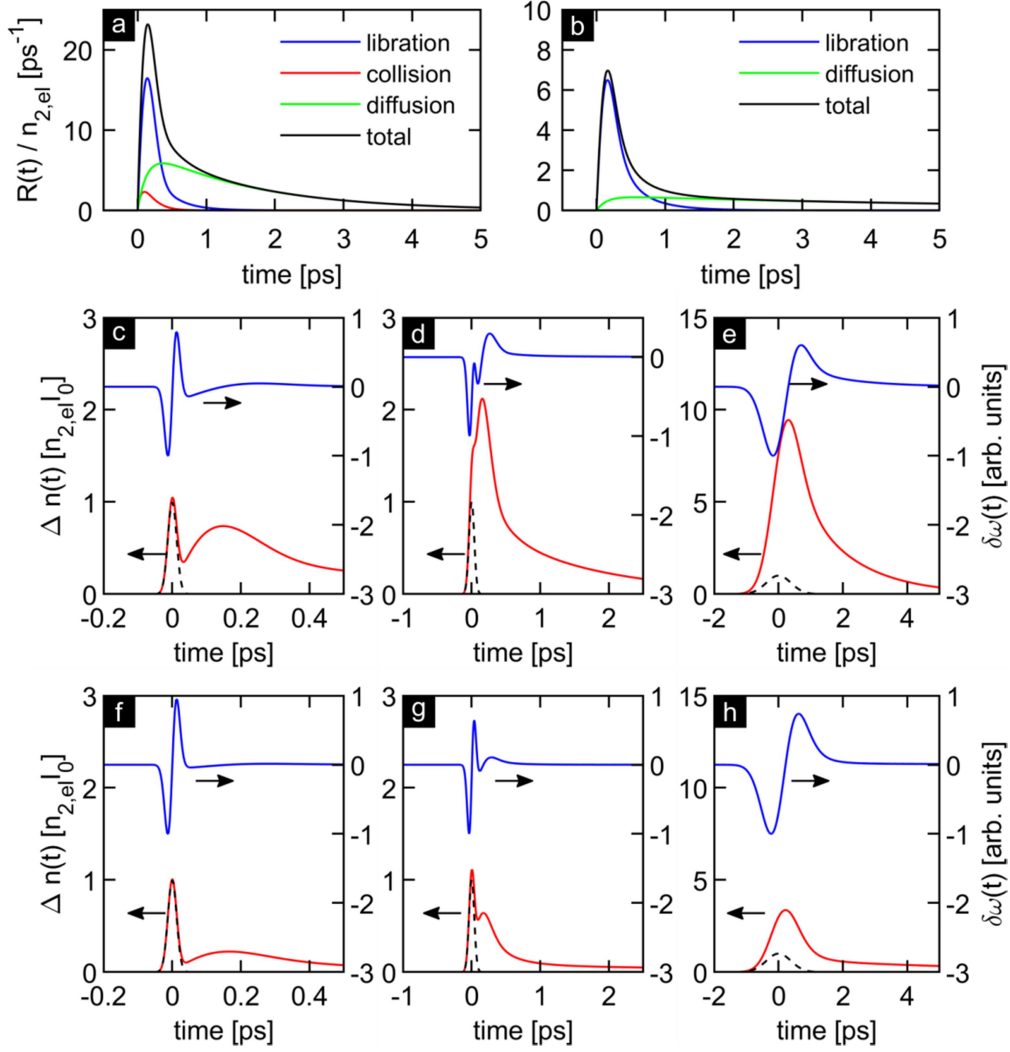
Fig. 29: Non-instantaneous response and its constituents for CS₂ (a) and C₂Cl₄ (b) normalised by the respective $n_{2,el}$. (c-e) Change of refractive index due to instantaneous and total non-instantaneous response of CS₂ (red, left axes, in units of $n_{2,el}I_0$) and frequency shift (blue, right axes, in arbitrary units). Pulses assumed for the convolution are shown as dashes with FWHM durations of 30 fs (c), 90 fs (d), and 900 fs (e). (f-h) same as (c-e) for C₂Cl₄.

Table 3 lists the parameters for the characteristic response function of C₂Cl₄ and CS₂ used to obtain the responses shown in Fig. 29 (a) and (b). C₂Cl₄ was only recently characterised by using the beam deflection technique [88]. A former model developed in [39] is shown in the table for comparison. All $n_{2,k}$ values are in 10^{-20} m²/W, rise and fall times $\tau_{f,r}$ in ps, ω_0, i.e. the librational resonance frequency, and σ, i.e. its bandwidth due to inhomogenous broadening, are given in ps⁻¹.

By comparing the different models for C₂Cl₄ an approximate factor of two in terms of nonlinear strength, i.e. higher values for $n_{2,k}$, shows that parameters for the material model are difficult to determine accurately, since both in [88] and in [39] very good agreement between experimental data and simulations was achieved using the respective model parameters.

Table 3: Response parameters for CS$_2$ and C$_2$Cl$_4$. Functional forms of the respective effects are given in Table 1, page 12. Nonlinear indices n_2 are given in 10^{-20} m^2/W, $\tau_{r,f}$ are in ps, and ω_0 and σ are in ps^{-1}.

effect	CS$_2$ [34,87]				C$_2$Cl$_4$ [39]				C$_2$Cl$_4$ [88]			
	n_2	τ_r	τ_f	ω_0/σ	n_2	τ_r	τ_f	ω_0/σ	n_2	τ_r	τ_f	ω_0/σ
electronic	15.2				5.52				3.87			
libration	76		0.57	8.5/5	20.8		0.78	4/6.3	10		0.65	4/6.5
diffusion	180	0.1	4.5		50.1	0.1	4.5		18	0.15	6.5	
collision	10	0.1	0.78		3.1	0.1	2.98		0			
max. f_R		92.47%				93.05%				87.91%		

In comparison to other known solvents [34,35,87], and CS$_2$ in particular, C$_2$Cl$_4$ exhibits a relatively large fall time for the diffusion component and at the same time either model corroborates a short temporal width of the librational component which manifests in in a L-shaped response with a low level extended tail. Both CS$_2$ and C$_2$Cl$_4$ represent excellent retarded nonlinear materials.

For completeness, the molecular fraction f_R for the above liquids is compared to silica (SiO$_2$) in Fig. 30. In contrast to a constant value of 0.18 for silica, the multicomponent response from [125] was used to evaluate $n_{2,\text{eff}}$ and finally f_R assuming Gaussian pulses.
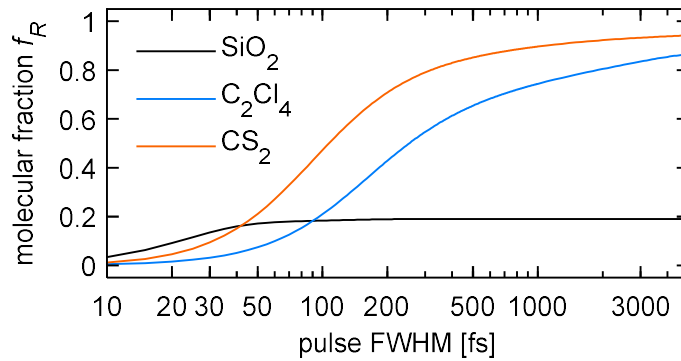
Fig. 30: Molecular fraction for CS$_2$, C$_2$Cl$_4$, and SiO$_2$ for Gaussian pulses. x-axis is logarithmic.

When probing the material response with pulses shorter than characteristic rise times, inertial effects cease to contribute, as expected. This effect is observed for silica, too. Interestingly, silica exhibits greater molecular fractions in the sub-40 fs regime than CS$_2$ and C$_2$Cl$_4$ due to the shorter rise times of its *Raman* response which is still probed by such short pulses. Fig. 30 shows that f_R = const. is a reasonable approximation only if the pulse duration is significantly larger than characteristic rise times and should not be applied for molecular liquids in the sub-picosecond domain.

4.1.3 Material Refractive Index

Material indices for the two core liquids and silica cladding are shown in Fig. 31 (a) (left axis) along with the resulting fibre NA (right axis). Curves are calculated based on the respective Sellmeier equations (silica [126], C_2Cl_4 [39,118], CS_2 [38]) defined as

$$n(\lambda)^2 = 1 + \sum_k \frac{a_k \lambda^2}{\lambda^2 - b_k^2}. \tag{39}$$

A peculiar and perhaps unique property of liquid core fibres is the local minimum of the NA (e.g. 900 nm for C_2Cl_4). The infrared absorption strength used in modelling the refractive index is much lower for liquids as compared to silica or most other glasses. This results in relatively large ZDW for the liquids and causes the increase in NA with potential of robust modal confinement towards mid infrared wavelengths reducing losses due to the silica cladding in this spectral domain.

Fig. 31 (b) shows that CS_2 and C_2Cl_4 are valid core materials as their referenced indices exceed the zero-line sufficiently. The number of modes guided in such high NA fibres can be very large in the visible range as indicated in the bar chart in Fig. 31 (c). However, the green portion of the bars indicates modes with azimuthal index equal to one, as in case of the fundamental pump mode. Only such modes will achieve reasonable modal overlap which reduces the higher the order of the respective mode.
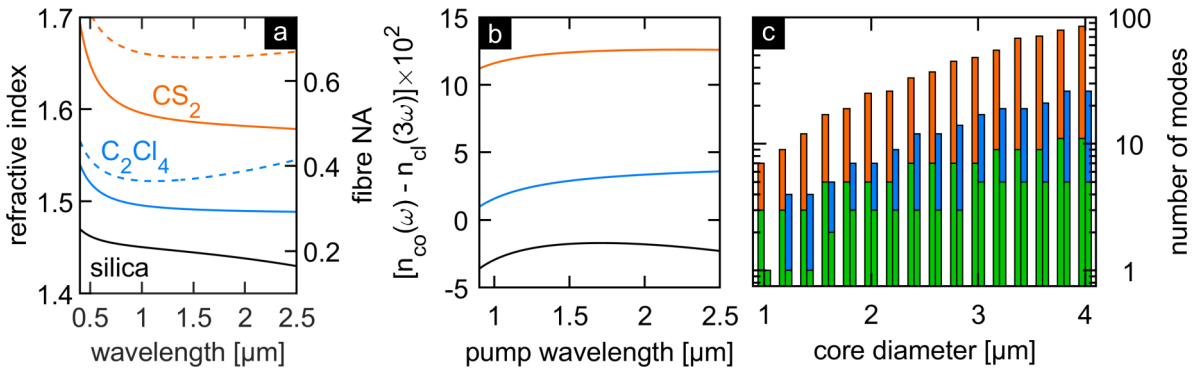
Fig. 31: Dispersion and fibre properties. (a, solid lines, left y axis) Refractive index of core (red: CS_2 [38], blue: C_2Cl_4 [39,118]) and cladding (black: silica [126]). (a, dashed lines, right y axis) Numerical aperture. (b) Index difference to cladding at the harmonic (colours as in (a)). (c) Number of non-degenerate guided modes for CS_2 (red) and C_2Cl_4 (blue) at 532 nm. The green portion highlights the number of modes with a central intensity lobe.

4.1.4 Phase Matching in a Liquid Filled Fibre

In simulations different linear dispersion regimes, as well as nonlinear contributions, were explored to determine their impact on the conversion process. Sufficient signal can

be generated if phase matching is achieved among the interacting modes. In this subsection the waveguide design is detailed for both liquids revealing the dispersion parameters that can be targeted.

Fig. 32 provides an overview of possible higher order modes that achieve phase matching to a fundamental pump mode at 1.56 μm using C_2Cl_4 (Fig. 32 (a)) or CS_2 (Fig. 32 (b)). As discussed in subsection 2.4.3, only modes with central intensity peaks (HE-type) are considered. Phase matching is indicated at the intersection of the HOM with the fundamental mode (HE_{11}) upon entering the green area. For C_2Cl_4 phase matching is achieved with a HE_{13} mode close to the single mode regime of the pump which is indicated by the grey shaded area, an HE_{14} mode can also be phase matched at higher V parameters and core sizes, respectively. CS_2 exhibits an enlarged green area within the V parameter range shown in Fig. 32 (b) compared to C_2Cl_4 due to the larger NA, yet the same two types of modes can be phase matched at smaller core sizes compared to C_2Cl_4.

To determine an optimal core size for an experiment, the phase matching points shown in Fig. 32 (a, b) are traced in the desired spectral range and yield unambiguous pairs of core size and wavelength. For this calculation the full material and waveguide dispersion is accounted for by solving the linear phase matching condition

$$0 = \Delta\beta_{\text{lin}} = \beta^H(3\omega) - 3\beta^P(\omega). \tag{40}$$

In this case no approximation is applied, $\beta(\omega)$ is found numerically for the modes of interest and Eq. (40) is solved subsequently. Nonlinear contributions, i.e. a power dependent shift from the phase matched wavelength λ_{PM}, are neglected since both $\partial_r\Delta\beta$ and $\partial_\lambda\Delta\beta$ are more than two orders of magnitude larger than $\Delta\beta_{\text{NL}}(P_{\text{max}})$ assuming a 30 kW peak power in either CS_2 or C_2Cl_4.

The resulting phase matching curves are shown in the bottom row of Fig. 32 (left axes) as solid lines for the modes HE_{13} in C_2Cl_4 (a), HE_{13} in CS_2 (b), and HE_{14} in CS_2 (c). The coloured part highlights normal (red, ND) and anomalous dispersion (blue, AD) for the fundamental pump mode. At the black dot the GVD of the pump is equal to zero. The dashed curves (right axes) show the group velocity mismatch (GVM) between pump and harmonic. Symbols highlight experimental observation (stars) which are discussed in the following subsections. Insets in Fig. 32 (c-e) show the Poynting vector distribution of the respective modes in colours of the experimental observation in a LCF with core

diameter 3.4 μm. From the bottom row it is evident that the condition GVM < 0 cannot be fulfilled in the shown range of wavelengths and core sizes. In fact, no modal combination, including pumping via transverse electric and transverse magnetic modes, was found to achieve phase matching and provide a negative GVM in C_2Cl_4 or CS_2 filled LCF to enable XPM based frequency down-shift in a THG experiment.
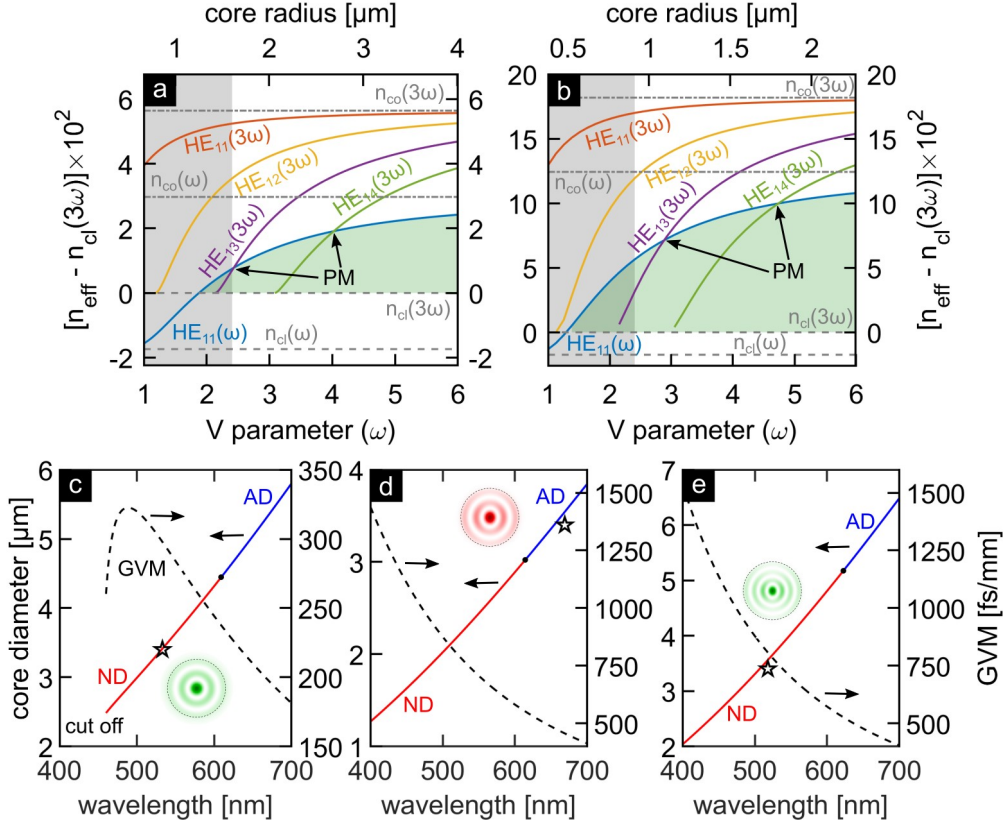
Fig. 32: Modal dispersion in liquid filled step index fibre referenced to cladding refractive index at the harmonic frequency. (a) C_2Cl_4, NA = 0.372 and (b) CS_2, NA = 0.655 for 1.56 μm pump wavelength. Horizontal lines indicate core and cladding indices, coloured curves represent modes according their label. PM indicates phase matching at the intersection of a higher order mode with the fundamental pump mode which occurs upon entering the green area. Grey area: single mode operation of pump. (c – e) Phase matching calculation for (c) HE_{13} mode in C_2Cl_4, (d) HE_{13} mode in CS_2, (e) HE_{14} mode in CS_2. Solid lines represent the required core diameter (left axis) vs. harmonic wavelength. The red (blue) part indicates normal (anomalous) dispersion at the pump wavelength. Dots highlight the zero dispersion wavelengths. Group velocity mismatch (dashes, right axis) is shown for each core-wavelength pair. Insets: modal intensity with core as dotted line. Stars: experiments with 3.4 μm core (c) 533 nm and 3.5 μm core (d) 669 nm, (e) 518 nm.

In general, larger cores lead to larger λ_{PM} because HOMs cut-off at fixed V parameters. The tuning slope, i.e. the change of THG wavelength versus core diameter, amounts to 7.7 % in (c), 10.3 % in (d), and 7.0 % in (e) evaluated at the experimental THG wavelengths indicated by stars. Axially varying core sizes, i.e. tapered fibres can hence be used to achieve a phase matched bandwidth beyond that of a fibre with constant core size provided sufficient pump bandwidth is supplied.

A similar approach was demonstrated using a standard silica telecommunication fibre tapered down with a linear slope in width [15], yet multiple modes were observed in that case rather than a single HOM with broadband emission.

4.2   Experimental setup

A representative experimental setup is shown in Fig. 33 (a) below. Commercial Er:doped fibre lasers are used as pump sources delivering pulses of different durations in order to investigate the impact of the molecular nonlinearity. Autocorrelation traces are shown in the inset exemplarily. The pulse energy is controlled via a combination of half wave plate and linear polarizer. Depending on the beam size and fibre core size a suitable aspheric lens is used to launch pulses into the fibre which is assembled manually in a home-made optofluidic mount[4]. The mount is fed with the fibre and serves as liquid reservoir and light coupling interface. Such a pair of mounts is then clamped in commercial holders using a 40 mm optical rail system. Fibres fill by capillary forces when submerged in the liquid without the need of external pressure.

The assembly is then positioned between coupling and collecting lenses which are mounted on three-axes-translation stages.
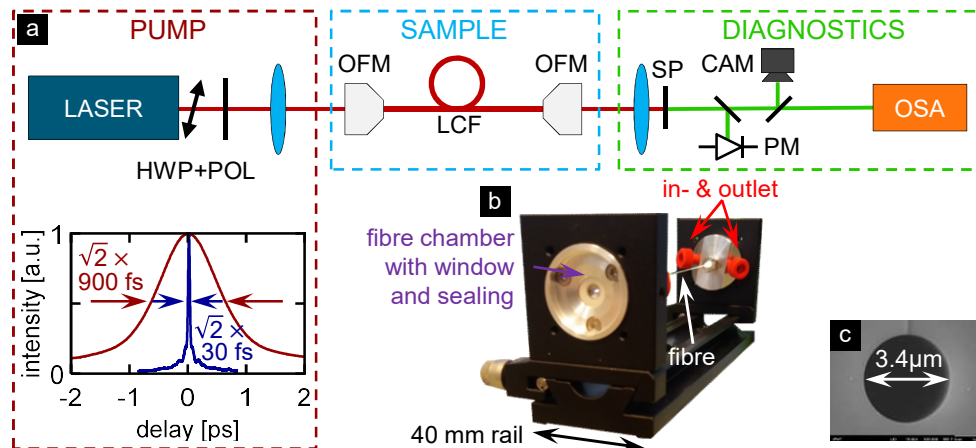
Fig. 33: (a) Experimental setup: Three different Er:doped fiber lasers are used as pumpsources (30 fs, 90 fs, and 900 fs FWHM pulse duration). Typical autocorrelation traces are shown for 30 fs and 900 fs. The diagnostics include an optical spectrum analyser (OSA) and beam profilers for visible and near infrared radiation (HWP: half-wave-plate, POL: polarizer, OFM: optofluidic mount, LCF: liquid filled fiber, SP: short pass filter, PM: power meter). (b) photograph of the mounted LCF. (c) SEM image of capillary. [After Ref [118], © OSA 2020].

---

[4] Initial designs of optofluidic mounts by Mario Chemnitz

Fibre coupling and transmission is monitored via input and output powers which are measured with a thermal power meter in case of the pump and the spatial beam profile is observed with a camera for near infrared radiation. The harmonic signal is monitored via a photo diode power meter and a camera sensitive in the visible range. Both harmonic and pump waves are collected using a fibre with core diameter of 200 μm and are analysed in the spectral domain by optical spectrum analysers (OSAs) that provide a noise floor of -80 dBm (10^{-8} mW). The power dependent evolution and signal strength can thus be recorded for small steps of launched pulse energy and yields the power spectral evolutions which will be presented in the respective subsections.

4.3 Third Harmonic Generation in Circular Liquid filled Step Index Fibres

C_2Cl_4 and CS_2 were identified to fulfil the criteria pointed out in section 4.1, that is high transmission for pump and harmonic, large molecular contribution, and ability to form LCFs with sufficient index contrast to allow phase matching. Hence these two liquids are deployed as core materials for the following experiments.

4.3.1 Third Harmonic Generation in C_2Cl_4 filled Fibres

In this subsection the experimental data for THG in TCE in circular fibres are presented and results were published in parts in ref. [118]. To investigate a possible effect of the non-instantaneous nonlinearity and to study the conversion dynamics in the sub-picosecond domain, three kinds of Er:doped fibre lasers delivering pulses with full width at half maximum of 30 fs, 90 fs, and 900 fs are used as pump sources. The central wavelength is in the telecom domain at 1.56 μm, such that THG is expected in the green part of the visible spectrum.

Due to different pulse durations, the non-instantaneous contribution to the nonlinearity (i.e. the molecular fraction f_R) amounts to 3 % for 30 fs, 17 % for 90 fs, and 71 % for 900 fs at the fibre input. This targets THG in a quasi-instantaneous (30 fs), weakly non-instantaneous (90 fs), and highly non-instantaneous (900 fs) regime. It is to emphasize again that f_R dynamically changes during propagation due to the interplay of dispersion and nonlinear frequency generation, yet it is common to present a static initial value as it is done for solid glass fibres.

4.3.1.1 Characteristic figures for THG in TCE-LCF

A core diameter of 3.4 μm is chosen to achieve intermodal phase matching between the fundamental pump mode and the HE_{13} higher order mode (HOM) targeting the harmonic wavelength of 532 nm (see Fig. 32 (c) star) which can be an important wavelength for future investigations of spontaneous parametric down conversion experiments in such LCFs. The hybrid mode represents the HOM of lowest order allowing for highest possible modal coupling due to its field distribution. The central intensity lobe contains approximately 22 % of the total energy that is guided in the mode. The LCF supports 4 (19) modes at 1596 nm (532 nm) wavelength and is normal dispersive in both cases with a group velocity dispersion (GVD) of 30 fs^2/mm and 296 fs^2/mm, respectively. The group velocity mismatch (GVM) is $\approx$299 fs/mm such that pulse walk-off is expected even for 900 fs pulses after the relatively short distance of 3 mm. It is to emphasise again that the above parameters are evaluated at the exactly phase matched wavelength according to the modal dispersion. In other words, these parameters are based on the LCF, not on the laser systems to be used. The initial bandwidth of the 30 fs laser covers the phase matched wavelength. Both laser systems providing 90 fs and 900 fs pulses are centred at 1.56 μm wavelength, whereas the bandwidth of the latter does not cover the phase matched wavelength. Table 4 therefore summarises important parameters that are evaluated for this LCF in view of the particular laser central wavelength of 1.56 μm.

As it is common, the phase mismatch is expanded around the laser central frequency ω_0 up to the first order as in section 2.4.1 which yields $\Delta\beta(\omega) \cong \Delta\beta_0 + \text{GVM} \cdot \Omega$. The phase mismatch $\Delta\beta_0$ amounts to 25 mm^{-1} which results in a coherence length of 124 μm for the THG wavelength of 520 nm. For the particular experimental configuration the detuning, $\Omega = 3(\omega - \omega_0)$, amounts to -12.4 THz which leads to a redshift of 11.2 nm. The numerical value where to expect THG (531.2 nm) agrees well with the direct calculation, showing the validity of the low order approximation in this case. The ZDW, i.e. the transition from ND to AD domain, is at 1.95 μm. As it is far away from the PM wavelength it is not considered further.

Table 4: Summary of fibre parameters according to the experimental configuration at the pump central wavelength of 1.56 µm. $L_c = \lambda_0/6\Delta n_{\text{eff}}$, $\Omega = 3(\omega - \omega_0) = -\Delta\beta_0/\text{GVM}$

dispersion parameters	GVM [fs/mm]	GVD [fs^2/mm]	TOD [fs^3/mm]	FOD [fs^4/mm]
520 nm	320	263	-320	2148
1560 nm		32	85	-215
phase matching	$\Delta\beta_0$ [mm^{-1}]	L_c [µm]	Ω [2πTHz]	$\delta\lambda_{\text{THG}}$ [nm]
	25.3	124	-12.4	11.2
modal coupling	J_{SPM} [µm^{-2}]	J_{XPM} [µm^{-2}]	J_{THG} [µm^{-2}]	
520 nm	0.202	0.096	0.0023	
1560 nm	0.097			
pulse parameters	L_{w} [mm]	L_{D} [mm]	f_{r} [1]	
30 fs	0.09	9	0.03	
90 fs	0.28	81	0.17	
900 fs	2.81	8146	0.71	

The coupling constant J_{THG} exceeds the one reported in ref. [17] by 200% using the same type of HOM. Yet the overlap for SPM of the pump, and XPM of the TH due to the pump, are approximately 40 times larger, which highlights their relative importance during propagation.

4.3.1.2 THG in TCE-LCF – Experimental Data

The power spectral evolutions for TH and pump wave are shown in Fig. 34 (top row: THG, bottom row: pump) after propagating a 15 cm long TCE-LCF. For each panel the experimental data is normalised to its respective maximum and plotted in dB-scale. Note here, the colour bar in (f) represents a 40 dB contrast which applies to the bottom row, whereas each panel in Fig. 34 uses a different colour scale and contrast for THG ((a) 30 dB, (b) 40 dB, and (c) 20 dB) due to different resolutions during acquisition and repetition rates of the laser systems (resolution: (a) 0.05 nm, (b) 0.2 nm, and (c) 0.05 nm; repetition rates: (a) 80 MHz (b) 40 MHz (c) 400 kHz). For top and bottom the axes show pump pulse energy (left) and pump peak power (right), which is calculated assuming a Gaussian pulse with the measured pulse energy. The initial molecular fraction is indicated in the bottom row using the model of [88]. Insets in top row show experimental farfield images of the HE$_{13}$ mode which prove intermodal phase matching to a HOM, rather than intramodal THG that would emerge in the fundamental mode. The diamond in Fig. 34 (f) highlights λ_{PM} for panel (c) at the onset of THG.
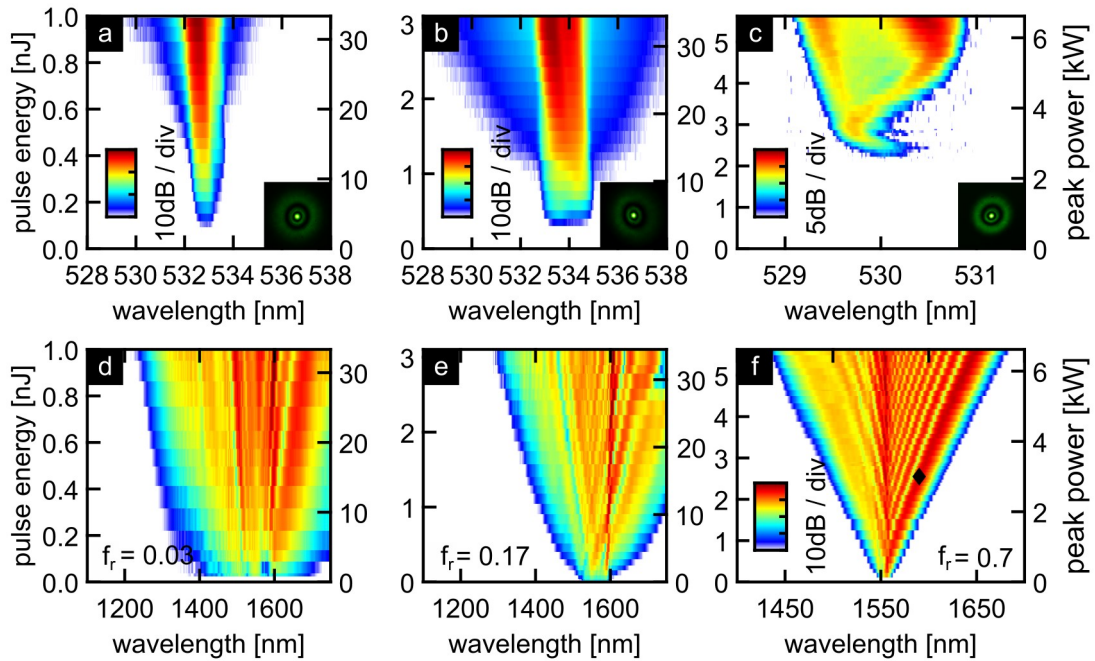
Fig. 34: Experimental power spectral evolution in a 15 cm TCE-LCF with core diameter 3.4 μm of TH (top row) and pump (bottom row) for pump pulse durations of 30 fs (a, d), 90 fs (b, e), and 900 fs (c, f) in log-scale. Left axes: pulse energy, Right axes: pulse peak power. Insets in top row show modes in farfield, initial molecular fractions are stated in bottom row. Colour scale in (f) applies to bottom row. Diamond in (f) highlights THG onset from (c). Reprinted from [118] © OSA (2020)

A common peak power threshold slightly below 3 kW is revealed by experiments, although it requires more pulse energy for longer pulses to generate measurable TH signal. Whereas the 30 fs and 90 fs pulses exhibit a bandwidth that covers λ_{PM} initially, for 900 fs pulses the bandwidth of the pump must be increased due to SPM. As soon as the pump spectrum reaches λ_{PM} TH is generated (see marker in Fig. 34 (f)). Remarkably, THG occurs almost immediately once the pump covers λ_{PM}, which first occurs towards the end of the fibre leaving little propagation length for conversion. With increasing power, SPM causes spectral broadening at shorter propagation distances, leaving a greater length of interaction for THG. These results clearly show that THG occurs at λ_{PM} if a seeding spectral component is present.

For the 90 fs pulses (Fig. 34 (b)) a narrow TH peak is observed followed by a growing spectral pedestal which is attributed to XPM between the harmonic signal and the spectral pump components generated by SPM. However, the level of the pedestal is 25 dB – 30 dB below the TH peak. Despite the lesser dynamic range in the other experiments (Fig. 34 (a,c)), for 30 fs pulses the pedestal is still visible. The wavelength at which the TH peaks shifts by 2 nm – 3 nm from experiment to experiment. Small variations of the core diameter along the capillary spool from which the samples are

taken can cause such shifts. λ_{PM} shifts by 7% of the core size deviation in Fig. 32 (a). Since the spatial resolution of the SEM imaging is also limited to approximately 50 nm – 60 nm, this can amount to a shift of 3.5 nm – 4.2 nm for λ_{PM}.

In Fig. 34 (d,e,f) the spectral evolution of the pumps are shown. SPM driven broadening is observed in the normal dispersive regime and is particularly clean, but asymmetric in case of the 900 fs pulses (Fig. 34 (f)). The evolution will be discussed in subchapter 4.3.1.4 in more detail.

4.3.1.3 Analysis of Experimental Data in TCE-LCF

The spectra of the harmonic develop a spectral FWHM of 0.6 nm for 30 fs and 1.4 nm for 90 fs pump pulses. This bandwidth is two orders of magnitude larger than predicted by first order dispersion theory, $\Delta\lambda_{THG} = 0.441 \cdot \lambda_{THG}^2 / (c_0 \cdot L_{LCF} \cdot GVM)$, resulting in $\Delta\lambda_{THG} \approx 9$ pm for a 15 cm long LCF as in the experiments. Note that neither of the aforementioned bandwidths is limited due to the resolution of the OSA, which allows retrieving it and the respective peak centre from the data. In Fig. 35 the TH peaks are shown versus pump pulse energy and exhibit a blue-shift for increasing energy and pump peak power for 30 fs and 90 fs pulses in Fig. 35 (a) and (b). The green shaded area represents the spectral FWHM which follows the same trend. In case of 900 fs pulses, the complicated splitting dynamics shown in Fig. 34 (c) are captured in Fig. 35 (c), to this end the peaks are extracted above and below 529.7 nm and are evaluated separately. The limit of 529.7 nm is arbitrary, yet it represents a reasonable choice in accordance with the data shown in Fig. 34 (c).

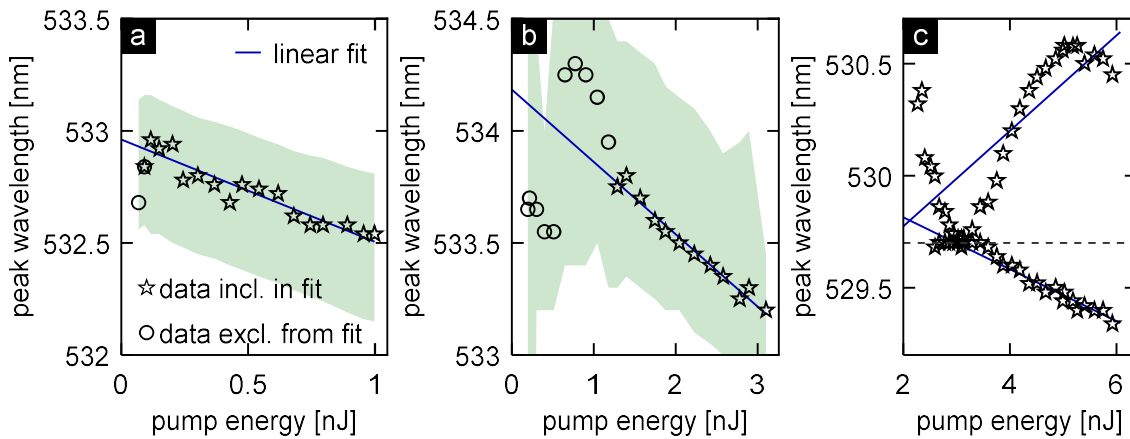Fig. 35: Experimental power dependence of TH peak wavelength for (a) 30 fs, (b) 90 fs, and (c) 900 fs. Legend in (a) applies to all panels. The shaded area in (a) and (b) represent the spectral FWHM, which is omitted in (c) for clarity. Due to the more complex dynamical behaviour for 900 fs pulses, in (c) the peaks are extracted above and below 529.7 nm (indicated by the dashed horizontal line). For details see main text.

For linear fits data points with low signal were excluded, and in case of Fig. 35 (b) the initial swings of the peaks were excluded as well, yet the general trend is not affected if all data is included for a fit. The rates $R_{\delta\lambda}^{E}$ at which the TH peaks shift versus pulse energy are $-456\,\text{pm/nJ}$ (a), $-322\,\text{pm/nJ}$ (b), $-116\,\text{pm/nJ}$ below $529.7\,\text{nm}$, and $213\,\text{pm/nJ}$ above $529.7\,\text{nm}$ (c), respectively. Note however, a blue-shift may be continued even above the $529.7\,\text{nm}$ case in (c) if greater pulse energies are launched than it was possible in experiments due to the damage threshold of the LCF samples. The findings suggest a stronger shift for shorter pulses, however if the fits are conducted versus peak power, the situation is reversed. The rate can be obtained via $R_{\delta\lambda}^{P_0} = \tau \times R_{\delta\lambda}^{E}$, with the pulse duration τ and leads to $-14\,\text{pm/kW}$ (30 fs), $-29\,\text{pm/kW}$ (90 fs), $-104\,\text{pm/kW}$, and $191\,\text{pm/kW}$ (900 fs, below and above $529.7\,\text{nm}$) in agreement with simulations from section 3.3.3.3.

As established before, the detuning due to peak power, $\partial\Omega/\partial P = -3\gamma/\text{GVM}$, which is expected to lead to a red-shift for the present dispersion $(\text{GVM} > 0)$ [127], is overcompensated by XPM. In solid glass microstructured fibres $\text{GVM} < 0$ is the more common case [9,127,128] and blue-shifts of the TH with increasing power were observed when the fibre was pumped close to the maximum group index in the AD regime. Hence the experimental observation indicates the potential impact of the non-instantaneous response. Further, it is to note that a red-shift in silica based fibres may originate from both positive GVM and soliton self-frequency-shift due to the ultrafast Raman response in glasses.

4.3.1.4 Pump Evolution in the Non-Instantaneous Regime

Revealing the effect of the retarded response during propagation is challenging, the data shown in Fig. 34 (f) on p.61 allow investigating the bandwidth evolution for a large f_{R} that may be used to determine both the effective nonlinearity of the fibre as well as the effect of the material response. Fig. 36 presents cut-off wavelengths extracted from individually normalised experimental data. An experimentally relevant cut-off at the $-30\,\text{dB}$ ($\lambda_{\text{-30dB}}$, circles) and at the $1/e$ level ($\lambda_{1/e}$, squares, corresponds to $-4.34\,\text{dB}$), which is common in theoretical considerations, are chosen. Red (blue) colour represents longer (shorter) wavelength cut-offs with respect to λ_0. Black diamonds indicate the centre of mass wavelength (λ_{COM}). Whereas on the red spectral edge both cut-offs run in parallel for increasing power, a significant difference for the evolution of the cut-offs is

observed on the blue spectral wing, indicating a general shift of spectral power towards longer wavelengths. This effect is reminiscent of a soliton self frequency shift in the AD domain, yet in this case the soliton maintains its spectral shape [109,110,129]. Here, typical SPM structure above and a rather flat spectral extension below λ_0 is observed, similarly as in [33] but with larger NLP shifts. The evolution of λ_{COM} shows a linear red-shift at a rate of (5.8 ± 0.1) nm/kW.
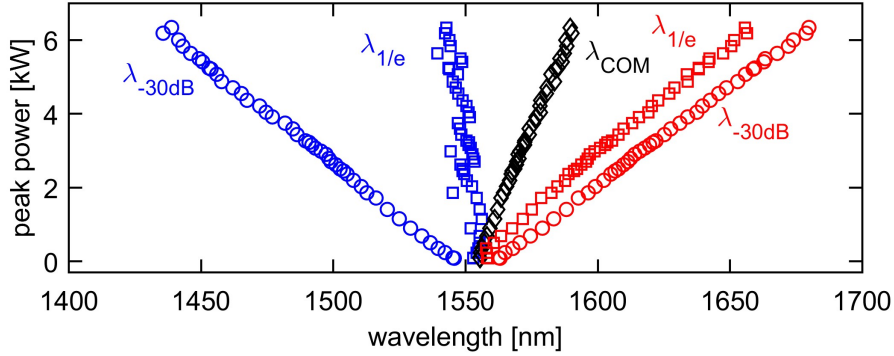
Fig. 36: Experimental evolution of bandwidth for 900 fs pulses in a C₂Cl₄ LCF with 3.4 µm diameter. Data is extracted from Fig. 34 (f). Black diamonds represent spectral centre of mass (λ_{COM}), The -30 dB and 1/e cut-off for the short (blue) and long wavelength region (red) are shown as circles and squares, respectively.

For 900 fs pulses the characteristic length scales of dispersion are much larger than the sample length (Table 4, p. 60, $L_D > 8$ m), the attempt to extract an effectively acting nonlinearity, γ_{eff}, directly from the bandwidth is reasonable. Since the relevant broadening mechanism is SPM and dispersive broadening is negligible, the standard estimate $\delta\omega_{max} = \delta\lambda_{max} \cdot 2\pi c_0/\lambda_0^2 = 0.86 \cdot \gamma_{eff}P_0L \cdot T_0^{-1}$ (see, e.g. [85]), where L is length (15 cm), T_0 is the 1/e half width (540 fs), and P_0 is peak power, connects bandwidth and NLP resulting from the fibre and pulse parameters during propagation. The slope of a linear fit yields $\delta\lambda_{max}/\delta P_0$ and when solved for γ_{eff} while accounting for the red-shift in λ_0, one obtains $\gamma_{eff}^{red} = (34 \pm 1)$ (m kW)$^{-1}$ and $\gamma_{eff}^{blue} = (24.2 \pm 0.5)$ (m kW)$^{-1}$, respectively. Note these values represent an *effective* nonlinearity, i.e. the nonlinearity necessary to achieve the measured bandwidth regardless of the physical mechanism. It is worth noting that $\gamma_{el} < \gamma_{eff} < \gamma_{total}$ holds for either of the two values retrieved from experiment and calculated values using the model from [39] or [88], respectively. This means the retarded response not fully contributes to SPM.

4.3.1.5 Experimental Efficiency of THG in C_2Cl_4 fibre

To evaluate the efficiency of the THG process, direct average output power of the harmonic is measured for increasing average pump powers. Average powers are converted to energy via the laser repetition rates and the data is shown as symbols in Fig. 37 (a) and (b) versus peak power and pump pulse energy, respectively. Solid lines show cubic polynomial fits ($s \cdot X^3$) with good agreement to the data as expected for THG. Here, s is the slope efficiency and X is either peak power or pulse energy of the pump. Scaling the y-axis by 10^{-6} allows direct determination of the experimental conversion efficiency η^{exp} by reading off the respective value from the axis (Fig. 37 (b)).

Important parameters are given in Table 5, including the experimental maximum conversion efficiency $\eta_{\text{max}}^{\text{exp}} = P_H/P_P$ for the highest average powers of pump and harmonic. Note that η^{exp} is obtained from the slope efficiency s_E by rescaling with f_{rep}^{-2} (f_{rep}: repetition rate).
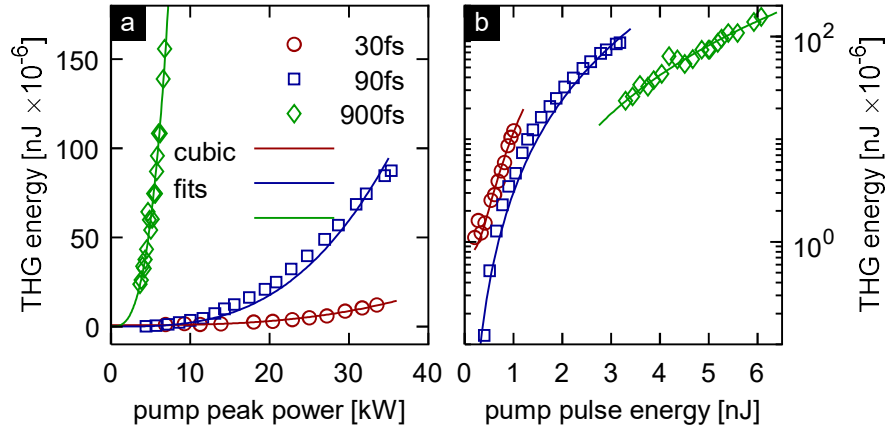
Fig. 37: Output energy of harmonic signal for increasing pump peak power (a) and pulse energy (b) for 30 fs (red circles), 90 fs (blue squares), and 900 fs (green diamonds) pulse duration (FWHM) in C_2Cl_4 LCF. Solid lines represent cubic fits as described in the main text. Upper y-axis limits in (a) and (b) are identical. Reprinted from [118] © OSA (2020).

In these experiments it was shown that the slope efficiency with respect to peak power continuously increased with pulse duration, whereas a decrease is found when s is evaluated with respect to pulse energy. Both results are consistent – yet, the highest conversion efficiency was similar for 90 fs and 900 fs pulses, which both were limited by the damage threshold of the sample. The damage mechanism in LCFs is largely unexplored and beyond the scope of this thesis. However, long term studies showed excellent stability for high average power beam delivery and continuum generation [130] when pumping at 1.9 μm which will be discussed in section 4.6, and capabilities to

deliver highly energetic 3 μm pulses in the ns-regime were already demonstrated [131,132] . In case of 30 fs pulses the delivered pulse energies were insufficient to damage the LCF.

Table 5: Slope efficiency s, experimental efficiency η, and number of photons per pulse for THG with different pulse durations in C_2Cl_4 LCF.

pump FWHM [fs]	s_{P_0} [fJ/kW^3]	s_E [fJ/nJ^3]	η_{max}^{exp} [1]	photons / pulse ($\lambda = 532$ nm)
30	2.9×10^{-4}	10.9	1.2×10^{-5}	30×10^3
90	2.2×10^{-3}	3.0	2.7×10^{-5}	216×10^3
900	0.478	0.7	2.6×10^{-5}	385×10^3

4.3.2 Third Harmonic Generation in CS₂ filled Fibres

Experimental results for CDS-LCFs are presented in this subsection focussing on the two spectrally separated phase matched modes shown in panels (d) and (e) in Fig. 32 on page 56. Due to the higher refractive index compared to C_2Cl_4 two modes, namely the HE_{13} and HE_{14} modes, can be addressed with the 30 fs and 90 fs laser systems. For 900 fs pulses no stable THG output could be generated and detected due to the lower coupling constant of the HE_{14} mode at 520 nm and the lack of pump signal for the HE_{13} mode at 650 nm. Further, CS_2 exhibited a slightly lower damage threshold than C_2Cl_4.

Due to its strong retarded response, the initial f_R amounts to 9 % for 30 fs and 42 % for 90 fs pulses in a CS_2 LCF representing more than twice as much contribution due to the molecular response as for C_2Cl_4.

4.3.2.1 Characteristic figures for THG in CDS-LCF

Similar to the case of TCE, a round 3.5 μm core size is used to achieve phase matching in the visible domain. Here, different pump dispersion regimes, i.e. the ND and AD regimes, are targeted to observe a possible impact from GVD and potential soliton formation in the AD regime compared to a dispersive wave pump in the ND regime.

For the case of phase matching to the HE_{14} mode the CDS-LCF supports 7 (72) modes at 1554 nm (518 nm) wavelength and is normal dispersive in both cases with a GVD of 38 fs^2/mm and 348 fs^2/mm, respectively. The GVM is ≈813 fs/mm, i.e. the slope of $\Delta\beta$ is much steeper than in case of TCE which ought to limit the THG bandwidth. The CDS-LCF in the HE_{13} mode configuration supports 4 (37) modes at 2007 nm (669 nm) wavelength but this time is anomalous dispersive for the HE_{11} mode (ZDW is 1.79 μm)

with a GVD of -35 fs^2/mm and normal dispersive at the harmonic (204 fs^2/mm). The GVM amounts to 459 fs/mm. Again the above parameters are evaluated at λ_{PM} according to the modal dispersion without approximations as in case of TCE. Similar to the former section, a central laser wavelength of 1.56 µm is chosen to present dispersive parameters in Table 6 as well as characteristic lengths and the detuning.

Since λ_{PM} for the HE$_{13}$ mode in this case is far from the pump central wavelength, the linear expansion of $\Delta\beta$ is not valid anymore, therefore a fictitious pump central wavelength of 1.95 µm, e.g. a Tm-doped laser source, is assumed as reference as if the HE$_{13}$ mode was pumped by a separate pulse. This assumption may seem arbitrary at first but is motivated by the spectral evolution shown in the following chapter. Hence all parameters in Table 6 are given twice corresponding to the wavelength pairs of 520 nm and 1560 nm for the HE$_{14}$ mode and 650 nm and 1950 nm for the HE$_{13}$ mode which are pumped from the fundamental HE$_{11}$ mode in either case.

Table 6: Summary of fibre parameters according to the experimental configuration at the pump central wavelength of 1.56 µm for a conversion to the HE$_{14}$ mode given by the first value in each cell. The second value corresponds to the HE$_{13}$ mode pumped at 1950 nm. $L_c = \lambda_0/6\Delta n_{eff}$, $\Omega = 3(\omega - \omega_0) = -\Delta\beta_0/\text{GVM}$

dispersion parameters	GVM [fs/mm]	GVD [fs^2/mm]	TOD [fs^3/mm]	FOD [fs^4/mm]
HE$_{14}$ / HE$_{13}$	809 / 477	345 / 218	227 / 182	249 / 193
HE$_{11}$		37 / -26	214 / 334	-266 / -902
phase matching	$\Delta\beta_0$ [mm^{-1}]	L_c [µm]	Ω [2πTHz]	$\delta\lambda_{THG}$ [nm]
	-36 / 30	87 / 105	7.12 / -9.93	-6.4 / 14
modal coupling	J_{SPM} [µm^{-2}]	J_{XPM} [µm^{-2}]	J_{THG} [µm^{-2}]	
HE$_{14}$ / HE$_{13}$	0.28 / 0.25	0.135 / 0.125	0.0006 / 0.0018	
HE$_{11}$	0.144 / 0.128			
pulse parameters	L_w [mm]	L_D [mm]	f_R [1]	
30 fs	0.04 / 0.06	8 / 12.6	0.09	
90 fs	0.11 / 0.19	78 / 113	0.42	
900 fs	1.11 / 1.9	7,822 / 11,311	0.89	

The detuning due to the choice of expansion wavelengths matches the experimental observation. Due to the different types of modes, the coupling constants J_{THG} differ by a factor of three which results in an approximate order of magnitude difference in generation efficiency if all other conditions were kept constant highlighting the importance of phase matching to the lowest order HOM possible.

4.3.2.2 THG in CDS-LCF – Experimental Data

During the course of experiments it was necessary to assemble several LCF samples since the damage threshold, in contrast to TCE-LCFs, varied noticeably from sample to sample. A higher degree of moisture, i.e. water absorption in the solvent, may have caused larger optical absorption which, however, was not evident in the recorded spectra. As a consequence the spectra shown below extend to the respective damage threshold of the LCF in use rather than to a common maximum power throughout all pump and harmonic recordings.

The power spectral evolution in case of 30 fs pump pulses is shown in Fig. 38 for the pump (a), the HE_{14} mode (b), and the HE_{13} mode (c). The ZDW is indicated as a dashed line in (a), at first the entire spectral power resides in the ND regime and SPM of the initial spectrum causes broadening towards the ZDW more rapidly as in the opposite direction. This is similar to the cases shown in Fig. 34, albeit the detection bandwidth this time is sufficient to capture the most red-shifted spectral components for the short pump pulse durations. At a level of 5 kW peak power the arrow indicates a sudden radiation transition from ≈ 1780 nm towards 2 µm with subsequent red-shift. Remarkably, for 90 fs pulses the same effect occurs at 5 kW peak power (see arrow in Fig. 39 (a)). This transition is essential as it provides the pump radiation for the HE_{13} mode and is well explained by a *four wave mixing* (FWM) approach. 1780 nm radiation serves as degenerate pump, strong initial pump light at 1.6 µm acts as signal and generates an idler at 2 µm which is confirmed by a phase matching condition of the respective propagation constants, i.e. $2\beta(1.78\mu m) = \beta(1.6\mu m) + \beta(2\mu m)$.
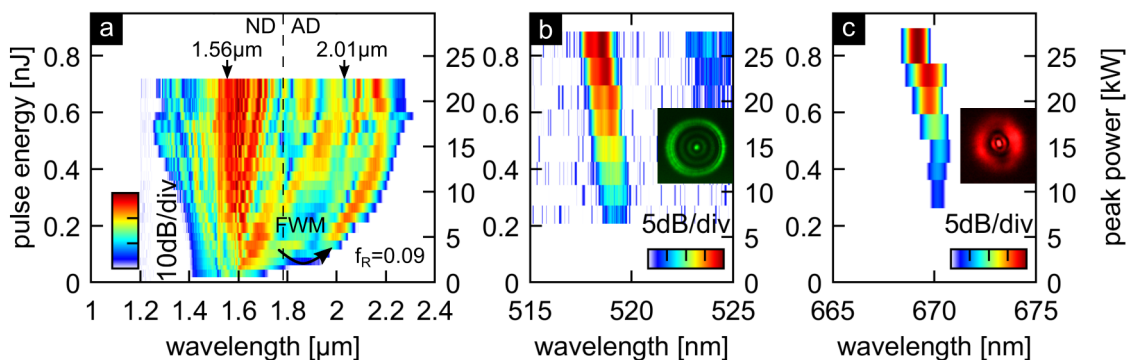
Fig. 38: Power spectral evolution in log-scale in a CS_2 filled LCF for 30 fs pump pulses (a) and THG in mode HE_{14} (b) and mode HE_{13} (c). The dashed line in (a) highlights the ZDW. Arrows at the top mark the central TH wavelengths from (b) and (c), a transition of radiation towards λ_{PM} is indicated. Insets in (b) and (c) are mode images captured simultaneously after the fibre. Common upper axes levels are chosen for comparability - data in (a) is cropped due to sample damage at 0.72 nJ. The fibre length was 15 cm.

Both HOMs in panels (b) and (c) exhibit an onset power threshold of approximately 7 kW, despite the initial coverage of the pump spectrum in case of the HE_{14} mode. As stated above the modal coupling coefficient is three times smaller and hence the overall conversion is less efficient in this case. Both modes exhibit a blue-shift with power despite their positive GVM with respect to the pump.

In case of 90 fs pump pulse duration the spectral dynamics of the pump show equivalent features in Fig. 39 (a), especially the FWM transition occurs also at 5 kW and the harmonic was detectable from approximately 7 kW onwards. A substantial extend towards short wavelengths in contrast to the 30 fs pulses is observed for similar powers, yet higher launched pulse energies. Note the dark patch in the 20 kW domain at 2.4 µm signals a grating artefact from 2nd order diffraction, i.e. spectral components with $\lambda < 1.2$ µm. In each case absorption in CS_2 limited broadening beyond 2.2 µm (see Fig. 28 (b) p. 50). As in all previous experiments, the harmonic tends towards shorter wavelengths for increased powers but in this case exhibits more spectral structure whose origin is difficult to determine. Qualitatively the same dynamics were observed for different samples with similar shifts and spectral structure.
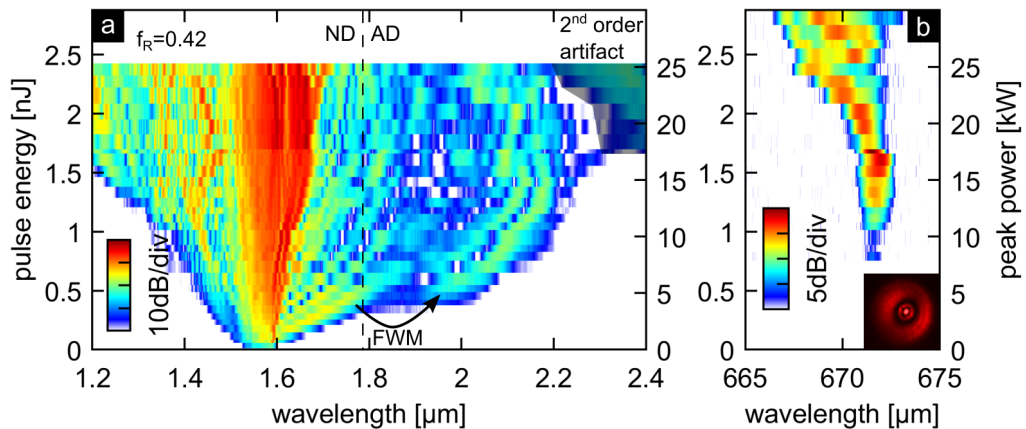
Fig. 39: Power spectral evolution in log-scale in a CS_2 filled LCF for 90 fs pump pulses (a) and THG in mode HE_{13} (b). The experimental mode is shown as inset. The dashed in (a) highlights the ZDW. The shaded batch is a higher order reflection artefact from radiation with $\lambda < 1.2$ µm inside the OSA. A sudden radiation transition at the ZDW towards λ_{PM} is marked in (a).

It is to note here that the HE_{14} mode was observed on a camera screen at relatively low intensity as the entire coupling conditions were optimised in favour of the HE_{13} mode for all samples.

4.3.2.3 Analysis of Experimental Data in CDS-LCF

The spectral FWHM of the harmonic in the CDS-LCF amounts to 1.06 nm for the HE_{14} mode at 519 nm (30 fs pulses), 0.74 nm (30 fs pulses), and 0.95 nm (90 fs pulses) for the HE_{13} mode. In case of 30 fs pulses the FWHM was averaged, whereas the median is reported for the 90 fs case due to the extent of structural fluctuation in the spectrum.

As in the case of TCE, the theoretical bandwidth predicted by first order dispersion theory, $\Delta\lambda_{THG} = 0.441 \cdot \lambda_{THG}^2/(c_0 \cdot L_{LCF} \cdot GVM)$, is surpassed by two orders of magnitude as the calculation yields $\Delta\lambda_{THG} \approx 9$ pm for HE_{13} and a width of 3 pm for the HE_{14} mode in a 15 cm long LCF. Further the overall trend of the blue-shift is shown in Fig. 40 (a-c). Peak TH wavelengths are extracted from the data and the FWHM is indicated by shaded areas. A solid line represents a linear fit and yields the rates $R_{\delta\lambda}^E$ at which the peak wavelengths shift. For 30 fs the blue shift amounts to -1409 pm/nJ (a), -1834 pm/nJ (b), or – 42 pm/kW and -165 pm/kW, respectively. The shift rates are larger by a factor of three to four compared to the case in TCE. The enhancement is due to the stronger relative contribution of molecular effects to the total nonlinearity.
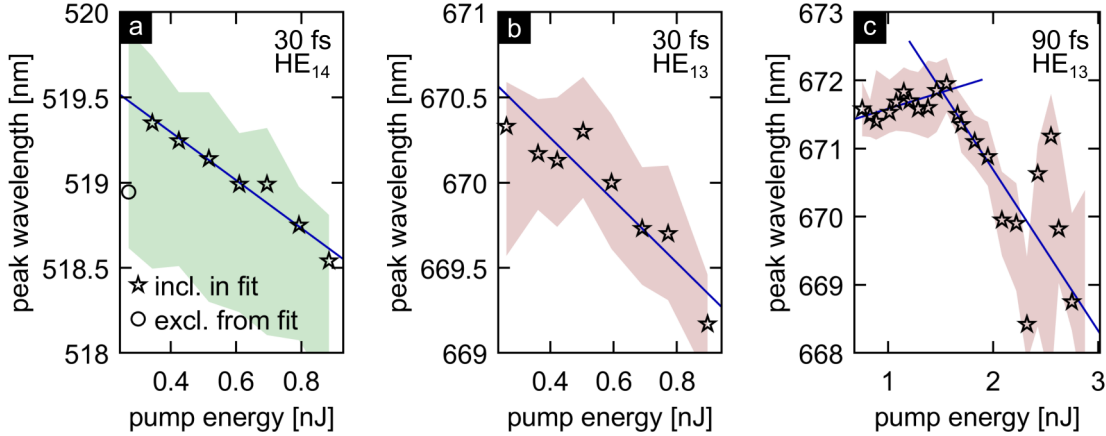
Fig. 40: Spectral shift in CDS-LCF extracted from experimental data. Pulse durations and mode labels are given in the panels. Shaded area corresponds to the FWHM. Solid lines represent linear fits highlighting the overall blue-shift with increasing pump energy. In (c) a modest red-shift is observed before a relatively steep blue-shift.

When pumped with 90 fs pulses $R_{\delta\lambda}^E$ is +475 pm/nJ initially but changes sharply at 1.7 nJ (≈ 17 kW) to -2361 pm/nJ (-212 pm/kW) in Fig. 40 (c) which maintains the overall trend of the blue-shift. Similar rates are obtained throughout different CDS-LCF samples, yet different samples from the same fibre spool showed quantitatively different spectral modulations since the THG process is sensitive to the launching conditions, i.e. modal coupling at input and pulse parameters, e.g. power and chirp.

4.3.2.4 Pump evolution in the non-instantaneous regime

Analogous to the case of a C_2Cl_4 filled LCF the evolution of bandwidths ($1/e$ and -30 dB) is investigated based on experimental data and is shown in Fig. 41. For 30 fs (a) and 90 fs (b) spectral broadening is limited due to absorption in CS_2 at 2.2 μm and it is to note that strong uncompensated chromatic aberration from coupling optics after the LCF alters spectral amplitudes which impacts retrieved bandwidths already at around 5 kW but especially beyond 10 kW. Albeit present in the case of 900 fs pulses, chromatic effects are less detrimental due to the smaller bandwidths. The -30 dB width (circles) highlights the generation of 2 μm radiation via FWM in (b), whereas in (a) the $1/e$ width (squares) jumps at the respective peak power as a consequence of different relative spectral amplitudes. Besides this jump, the $\lambda_{1/e}$ bandwidths remain in the spectral centre in (a) and (b) which is in contrast to the case of 900 fs (d). Here, broadening is also more symmetric towards blue and red spectral edges than in case of C_2Cl_4 shown in Fig. 36. The data shown in (d) is extracted from the spectral evolution in (c).

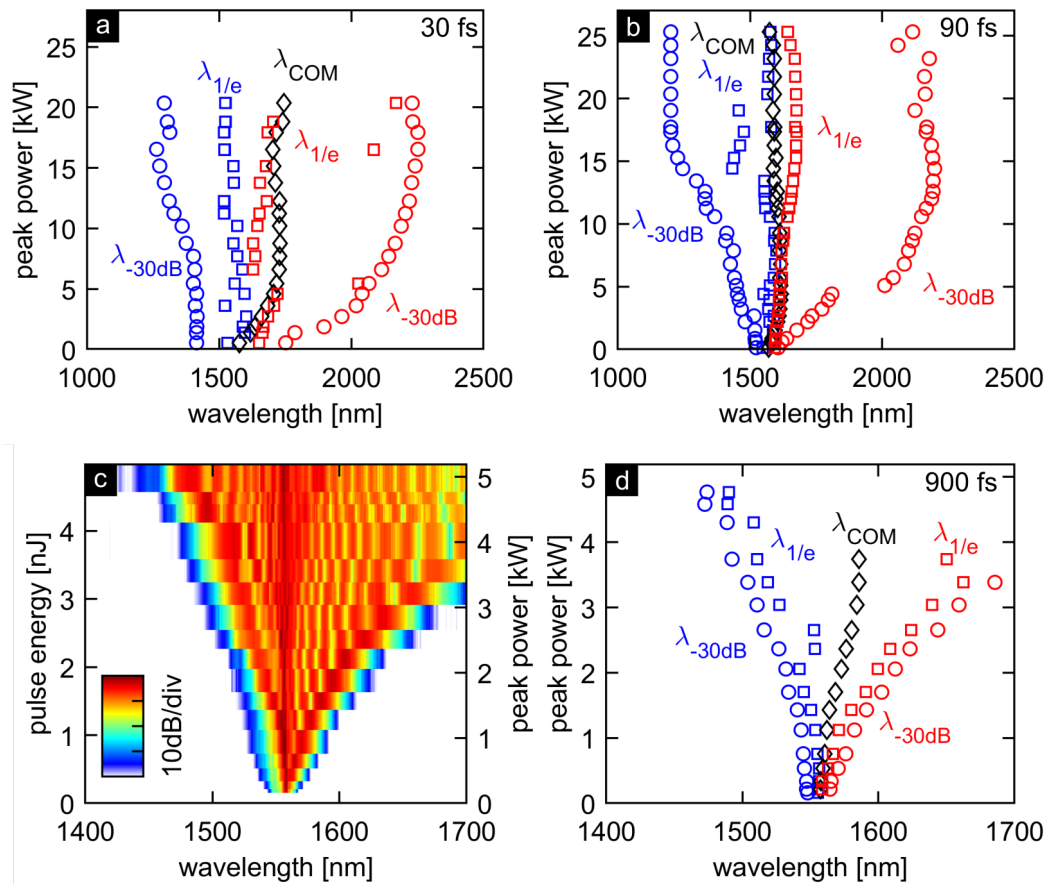Fig. 41: Bandwidth evolution for 30 fs (a), 90 fs (b), and 900 fs (d). Data for (d) was extracted from power spectral evolution for 900 fs in (c). Different bandwidths are indicated by dots (-30 dB) and squares (1/e) for longest (red) and shortest (blue) wavelength. The centre of mass (COM) wavelength is shown as black diamonds.

Note λ_{COM} was not determined beyond 3.5 kW due to insufficient detection bandwidth where only the blue spectral edges are retrieved. For each pulse duration an initial red-shift can be observed. Since dispersive length scales are much greater than the fibre length only for 900 fs pulses, the red-shift of (9.2 ± 0.5) nm/kW in this case can be attributed to the retarded response.

The procedure to extract an effective nonlinearity as described in section 4.3.1.4 using both the red and blue $\lambda_{1/e}$ leads in this case to $\gamma_{\text{eff}}^{\text{red}} = (50 \pm 1)$ (m kW)$^{-1}$ and $\gamma_{\text{eff}}^{\text{blue}} = (48.5 \pm 1)$ (m kW)$^{-1}$, respectively. As in the former case, the red-shift was accounted for, but here both parameters are very similar as the symmetrical broadening suggested. Experimentally obtained values are smaller than the purely electronic nonlinear parameter $\gamma_{\text{el}} = 89$ (m kW)$^{-1}$ calculated for a 3.5 µm core CDS-LCF. Considering the error margin of $n_{2,\text{el}}$ stated in [87] (27 %) and an overestimated peak power the experimental and theoretical values are in close proximity, however, no contribution to SPM from the retarded response would be present in that case despite the relatively long pulse duration harnessing a large amount of the retarded response.

4.3.2.5 Experimental efficiency of THG in CS$_2$ fibre

The procedure to obtain the conversion efficiency for the case of CS$_2$ filled LCF is analogous to that described in section 4.3.1.5, despite the THG signal used here is retrieved from the optical spectrum analysers (OSA) due to the lack of optimised short and long pass filters. Measured power spectral density is converted to signal energy using the laser repetition rate. Pump parameters are measured directly.

In Fig. 42 the increase in THG energy is presented versus pump peak power (a) and pump pulse energy (b) for the different modes and pump pulse durations, respectively. Solid lines represent cubic fits of the form $s \cdot X^3$ with slope efficiency s and X is either peak power or pulse energy. Cubic fits show reasonable agreement with the data as expected for a THG process. It is to note that the 90 fs case exhibits large fluctuation due to the spectral dynamics evident in Fig. 39 (b).

The respective efficiencies are provided in Table 7. Although the experimental efficiency is fairly low – mainly due to overall lesser power handling capabilities compared to C$_2$Cl$_4$ – the slope efficiencies exceed the ones obtained for C$_2$Cl$_4$ filled fibres by more than two orders of magnitude.
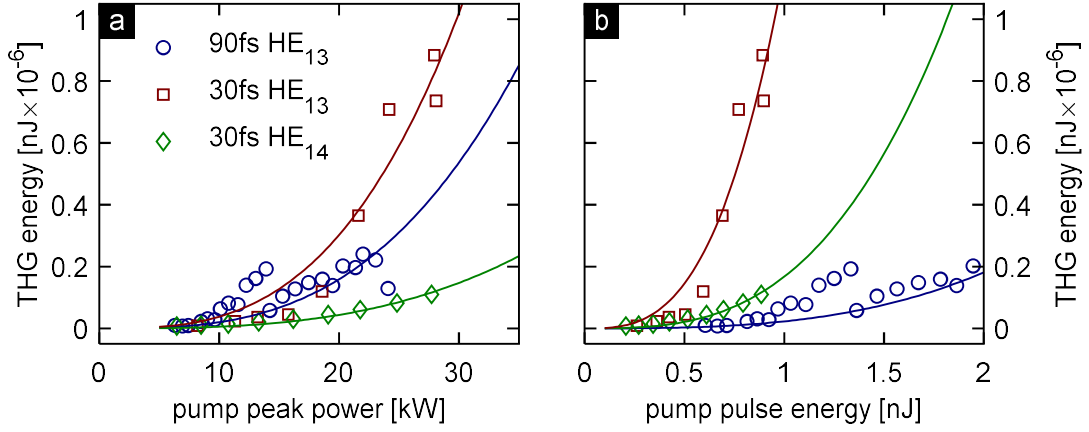
Fig. 42: Experimental THG output in a CS₂ filled LCF pumped by 30 fs (squares, red and diamonds, green) and 90 fs pulses (circles, blue) for increasing peak power (a) and pulse energy (b). Solid lines represent cubic fits to the data. Slope efficiencies are given in Table 7.

Table 7: Slope efficiency s and experimental efficiency η for THG with different pulse durations in CS₂ LCF.

pump FWHM [fs]	s_{P_0} [fJ/kW³]	s_E [fJ/nJ³]	η_{max}^{exp} [1]	mode
30	5.4×10^{-3}	167.3	1.2×10^{-7}	HE₁₄
30	378×10^{-3}	1160	9.9×10^{-7}	HE₁₃
90	199×10^{-3}	22.6	1.4×10^{-7}	HE₁₃

Clearly, THG in the HE₁₃ mode performed better than in case of the HE₁₄, as reasoned earlier due to its smaller modal coupling constant. Although the presented data do not admit conclusions which impact the pulse duration may have, these results suggest further capability of efficiency enhancement accounting for the large mismatch of power spectral density and phase matched bandwidth due to the pump pulse spectrum which occurred for both TCE and CDS-LCFs. Usually less than 5 % of the spectral power density is located within the phase matched bandwidth which in each case was experimentally determined to be of the order of 1 nm. Therefore transform limited pump pulses in the 2 μm domain with 2 ps FWHM duration and above seem ideal to greatly enhance the conversion efficiency in case of the HE₁₃ mode in a CDS-LCF, and similarly for TCE-LCFs at the respective wavelength.

4.4   Birefringence in Liquid Core Fibres

This chapter is devoted to explore in detail the possibilities to incorporate birefringence in LCF and to study its effects with the focus on THG and the participating HOMs in this process by both numerical methods and experiments. Results were published partially in [133]. Up to this point the pump was assumed to propagate in a single fibre mode, yet not necessarily in the single mode regime, discarding effects related to the polarisation of the input field and the existence of degenerate modes. It is the latter that may cause severe fluctuations during nonlinear wave propagation for instance during SCG as discussed in [134]. Both coherence and polarisation properties deteriorate due to vector or polarisation modulation instability (MI). Although MI is a noise seeded FWM process which occurs for large soliton numbers in the AD domain, recent studies showed that these effects are limiting performance in the ND domain as well [135,136] calling for an approach circumventing crosstalk among modes. Mitigation of polarisation related instabilities can be achieved by breaking the fibres symmetry, i.e. introducing mechanical stress or a noncircular geometry. The latter method is chosen here as it is straight forward to incorporate whereas inducing stress in the cladding of an LCF does not promise noticeable effects since liquid phase core materials intrinsically are free of any stress. The resulting IOR profile then exhibits at least two distinct axes a propagating mode may be polarised along with – the fast and slow axis. It will be shown that these are unrelated to the fibre geometry by its own which is in contrast to common sense. Further, the transformation of modes as discussed in the following sections reveals a number of advantages in THG due to enhancement of modal coupling.

4.4.1   Transformation of Modes in Elliptical Liquid Core Fibres

Guided modes in fibres strongly depend on the IOR distribution which is investigated here by means of fully vectorial finite element calculations covering a large range of ellipticity and wavelength using the commercial software COMSOL Multiphysics™ rather than semi-analytical methods [137] due to the large contrast of core and cladding IOR in elliptical LCF (eLCF).

A schematic of the fibre geometry is illustrated in Fig. 43 (a) to introduce the ellipticity Δ, i.e. the difference between semi major and semi minor axis of the ellipse. The semi major axis is denoted with ρ and is kept constant at 1.6 μm in the following analysis to allow for potential phase matching at smaller wavelengths than in previous

experiments. Particularly the prospect of phase matching a lower order HOM (EH-type of mode) which requires larger PM wavelengths motivates the core size reduction. Fibres with elliptical cores were employed already in the late 70's to preserve polarisation states [138]. Modes in eLCF are labelled with their respective original mode label as in case of the circular fibre and a superscript $\perp$ ($\parallel$) denotes polarisation perpendicular (parallel) to the semi major axis. It is to note that the following analysis applies to any elliptical SIF, yet here it is focused on eLCF for the purpose of THG in a C_2Cl_4 filled core.

Birefringent fibres are commonly operated exclusively in the single mode regime where only the two HE_{11} types of modes are guided. These two, which are now non-degenerate, and the first four HOMs are presented in Fig. 43 (b-f) for increasing Δ. In common notation $n_{eff}^{\parallel} > n_{eff}^{\perp}$ for HE_{11} modes and hence the polarisation parallel to the major axis is termed the slow axis, i.e. exhibits the lower phase velocity, and the perpendicular polarisation is associated with the fast axis. Whereas the deformation of the HE_{11} is barely visible despite the alignment of the electric fields, even the lowest order HOMs, such as TE_{01} (c), the two degenerate HE_{21} (d,e), and TM_{01} (f), rapidly transform their intensity, i.e. Poynting vector z-component, into double bell shapes resembling LP_{11} modes known from weakly guiding fibres [139], or the more general case of Ince-Gauss modes observed in elliptical Gaussian beams [140].

More noticeably the field vectors immediately align with either major or minor axis – moreover, these modes reveal that neither polarisation, nor core geometry alone predetermine the optical axis of a birefringent fibre which is a particular property of the fibre modes under consideration. It is to note that n_{eff} of the presented modes decreases from top to bottom and hence fast and slow axes interchange each time another pair of HOMs is considered, i.e. n_{eff} of mode (c) is larger than for (d) and it is larger for case (e) than for (f). This is in contrast to the common case where fast and slow axes are associated with the fibre geometry in commercial polarisation maintaining fibres, whose applications, however, are usually limited to the single mode regime.

For the THG process, modes of higher order are in focus as presented in Fig. 44. Significant transformation is observed for the EH_{12} mode in (a) forming a central intensity lobe from its initial dual ring intensity shape and again the electric field rapidly aligns with the ellipse axes. Modes of HE-type (b) undergo less drastic transformation and the field orientation remains largely unaffected.
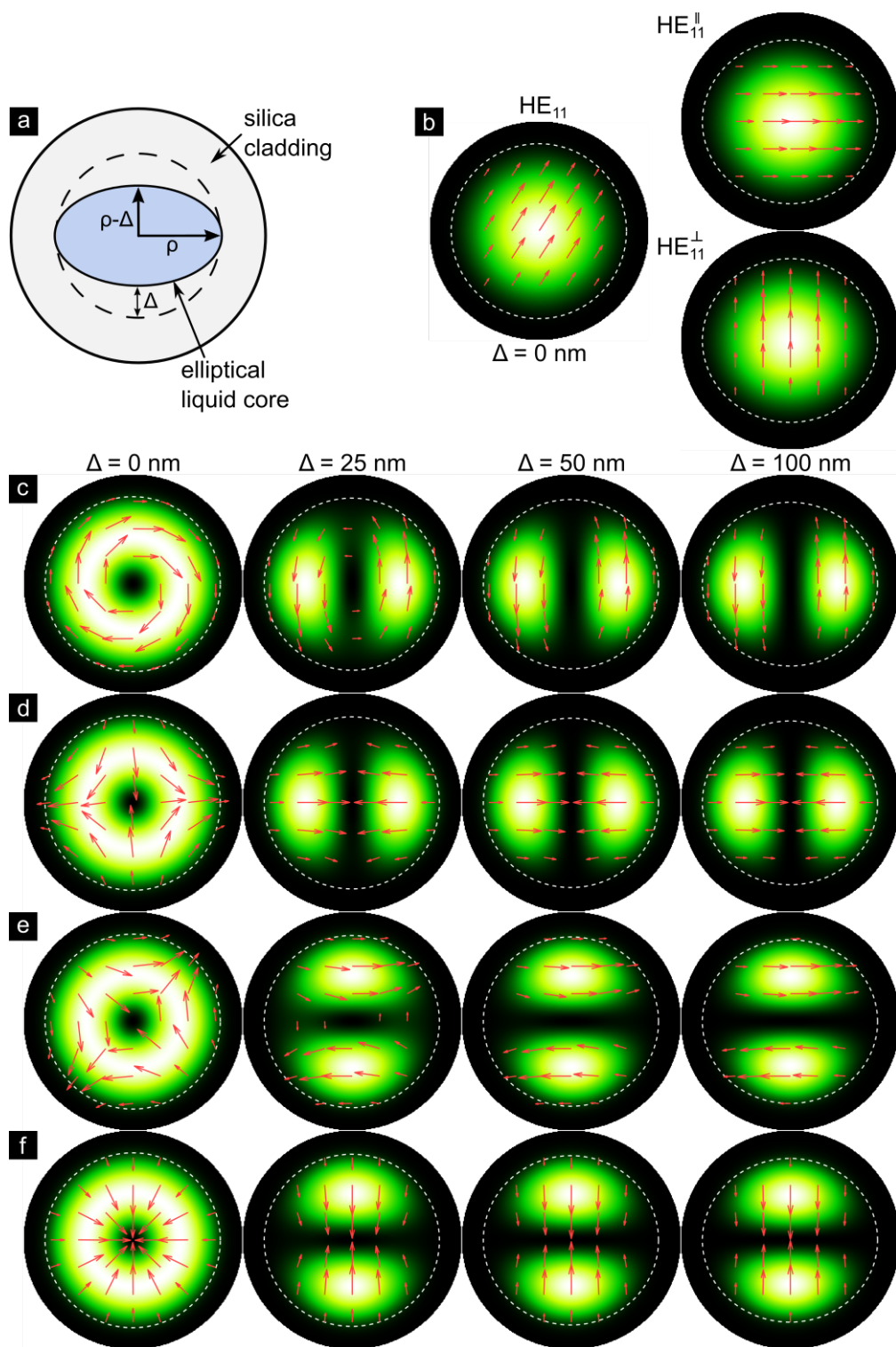
Fig. 43: Overview of modal transformation in elliptical fibres. (a) Schematic of cross section. Poynting and electric field vectors are shown for bound modes for ellipticity Δ as stated, silica cladding, TCE core and $\rho = 1.6\,\mu m$. $\lambda = 500\,nm$. The dashed white line indicates the core. (b) HE_{11}, (c) TE_{01}, (d,e) HE_{21}, (f) TM_{01}. n_{eff} decreases from top to bottom. See text for further details.
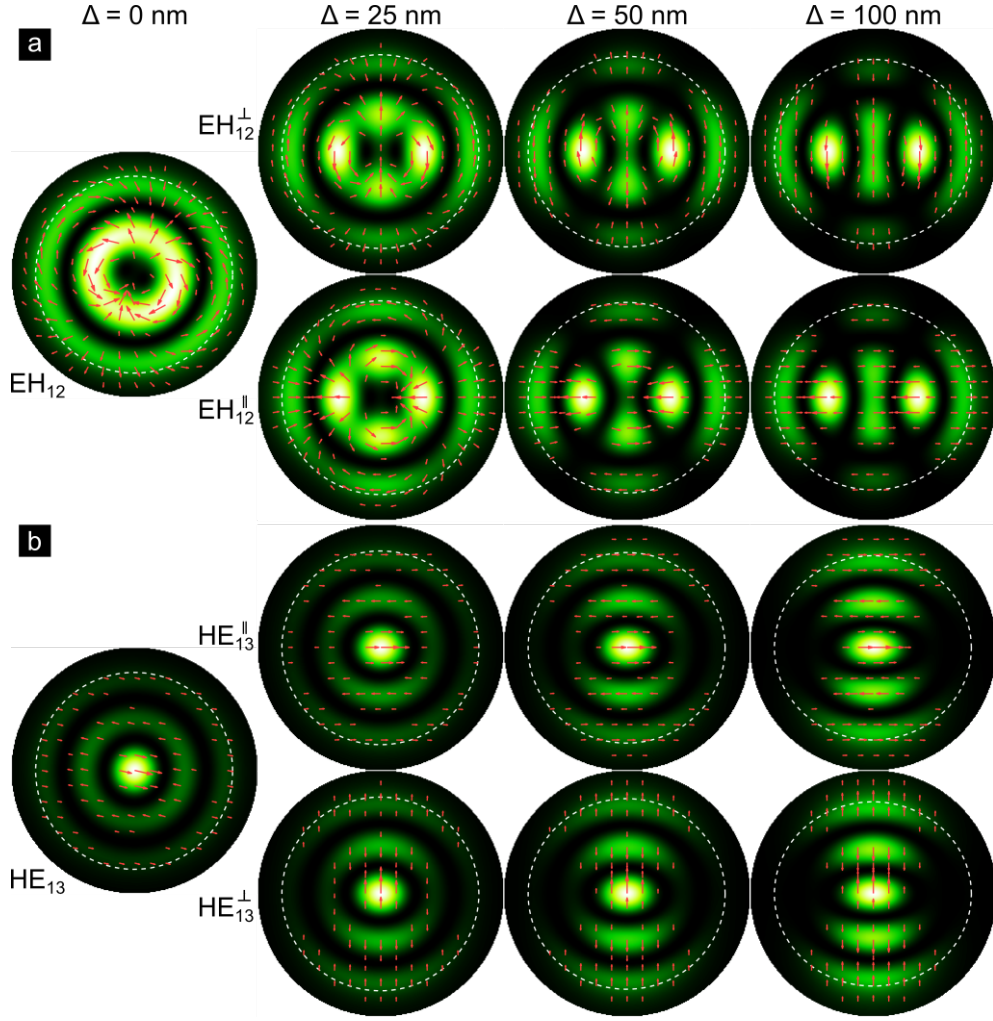
Fig. 44: Transformation of HOM in elliptical fibre for ellipticities as stated on top. Parameters as in Fig. 43. EH$_{11}$ (a) and HE$_{13}$ (b) modes split into parallel and perpendicularly polarised modes. n$_{eff}$ decreases from top to bottom and the core is indicated by the white dashed line. Adapted from [133] © OSA (2020).

4.4.2 Quantitative Analysis of Modes in elliptical LCF

In order to quantify the visual change of modes the mode field diameter (MFD)

$$MFD_x = \frac{\int_{-\infty}^{\infty} x^2 S_z \mathrm{d}A}{\int_{-\infty}^{\infty} S_z \mathrm{d}A},$$
(41)

along direction x (y), which here is associated with the semi major (minor) axis direction, is introduced as well as the ratio of polarisation (ROP)

$$ROP = \frac{\int_{-\infty}^{\infty} |E_x|^2 \mathrm{d}A}{\int_{-\infty}^{\infty} |E_x|^2 + |E_y|^2 \mathrm{d}A},$$
(42)

which is a measure of the relative amount of power carried by the respective polarisation direction. These quantities are presented in Fig. 45 (a) for modes relevant for the THG process evaluated at representative wavelengths (see figure caption); the

MFD ratio (left axis), i.e. MFD_y / MFD_x, of these modes is initially 1 due to the circular symmetry and is a measure how much the modes expand (MFD ratio < 1) and squeeze (MFD ratio > 1) along the semi major axis. The right axis shows the ROP for the EH_{12} modes (note in case of HE_{13} modes the ROP is not affected) indicating strong field alignment for $\Delta \approx 60$ nm, i.e. a change less than $\lambda_{TH}/8$. A benefit thereof is the enhancement of modal coupling discussed below. Panel (b) shows the contrast of effective indices, i.e. birefringence, of the respective modes for THG (e.g. pump at 1551 nm, harmonic at 517 nm); positive and negative values indicate the flip of orientation of the fast and slow axes in case of HOMs. Interestingly, birefringence peaks for Δ close to 90 nm and decreases monotonically thereafter for HE_{13} even below zero where fast and slow axis interchange yet again. It is to note that these modes are rather close to their respective modal cut-off due to the reduced core size in this case. Similarly, for EH_{12} modes the index contrast exhibits a local minimum after which the birefringence reduces again. This peculiar behaviour is associated with the field structure of the modes and the amount of tangential and perpendicular field components at the core cladding interface which alters in case of decreasing core area. The birefringence for the pump mode increases monotonically as expected from fibres with increasing ellipticity at a rate of $4.5 \cdot 10^{-7}$ nm^{-1} and at a rate of $7 \cdot 10^{-8}$ nm^{-1} with λ within the investigated parameter range.
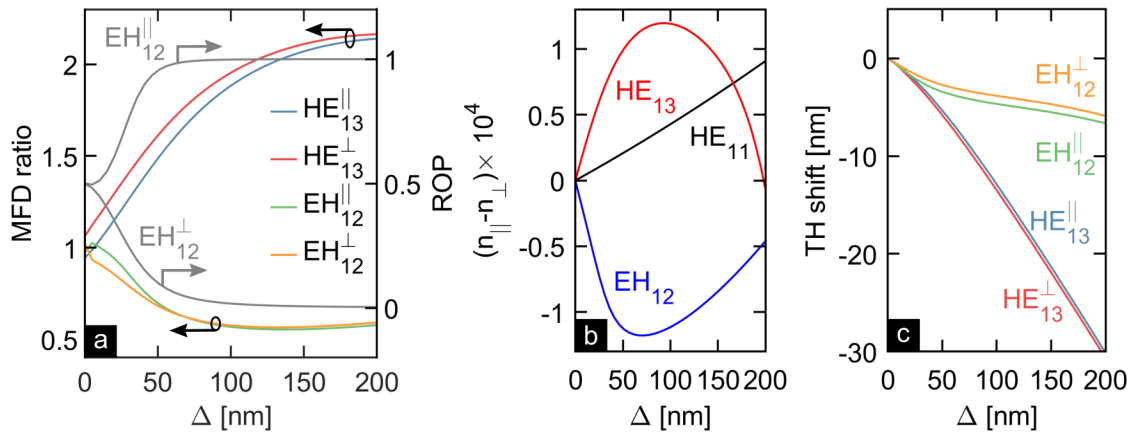
Fig. 45: (a) Ratio of MFD_y / MFD_x (left axis) evaluated at 520 nm (500 nm) for EH_{12} (HE_{13}) modes. ROP (right axis) for EH_{12} modes. (b) Birefringence for pump (HE_{11}, 1551 nm) and TH (HE_{13} and EH_{12}, 517 nm) modes. (c) Shift of λ_{PM}. In the circular case $\lambda_{PM}^{HE_{13}} = 516$ nm and $\lambda_{PM}^{EH_{12}} = 528$ nm. Adapted from [133] © OSA (2020).

The shift of λ_{PM} due to Δ is presented in panel (c). A shift towards shorter wavelengths results from the overall reduction of the core size, the steeper decline for the HE-type modes is inferred from the modal expansion along the minor axis. Due to

this transformation HE_{13} modes mainly probe the nearby core cladding interface and closely follow the PM wavelengths of a circular fibre with radius of the minor axis (not shown for clarity) resulting in a linear shift of -32 nm for up to 200 nm ellipticity. Note that EH_{12} modes in a circular fibre experience the same shift. In contrast, in the elliptical fibre the shift of the EH_{12} modes is much less steep since they are elongated along the major axis utilising more of the available high IOR core area.
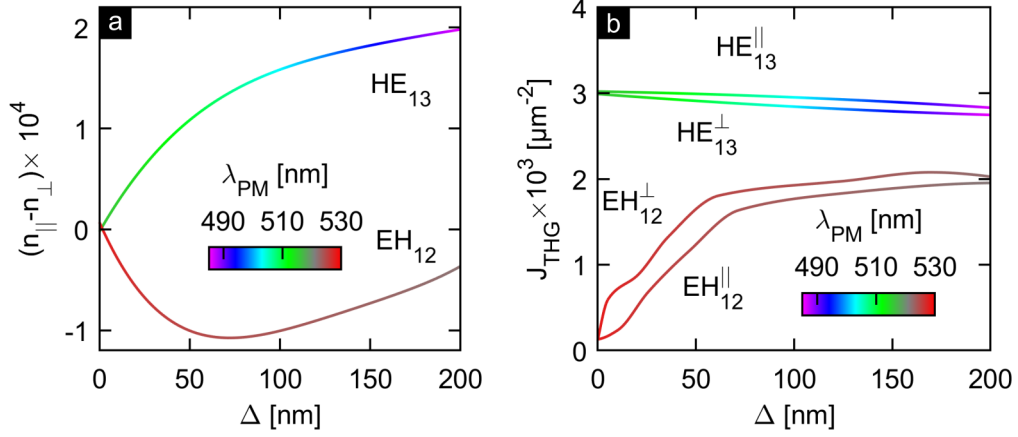
Fig. 46: (a) Birefringence and (b) modal coupling constant at λ_{PM} for EH and HE type modes as represented by the colour map. λ_{PM} was averaged among the two polarisations in (a). Adapted from [133] © OSA (2020).

In Fig. 46 the combined effects of Δ and the resulting λ_{PM} on birefringence (a) and modal coupling constant J_{THG} (b) are presented for the targeted THG application. It is to note that due to the reduction of λ_{PM} the reduction in core size probed by the HE type modes is compensated, i.e. $n_{\parallel} - n_{\perp}$ monotonically increases, whereas for EH modes the index contrast shows less dependence on λ_{PM}. The most remarkable effect, already indicated by the ROP in Fig. 45 (a), is the enhancement of J_{THG} by more than one order of magnitude compared to a circular fibre making this mode accessible experimentally.

In [141] multiple THG modes from highly germanium doped elliptical SIF were reported, yet their analysis based on scalar Ince-Gauss modes did not reveal the intricate transformation of electric fields leading to enhanced coupling of such modes.

4.4.3   Experimental THG in elliptical LCF filled with TCE

To confirm the modal analysis, i.e. intensity and field transformations, THG experiments are performed in TCE filled eLCF. To this end a capillary which was drawn under relatively high collapsing ratio of about 64 % with a hollow core with semi major axis $\rho = 1.6$ µm and $\Delta \approx 60$ nm – 80 nm was deployed. The 90 fs laser system served as pump

source and recorded data is presented in Fig. 47 for which the horizontal pump polarisation was used. Panel (a) presents a THG spectrum in linear scale along with the respective portion of the pump spectrum (normalised to its respective peak beyond the axis limits). Note the wavelength axes in (a) and (b) show equivalent ranges. Insets show experimental farfield images of the modes in agreement with simulation. Band pass filters were used to capture these modes individually. The third mode visible in the log-scale power spectral evolution in (b) probably originates from an even higher order mode, namely the HE_{32}, as phase matching calculations suggest. Due to the weak signal and proximity to the other strong modes no farfield images could be taken in this case. It is to note the relative strength of HE_{13} and EH_{12} modes is not reflected in this measurement due to chromatic dispersion. When coupling the signal into the collection fibre the focus is adjusted for optimum power and remained unaltered during data recording.
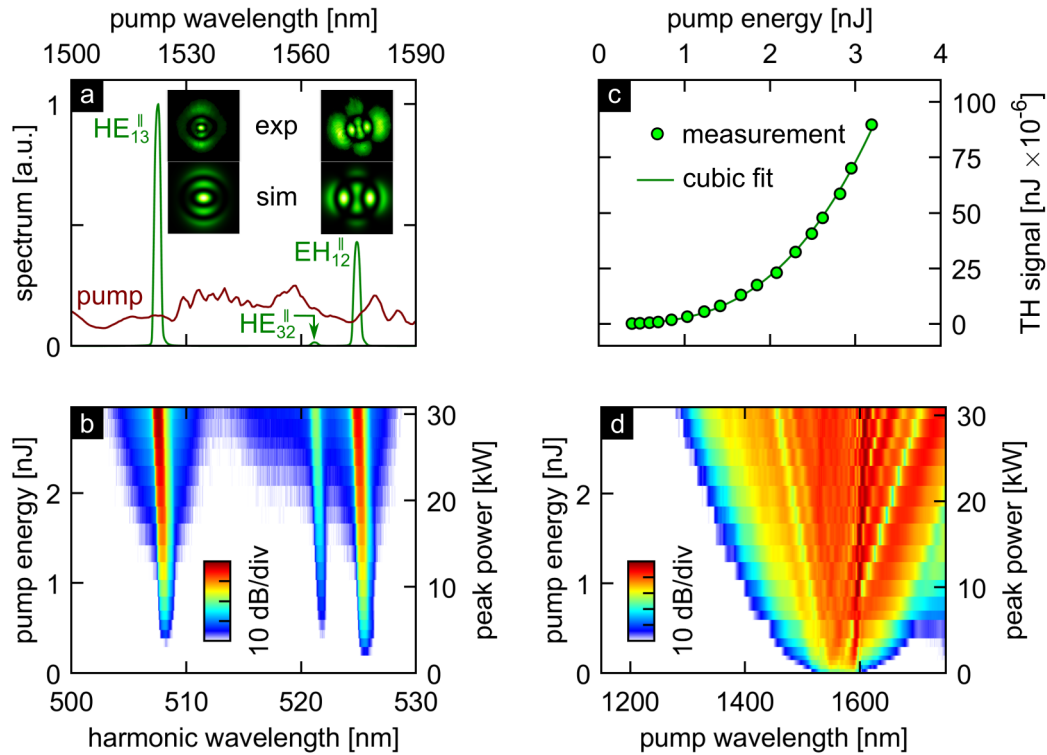
Fig. 47: Experimental results of THG in TCE filled eLCF with $\rho = 1.6\,\mu m$ and $\Delta \approx 70\,nm$. (a) Harmonic and pump spectrum (limited range, linear scale). Insets show experimental farfield and simulated intensity. Power spectral evolution of harmonic (b) and pump (d). Adapted from [133] © OSA (2020).

In (b) a phase matched bandwidth of 630 pm for both modes and a blue-shift at a rate of $R_{\delta\lambda}^{E} \approx -250\,pm/nJ$ is extracted which is consistent throughout all previous measurements. The eLCF is normal dispersive in both pump polarisation axes and SPM

based spectral broadening is observed as shown in (d). THG powers measured directly in free space are shown in (c) along with a cubic fit to the data. The slope efficiency obtained is $s = 2.7 \cdot 10^{-6}$ nJ^{-2}, while a conversion efficiency $\eta_{\text{exp}} = 2.8 \cdot 10^{-5}$ (3.3 µW TH signal from 128 mW pump) was achieved.

In the following the polarisation properties deduced from modelling are validated experimentally and results for the EH$_{12}$ type modes are shown in Fig. 48. To this end the input polarisation is adjusted such that either perpendicular (a) or parallel (b) THG yield is optimised, subsequently the farfield images are captured without linear polariser (1$^{\text{st}}$ column) and with a linear polariser once in parallel (2$^{\text{nd}}$ column) and once in perpendicular orientation (3$^{\text{rd}}$ column). The transformation of electric fields is evident as high contrast among the two polarisation axes is observed. A further, more sophisticated approach to analyse anisotropy in elliptical fibres was presented in [26].

Residual light in the outer area in (a-2) and (b-3) is likely to originate from the sapphire window acting as retardation plate for non-normal incidence leading to elliptically polarised light and retardation increases with angle of incidence, i.e. towards the outer region of the mode.
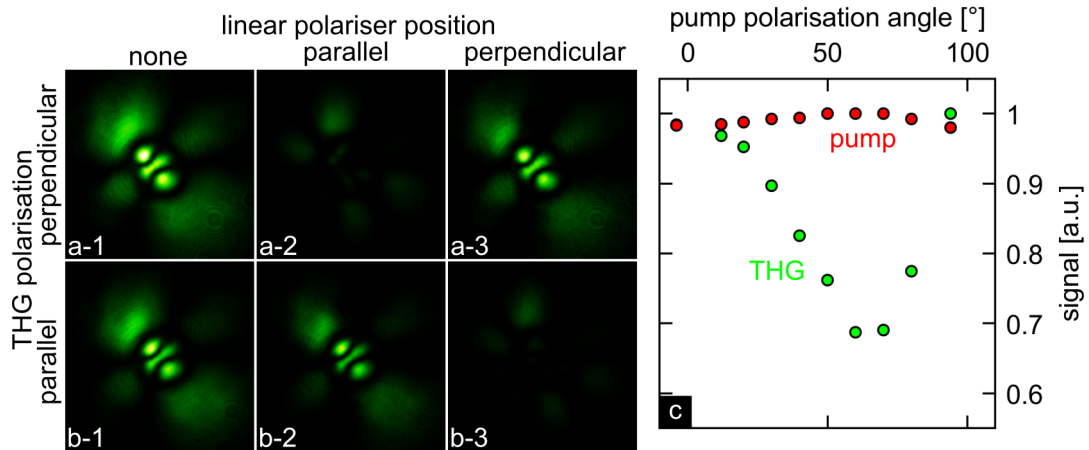
Fig. 48: Farfield images of EH$_{12}$ modes for perpendicular (a) and parallel (b) excitation. A linear polariser (LP) was inserted before the camera as indicated for columns 2 and 3. Images in column 1 are recorded without LP. (c) Normalised output signal for scanned input polarisation. Adapted from [133] © OSA (2020).

Scanning the input polarisation (c) demonstrates the crucial dependence of the signal yield in case of birefringent fibres on launching conditions. While the transmitted pump power is stable (red dots) the THG signal (green dots) drops by 30 % when coupled power is split among the fast and slow axis proving each individual polarisation state generates THG. Full signal strength is recovered after 90° rotation as expected.

Finally, the shift of λ_PM due to birefringence is revealed by an experiment deploying a slightly larger eLCF with semi major axis of 2 μm and ellipticity of approximately 70 nm which allows investigating a larger number of modes at a time. In Fig. 49 (a) the resulting THG spectrum and farfield images are shown as insets. The modes observed earlier are shifted towards longer wavelength. As shown in Fig. 45 (c) the shift of λ_PM is expected to be larger in case of the EH_{12} mode pair. Panel (b) of Fig. 49 shows a well resolved shift of the PM wavelength for parallel, perpendicular and intermediate input polarisation. The shift is also apparent in colour for the case of EH_{12} modes (not shown), whereas in case of the other modes no such change is observed.
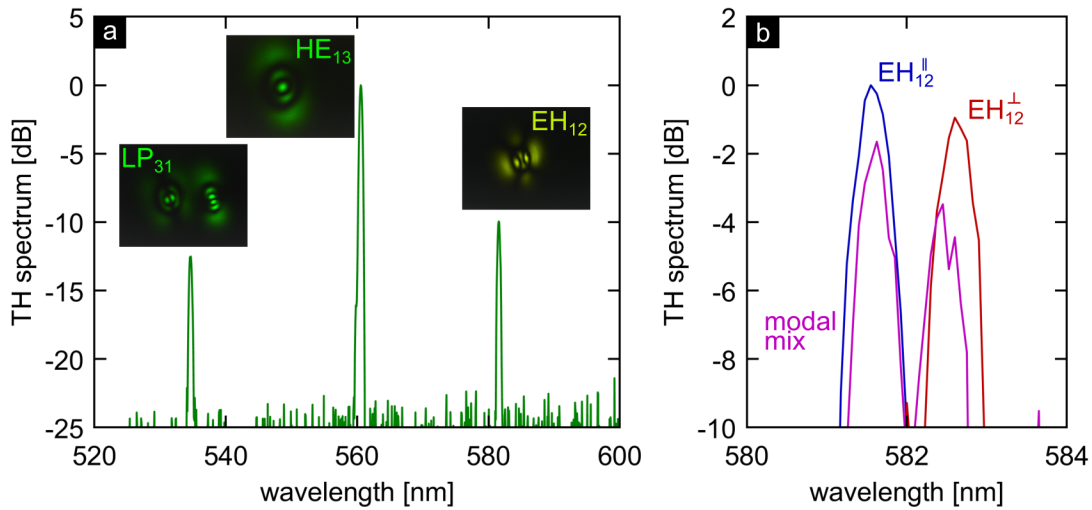
Fig. 49: (a) THG spectrum and farfield images as insets from a TCE-eLCF with $\rho = 2$ μm and $\Delta \approx 70$ nm. (b) Spectra for different polarisation conditions revealing a shift in λ_PM for parallel and perpendicular excitation.

It is to note, that an additional pair of modes is observed in panel (a) which, in contrast to the former modes, does not originate from a HE_{11} like pump mode, but rather originates from a pump in a HOM as shown in Fig. 43 (c-f) with a double bell shape usually referred to as linearly polarised (LP) modes. Strong dependence of the LP_{31} modal intensity on coupling conditions was observed which is attributed to preferentially exciting one of the two modes in parallel or perpendicular polarisation by a transverse focal shift at the fibre facet switching among the modes shown in Fig. 43 (c,f) or (d,e), respectively. Sufficient signal generation even for higher order pump modes enabling dispersive properties that usually require microstructured fibres [142] can allow multi-wavelength signals similarly to recently demonstrated supercontinuum induced THG in a suspended core fibre [19].

4.5 Tuning Potential via Temperature Control

In this section the ability of liquid core fibres to adjust phase matching on demand are highlighted. Tunability can become an important aspect in THG to compensate manufacturing insufficiency or environmental conditions. Whereas longitudinal adjustment of the core size leads to a static change in the PM wavelength (see Fig. 32, p. 56), dynamic control can be utilised exploiting the liquids thermo optical coefficient (TOC). Recent broadband measurements in a fibre coupler form the basis of the analysis [47]. To account for temperature dependence, the refractive index is assumed to have the following form: $n(\lambda, T) = n(\lambda) + TOC \cdot \Delta T$, where ΔT represents the temperature deviation from 20°C. Hence dispersion of the TOC towards near infrared is neglected for calculations of the wavelength shift $\delta \lambda_{\mathrm{PM}}$ from its original value for 20°C.

Fig. 50 presents the PM shifts accounting for the TOC in both core and cladding for C_2Cl_4 (a) and CS_2 (b,c) cores for the respective modes as stated in the panels for various core diameters. $TOCs$ for all cases are given in the caption.
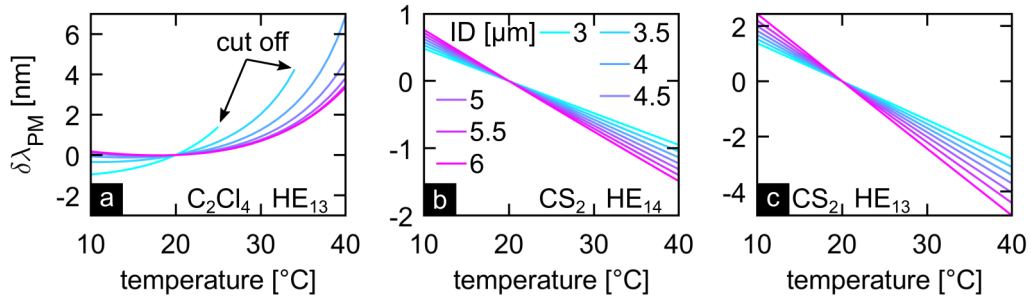
Fig. 50: Shift of phase matched wavelength $\delta \lambda_{\mathrm{PM}}$ due to temperature in a circular SIF. (a) C_2Cl_4, mode HE_{13}, (b) CS_2, mode HE_{14}, (c) CS2, mode HE_{13}. Legend with inner diameters (ID) applies to all panels. TOCs are assumed equal for pump and harmonic and amount to: 0.1 (silica cladding), -6 (C_2Cl_4), -8 (CS_2) in 10⁻⁴/K [47]. Cut off behaviour is explained in the text.

Since the TOC for the liquids is negative and much greater in absolute value compared to silica, the fibre NA reduces with increasing temperature and so does the V parameter. This resembles a reduction in core size and therefore the reduction in λ_{PM} in case of CS_2 (b, c) is understood intuitively. A linear slope which depends on core size is observed within the investigated range of temperatures. In case of C_2Cl_4 (a) the situation is different, here the initial NA of the fibre is lower compared to the CS_2 case and the phase matched HOM is closer to cut off. In such cases dispersion of modes varies more strongly as is evident from the curvature of $\delta \lambda_{\mathrm{PM}}$ in (a). For core diameters of 3 μm and 3.5 μm the HOMs cut off in the temperature range, however, this cut off is determined

numerically, whereas physically the mode starts leaking into the cladding leading to propagation loss rather than abrupt disappearance.

Experimental results in a temperature controlled eLCF filled with C_2Cl_4 as in section 4.4.3 are presented in Fig. 51. A 5 cm long peltier element placed directly after the opto-fluidic mount was used to heat and cool part of the fibre. Panel (a) presents measured TH power exhibiting signal reduction for temperatures beyond 35°C, which is in good qualitative agreement to calculations in circular fibres with similar core size.
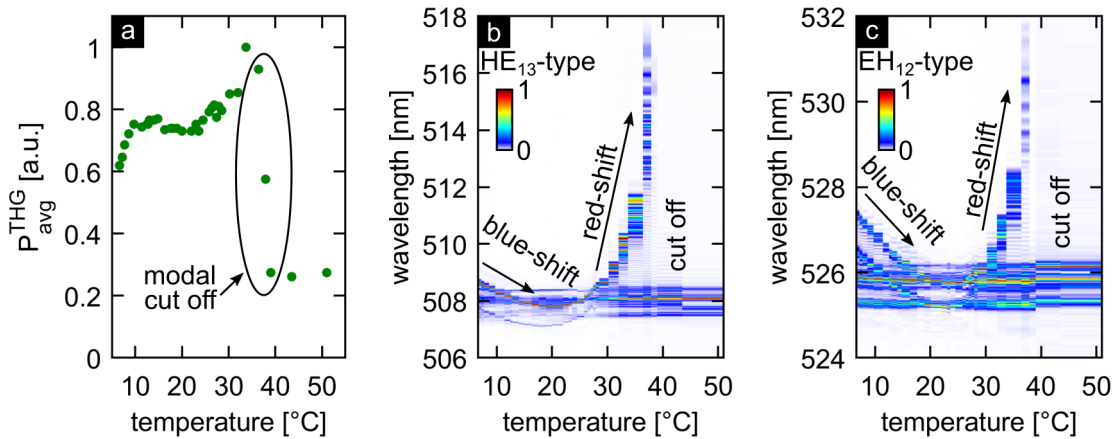
Fig. 51: Experimental shift of phase matching in an elliptical fibre ($\rho = 1.6\,\mu m$, $\Delta = 60\,nm$, C_2Cl_4 core). A 5 cm peltier element placed directly after the optofluidic mount ($\approx 2\,cm$ behind input facet) was used to control temperature of a 15 cm fibre. (a) Normalised temperature dependent TH output power. Temperature dependent TH spectra (linear scale, individually normalised) for HE_{13}-type (b) and EH_{12}-type modes (c). Non-shifted harmonic signal in (b, c) result from fibre parts with unaltered temperature of 21°C-22°C.

Spectral changes with temperature are presented in (b) and (c) for the two types of modes. Since part of the fibre remained at ambient temperature unaltered spectral components are evident at 508 nm (b) and 526 nm (c). Temperature dependent features exhibit an initial blue-shift towards ambient temperature (≈ 22°C), followed by a red-shift. These features vanish beyond 35°C due to modal cut off. Note, the pump polarisation was not aligned with ellipse axes and hence two spectral lobes are observed particularly in (c). Temperatures from 20°C to 35°C allow shifts of 4 nm (b) and 2 nm(c), i.e. at a rate of 0.26 nm/K and 0.13 nm/K, before the cut off. Similar rates are expected for CS_2 (Fig. 50 (c)) without approaching a cut off making this tuning scheme compatible to tapers in pressurised gas cells (0.12 nm/bar in Ref. [28]), while temperature tuning in solid core fibres is less sensitive (0.015 nm/K in Ref. [29]).

4.6 Long-term Stability and High Power Delivery in Liquid Core Fibres

The many recent reports of nonlinear effects in LCF clearly show that sufficiently high peak powers can be launched into such fibres – the remaining issue is a persistent worry that high average powers lead to thermally induced damage or boiling. Since high flux of photons is important to achieve high data acquisition rates with low noise figures for e.g. spectroscopic applications the long-term stability under such launching conditions in LCF filled with CS_2 and C_2Cl_4 was investigated.

To this end SCG in the AD domain was identified as most suitable nonlinear effect to contest LCF durability on long terms as it can be benchmarked with many other reports and the formation of typical spectral features such as solitons and dispersive waves (DWs) are more susceptible to fluctuations than continua generated in the ND regime. Experimental results were published in [130] in cooperation with the FS-LA group of the DESY synchrotron facility in Hamburg providing a state of the art Tm-doped fibre laser operating at 380 MHz which allowed to demonstrate record high average power SC from LCF as well as stable beam delivery above one Watt.

4.6.1 Stable High Power Beam Delivery in Large Core LCF

In order to push the limits of LCFs in terms of average power both a potent pump laser delivering femtosecond pulses and optimal fibre coupling conditions are necessary. In general larger cores are less restrictive in coupling efficiency from free space beams, as is the case here. Among the different core diameters under test a 20 μm core size allowed launching the maximum laser average power of 1.6 W with an efficiency of > 80% into the fibre. In Fig. 52 (a) the launched power is shown versus time. The power was calculated from the measured output power compensating reflection losses at window interfaces and propagation loss. Whereas for C_2Cl_4 propagation loss is negligible (0.23 dB/m) a pronounced absorption line near 1.95 μm in CS_2, already indicated in Fig. 27 on p. 49, partially overlaps with the laser pump spectrum resulting in propagation loss of 4.23 dB/m in the 15 cm LCF, i.e. 86 % transmission. For both liquids the power remains stable for the shown 90 minutes and beyond – since no sign of degradation was observed no further tracking was considered. A root-mean-square stability of 0.5 % and below is obtained. The beam profiles shown in (b) for CS_2 and (c) for C_2Cl_4 indicate good beam quality at the highest power level.
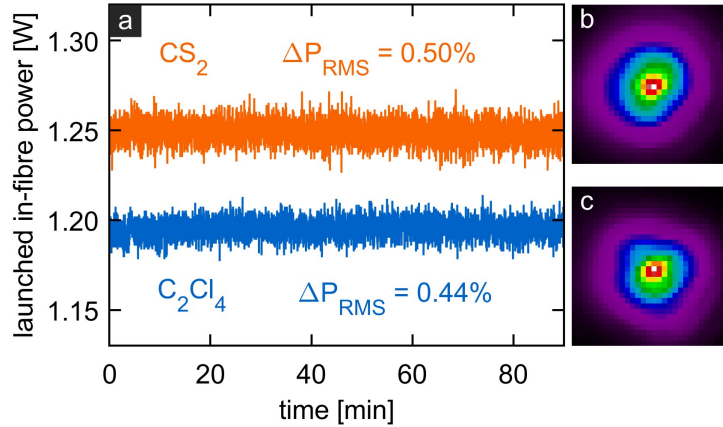
Fig. 52: Launched in-fibre average power for 20 µm core diameter LCF calculated from measured output power (a). Root mean square fluctuations are given for CS_2 and C_2Cl_4. Output beam profiles for CS_2 (b) and C_2Cl_4 (c) confirm guidance in the core. Reprinted from [130] © OSA 2019.

To ascertain the power was not transmitted in the cladding the LCF was bent slightly and immersed in index matching oil while monitoring power. No reduction in transmission was observed.

4.6.2 Record Average Power Supercontinuum in Liquid Core Fibre

SCG mediated by fission of higher order solitons is an excellent test scenario for long term stability, as soliton fission and subsequent DW emission are considered more susceptible to external fluctuations than SCG in the ND domain which is dominated by SPM and subsequent optical wave breaking [69]. The LCF is required to exhibit anomalous dispersion, i.e. $\beta_2 < 0$ using the core size to tune the ZDW. However, this procedure is more limited than in case of microstructured fibres [108]. It must be noted that recent works experimentally verified mixtures of different liquids in the core allow shifting the ZDW towards the 1.55 µm regime [41,42] and exploiting higher order modes in CS_2 filled LCF enabled the use of two ZDW in SCG as in [142]. However, the approach taken here focuses on pumping the fundamental mode.

Fig. 53 shows the respective ZDW (solid lines) for CS_2 (a) and C_2Cl_4 (b) for various core diameters. Green and purple shaded areas represent AD and ND, respectively. Dashed horizontal lines represent the respective bulk ZDWs. In general the AD domain is located above the given lines and the ND domain resides below.
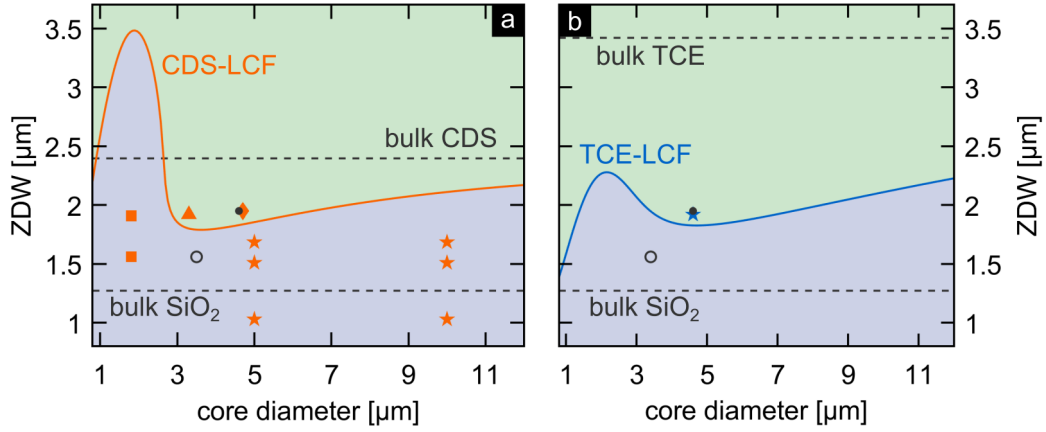
Fig. 53: Zero dispersion wavelengths (ZDW) for CS₂ (a) and C₂Cl₄ (b) filled LCF in the fundamental HE₁₁ mode. Bulk ZDW are indicated as dashed lines. AD domain lies above solid/dashed lines, ND domain lies below solid/dashed lines. Symbols: (a) ■ [36], ★ [37], ▲ [40], ◆ [38], (b) ★ [39]. Grey ○ and ● represent THG experiments and high power SCG from this work, respectively. Adapted from [130], © OSA 2019.

Different symbols highlight experimental configurations from literature and this thesis (see caption). Strong waveguide dispersion is evident in (a) in the range of 1.8 μm to 2 μm cores that allows normal dispersive pumping up to 3.3 μm, exceeding either bulk ZDW. The ranges of core sizes between 3 μm to 5 μm for CS₂ and 4 μm to 5 μm for C₂Cl₄, respectively, exhibit a pronounced ZDW reduction which is ideal for pump lasers around 2 μm targeting the AD domain.

Experimental verification of soliton mediated SCG via fission and DW generation is shown in Fig. 54. The power spectral evolution was recorded for CS₂ (a) and (b) and C₂Cl₄ (c) and (d) using a grating based spectrometer to capture the DW side and a Fourier transform spectrometer for the range of the pump and solitons. Spectral overlap could not be achieved due to the devices bandwidth limitations. Therefore each panel is normalised with its respective maximum. Left axes correspond to the launched pulse energy and right axes correspond to measured output average power.

Fission occurs at the indicated launched pulse energies for CS₂ (a) and C₂Cl₄ (c) where a distinct DW is first generated. Due to the larger nonlinearity in CS₂ the DW signal is much more pronounced and broadband and at the same time the extension towards the mid-infrared exceeds the one for the C₂Cl₄ LCF despite the strong absorption peak around 2.2 μm in case of CS₂. Still, the onset of DW emission occurs at $N \approx 11$, where N is the soliton number, in either case. Phase matching calculations agree with the experimental DW wavelengthts ($\lambda_{DW} = 1.4\,\mu m$ (a) and $\lambda_{DW} = 1.36\,\mu m$ (c)) assuming a higher order soliton at 1.95 μm.
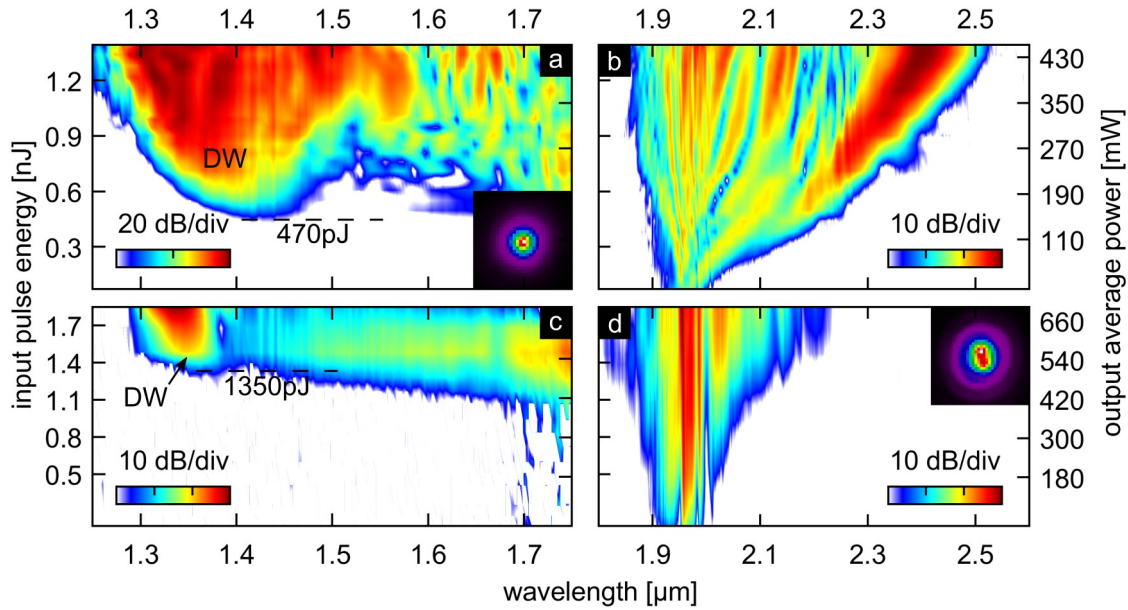
Fig. 54: Power spectral evolution of SCG in CS$_2$ (a, b) and C$_2$Cl$_4$ (c, d) filled fibre. Each panel is normalised individually. Fission is indicated at the onset of dispersive wave (DW) generation. Insets show experimental beam profiles.

The results from above represent the highest average power continua generated in a LCF to date and their stability was investigated by capturing both output power and output spectra for an extended period of time. For this experiment the CS$_2$ LCF was chosen and pumped at the highest possible power. Fig. 55 presents the acquired long-term data. A CaF$_2$ window served as beam splitter to capture spectra and the direct output power with an automated measurement routine for a 72 hour period.

In (a) the spectra are shown, whereas (b) shows integrated spectral intervals of pronounced features (red: pump, blue: soliton) on the left axis and the direct power measurement on the right axes. The experiment was initiated and running freely during the weekend resulting in a moderate reduction of power observed at the pump wavelength but a sizable reduction in power in the 2.3 µm to 2.6 µm interval which underpins the sensitivity of the SCG process to fluctuations.

Since the pump source showed no evidence for reduced power delivery the mechanical components were realigned after 48 h as indicated in (b). As the output power was re-established effortlessly data acquisition was continued. The slow decrease in power is assigned to the drift of mechanical components rather than high average power induced damage of the LCF sample. These results in conjunction with previous work where higher pulse energies were launched in such fibres at lower repetition rates [38] point towards the potential of such LCFs beyond scientific research.
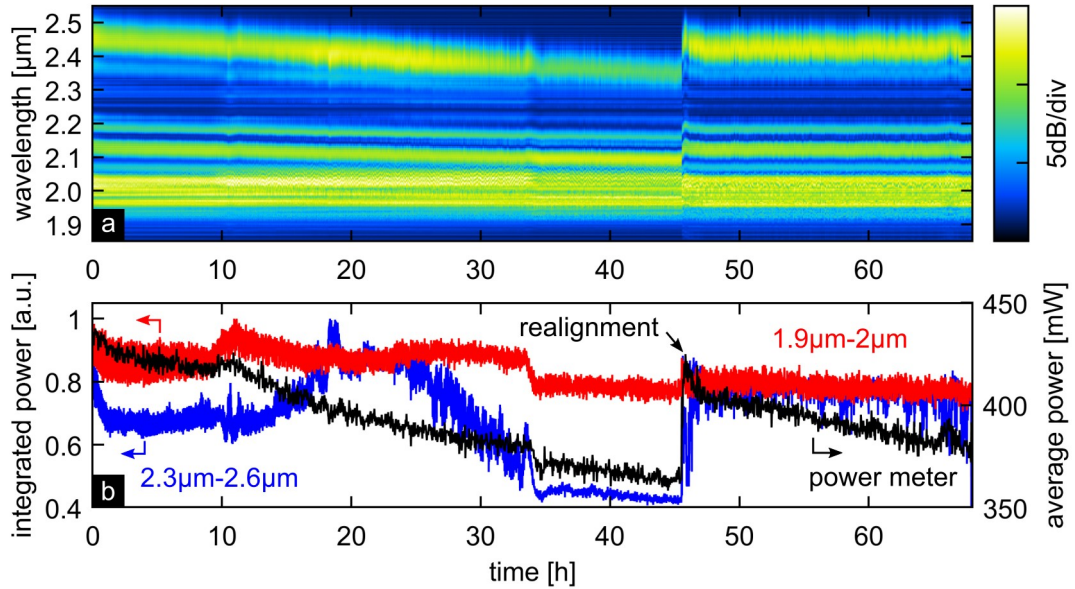
Fig. 55: Long term acquisition of spectra (a) and output power (b) of a CS$_2$ LCF pumped at 1.95 μm. Red and blue lines in (b) are integrated ranges from data in (a) as stated. After 48 h coupling optics were aligned again restoring the initial power almost completely.

4.6.3 Overview of Damage Thresholds in Liquid filled Fibres with CS$_2$ or C$_2$Cl$_4$

This subsection presents an overview of recent experimental results in LCF filled either with CS$_2$ or C$_2$Cl$_4$ compiled in Table 8 and Table 9, respectively. Laser parameters and the respective powers and energies endured by LCFs during experiments are collected from literature and experiments conducted in this thesis. If not provided in the article missing values are calculated as detailed in the table caption.

No claim to completeness is raised for the given list and it is to note that reported values not always represent the damage threshold, i.e. in case of insufficient laser power. Yet, all experiments aimed for nonlinear frequency conversion via SCG or THG which suggests the highest power available was employed. Despite the sizeable number of data no general power limits can be extracted. Whereas more than 300 MW/cm² peak intensity was possible to launch for either liquid the maximum fluence of 200 mJ/cm² for CS$_2$ allowed for only 200 MW/cm² intensity indicating complex dependence of energy and power related parameters. Future research may address the issue of correlations between fluence, average and peak powers as well as wavelength dependence making operational domains for LCFs more predictable. Momentarily CS$_2$ and C$_2$Cl$_4$ LCFs seem to hold potential to further scale up power in combination with laser sources providing repetition rates of several tens of MHz as is common for nowadays fibre lasers.

Table 8: Overview of experimental power capabilities in CS_2 LCFs. The given parameters are extracted from literature and converted accounting for transmission or other losses if stated. Unless specified, calculated values discard functional shapes, i.e. peak powers are calculated as $P_0 = E_p/\Delta t$, the fluence is determined as $\Phi = 4E_p/(\pi\,ID^2)$, with the inner diameter (ID) of the core, and intensity is obtained from $I_0 = \Phi/\Delta t$, with Δt as FWHM pulse duration. Experiments conducted in this thesis are highlighted by * in the last column.

λ_0 [μm]	ID [μm]	E_p [nJ]	P_{avg} [mW]	P_0 [kW]	Δt [fs]	f_{rep} [MHz]	Φ $\left[\frac{mJ}{cm^2}\right]$	I_0 $\left[\frac{GW}{cm^2}\right]$	Ref.
1.56	1.8	-	200	-	CW	-	-	-	
1.56	1.8	0.76	32	1.9	400	42	29.9	74.7	[36]
1.91	1.8	1.53	61.2	8.4	180	40	60.1	334	
1.03	5	0.85	35	1.7			4.35	12.4	
	10	1.71	70	3.4			2.17	6.21	
1.51	5	0.59	24	1.1	>350	41	2.98	8.52	[37]
	10	2.20	90	5.5			2.79	7.99	
1.69	5	0.41	17	<1			-	-	
	10	0.61	25	1.1			-	-	
1.56	3.1	0.32	25.6	10.7	30	80	4.23	141	[108]
		0.63	25.2	7	90	40	8.35	92.8	
1.56	3.5	0.9	72	30	30	80	9.35	312	
	3.5	2.88	115.2	32	90	40	29.9	333	*
	3.5	4.97	1.988	5.52	900	0.4	51.7	57.3	
1.95	4.7	16	40	34.78	460	2.5	92.2	200.5	
		15.13	85	32.88	460	5.6	87.2	189.5	[38]
		7.83	88	17.02	460	11.24	45.1	98.1	
1.92	3.3	1.8	45	5.14	350	25	21.0	60.1	[40]
1.95	4.6	1.4	532	12.73	110	380	8.42	76.6	[130]*
	20	3.29	1250	29.9	110	380	1.05	9.52	

Table 9: Overview of experimental power capabilities in C_2Cl_4 LCFs. Parameters are evaluated as for Table 8. Experiments conducted in this thesis are highlighted by * in the last column.

λ_0 [μm]	ID [μm]	E_p [nJ]	P_{avg} [mW]	P_0 [kW]	Δt [fs]	f_{rep} [MHz]	Φ $\left[\frac{mJ}{cm^2}\right]$	I_0 $\left[\frac{GW}{cm^2}\right]$	Ref.
1.56	3.4	1	80	33.3	30	80	11.01	367.1	
		3	120	33.3	90	40	33.04	367.1	[118]*
		5.7	2.28	6.3	900	0.4	62.78	69.7	
1.56	4.9	0.84	67.2	28	30	80	4.45	148.5	[42]
1.92	4.6	3.06	76.5	9.97	270	25	18.41	68.19	[39]
1.95	4.6	1.86	707	16.9	110	380	11.19	101.7	[130]*
	20	3.16	1200	28.7	110	380	1.01	9.14	

5 Summary

In this thesis liquid core fibres (LCFs) were deployed as a new platform for third harmonic generation (THG) of ultra-short laser pulses. Such LCFs are formed by filling a highly nonlinear, molecular liquid into a silica capillary. Careful consideration of material properties based on existing dispersion data and new loss measurements identified carbon disulfide (CS_2) and tetrachloroethylen (C_2Cl_4) as most promising.

Either of these allows making fibres with high numerical aperture above 0.6 and 0.4, respectively, such that a sufficient number of higher order modes (HOMs) can be guided at the third harmonic (TH) wavelength. Considerations to achieve coherent signal build up, i.e. to achieve phase matching among the fundamental and harmonic wave, in LCFs is described in detail for the step-index geometry.

Both liquids exceed the nonlinearity of common silica material by a factor of 6.8 and 2.5, respectively, only accounting the purely electronic contribution. Additional contribution to nonlinearity originates from the molecular structure and the possibility to move freely in the bulk liquid upon excitation with an external field. These orientational effects give rise to a non-instantaneous response which in contrast to silica's Raman response is of no oscillatory nature and decay times of 1.5 ps – 4.5 ps are typical. The ratio of these molecular and electronic nonlinearity is as high as 17.5 for CS_2. To assess the influence of this response on spectral transformation due to self and cross phase modulation (SPM and XPM), i.e. a strong pump and weak harmonic wave, numerical simulations based on coupled nonlinear Schrödinger equations were conducted. A persistent frequency down-shift for the pump in both normal and anomalous dispersive domains is observed. XPM on the other hand leads to asymmetric spectral shifts for the harmonic depending on the relative group velocities and acquired delays along the fibre. The non-instantaneous response causes significant nonlinear phase (NLP) trailing the pump and slower waves experience enhanced frequency up-shifts. The measured material loss for the harmonic was found to be negligible which allows utilizing the fibre geometry.

THG was demonstrated experimentally using three different laser sources based on Erbium fibre lasers with pulse durations of 30 fs, 90 fs, and 900 fs harnessing different amounts of contribution from the molecular response. A 3.4 µm circular capillary was chosen admitting a detuning from the pump centre of 1.56 µm in favour of addressing

532 nm as TH wavelength in the HE_{13} mode in C_2Cl_4. Here the expected reduction in efficiency by 25 % for 900 fs and less than 20 % for shorter pulses is acceptable. Due to positive group velocity mismatch the harmonic trails behind the pump after generation.

Broadening dynamics in the normal dispersive domain were observed in agreement with simulations. Particularly 900 fs pulses exhibit the frequency down-shift caused by the molecular response at a rate of 5.8 nm/kW whereas the harmonics reduce peak wavelength at rates of 14, 29, and 104 pm/kW for 30, 90, and 900 fs pump pulses, respectively. In simulations blue-shift rates of 7, 29, and 153 pm/kW were obtained also indicating phase modulation of the harmonic by the delayed trailing phase of the pump. The efficiency was obtained by direct power measurement and at the highest experimental power was found to be in the range of $1 - 3 \times 10^{-5}$.

Further, in a CS_2 filled capillary with 3.5 µm core diameter simultaneous phase matching to a HE_{14} mode at 520 nm and a HE_{13} mode at 670 nm is demonstrated which is enabled by the extraordinarily high refractive index of CS_2. Whereas the pump remained at 1.56 µm, sufficient spectral broadening was required to provide radiation in the anomalous dispersive domain at 2.01 µm to pump the HE_{13} mode. For 900 fs a spectral centre shift of 9.2 nm/kW was observed due to the greater nonlinearity of CS_2, yet THG could be observed only for 30 fs and 90 fs pulses that reached the bandwidth required to pump the HE_{13} mode, whereas coupling to HE_{14} is less efficient due to the higher order of the mode. Harmonic spectra exhibited a stronger rate of blue-shift than in case of C_2Cl_4 due to the larger contribution of the molecular response. The experimental conversion efficiencies, despite the higher nonlinearity, amount to 10^{-6} (HE_{13}, 30 fs) and 10^{-7} (HE_{14}, 30 fs and HE_{13}, 90 fs).

In circular fibres the number of accessible modes is limited and the degree of polarisation for the pump can degrade lowering also efficiency in THG. Therefore the effect of birefringence in a LCF was investigated in view of THG which further provides insights to birefringent modes in fibres beyond the set of fundamental modes. An elliptical core was modelled by finite element simulations considering the difference of major and minor axis Δ. Breaking the circular symmetry lifts modal degeneracy and modes transform both their intensity and field distribution. The latter exhibits an increasing degree of alignment with the geometric axes of the ellipse.

The change in modal shape is associated with a change in propagation constants leading to birefringence. Whereas birefringence increases monotonically for the

fundamental modes, this behaviour is different for HOMs. Specifically, HOMs originating from HE_{13} and EH_{12} modes exhibited a maximum difference of propagation constants for $\Delta = 60\,\text{nm}$ which was evaluated for 517 nm wavelength. The subsequent reduction is due to the eventual approach of their respective cut-off. Importantly, the orientation of fast and slow axis in their case was orthogonal to each other due to combination of amplitude distribution and polarisation of the field. EH_{12}-type modes are elongated along the major ellipse axis and a polarisation parallel to it represents the fast mode, i.e. the one with lesser effective index. HE_{13}-type modes expand along the minor axis and here the field polarised along the minor axis represents the fast mode. Qualitatively, the mode whose field exhibits a greater portion of normal components with respect to the core cladding boundary is associated with the fast axis and vice versa.

Due to the reduced core area the expected THG wavelengths reduced, whereas the modes of HE_{13}-type showed three times steeper dependence as they are closer to cut-off. The coupling constant of the EH_{12}-type was enhanced by more than one order of magnitude caused by the alignment of field vectors. Experimentally such an elliptical fibre with $\Delta = 60\,\text{nm}$ was deployed. Both harmonic wavelengths and modal shapes were found in good agreement with simulations and the field polarisation was confirmed as well as polarisation dependent wavelength shifts imposed by birefringence. Conversion efficiency of $2.8 \cdot 10^{-5}$ was achieved in C_2Cl_4.

Temperature dependence of phase matching was shown experimentally and is in agreement with calculations. Tuning rates of $0.1 - 0.2\,\text{nm/K}$ were obtained in a C_2Cl_4 fibre near to modal cut-off. Negative rates of the same order are expected in case of CS_2 due to larger contrast between core and cladding.

In addition, power handling capabilities of C_2Cl_4 and CS_2 filled LCFs were put to a test using a Thulium based fibre laser with 380 MHz repetition rate emitting 90 fs pulses centred at 1.9 μm. Highest average power supercontinuum generation from a 4.8 μm LCF was demonstrated at a level of 430 mW and 660 mW for CS_2 and C_2Cl_4, respectively. Excellent stability persisted for days without degradation. Average powers beyond one Watt were shown to be delivered via large core fibres which were limited by the pump power of the laser.

5.1 Outlook

Within the scope of this thesis conversion efficiencies of order 10^{-5} for C_2Cl_4 represent modest values compared to silica based platforms, ranging from 10^{-7} for similarly sized GeO_2 doped fibres up to 10^{-3} in small core MOF or taper. CS_2 filled fibres provided efficiencies of 10^{-7}. Potential for improvement and possible future research directions are provided below.

Pump conditions in the step index fibre geometry

In case of a 3.5 μm CS_2 LCF substantial improvement is expected for addressing the HE_{13} mode directly in the AD domain, exploiting solitary waves able to sustain their peak power for appreciable lengths [38].

Similarly an increase in core size and shift of λ_{PM} is possible for C_2Cl_4 which also due to the reduction of GVM compared to the present case holds promise of further enhancement. On the other hand, since capillary based LCF can be made meters long, pulse widths of several picoseconds allow to address a regime of negligible dispersion without the necessity of further GVD adjustments and should be addressed in future.

Active control and tuning

To exploit the tuning capabilities in THG, a temperature control system can be realised using miniature peltier elements. Such an implementation would allow tuning dispersion and phase mismatch curves along the fibre beyond linear gradients to potentially compensate for acquired mismatch due to nonlinear phase shifts.

The transfer of the recently shown mode conversion technique [31] to LCFs may enable progress towards realisation of correlated photon sources with reduced noise from spontaneous Raman scattering.

Fibre modification

Since phase matching is sensitive to core sizes, the case of restricted access to capillary fibres can be compensated to an extent by mixtures, which were formerly deployed to tune the GVD of LCFs [41,42].

Adjusting the core size along the fibre by either down or up tapering can assist if preferential tuning beyond the thermal tuning capacity is required. To this end, a particularly interesting configuration is an average core size chosen such that the phase matched wavelength and zero dispersion wavelength of the pump coincide. Axial

modulation of the core size then results in alternating GVD with potential to compensate dispersive broadening as demonstrated in silica fibres [143].

Beyond the step-index capillary the versatility of MOFs has yet to be explored – promising a rich variety of dispersive landscapes. Large air filling fractions in the photonic cladding and reduction in core size possibly enable phase matching to a HE_{12} mode with enhancement of the modal coupling constant. In an extreme case, utilising selective filling techniques [43], a suspended liquid column waveguide can be envisioned.

Effects beyond THG

The introduced elliptical fibres should provide a simple but effective platform to study polarisation related effects in LCFs which to date are largely unexplored. In particular polarisation mode instability was identified to limit coherence of supercontinua, i.e. their pulse to pulse stability, even in the normal dispersive domain [136]. The impact of the retarded response thus can be studied in such birefringent fibres.

Finally, a recently demonstrated effect called intermodal XPM was shown to induce soliton fission in silicon nitride ridge waveguides with instantaneous response [144]. Utilising birefringent LCF, these dynamics can be studied under the influence of a retarded response.

6   References

1.   F. Reiter, U. Graf, M. Schultze, W. Schweinberger, H. Schröder, N. Karpowicz, A. M. Azzeer, R. Kienberger, F. Krausz, and E. Goulielmakis, "Generation of sub-3 fs pulses in the deep ultraviolet," Opt. Lett. **35**(13), 2248–2250 (2010).

2.   F. Eilenberger, M. Bache, S. Minardi, and T. Pertsch, "Temporal switching induced by cascaded third order nonlinearity," Opt. Lett. **37**(24), 5109–5111 (2012).

3.   Y. Barad, H. Eisenberg, M. Horowitz, and Y. Silberberg, "Nonlinear scanning laser microscopy by third harmonic generation," Appl. Phys. Lett. **70**(8), 922–924 (1997).

4.   R. Genthial, E. Beaurepaire, M. C. Schanne-Klein, F. Peyrin, D. Farlay, C. Olivier, Y. Bala, G. Boivin, J. C. Vial, D. Débarre, and A. Gourrier, "Label-free imaging of bone multiscale porosity and interfaces using third-harmonic generation microscopy," Sci. Rep. **7**(1), 1–16 (2017).

5.   P. D. Maker, R. W. Terhune, M. Nisenoff, and C. M. Savage, "Effects of dispersion and focusing on the production of optical harmonics," Phys. Rev. Lett. **8**(1), 21–22 (1962).

6.   F. G. Omenetto, A. J. Taylor, M. D. Moores, J. Arriaga, J. C. Knight, W. J. Wadsworth, and P. S. J. Russell, "Simultaneous generation of spectrally distinct third harmonics in a photonic crystal fiber," Opt. Lett. **26**(15), 1158–1160 (2001).

7.   A. Efimov, A. Taylor, F. Omenetto, J. Knight, W. Wadsworth, and P. Russell, "Phase-matched third harmonic generation in microstructured fibers," Opt. Express **11**(20), 2567–2576 (2003).

8.   F. Omenetto, A. Efimov, A. Taylor, J. Knight, W. Wadsworth, and P. Russell, "Polarization dependent harmonic generation in microstructured fibers," Opt. Express **11**(1), 61–67 (2003).

9.   A. Efimov, A. Taylor, F. Omenetto, J. Knight, W. Wadsworth, and P. Russell, "Nonlinear generation of very high-order UV modes in microstructured fibers," Opt. Express **11**(8), 910–918 (2003).

10.   D. A. Akimov, A. A. Ivanov, A. N. Naumov, O. A. Kolevatova, M. V. Alfimov, T. A. Birks, W. J. Wadsworth, P. S. J. Russell, A. A. Podshivalov, and A. M. Zheltikov, "Generation of a spectrally asymmetric third harmonic with unamplified 30-fs

Cr:forsterite laser pulses in a tapered fiber," Appl. Phys. B **76**(5), 515–519 (2003).

11.   V. Grubsky and J. Feinberg, "Phase-matched third-harmonic UV generation using low-order modes in a glass micro-fiber," Opt. Commun. **274**(2), 447–450 (2007).

12.   V. Grubsky and A. Savchenko, "Glass micro-fibers for efficient third harmonic generation," Opt. Express **13**(18), 6798–6806 (2005).

13.   A. N. Naumov and A. M. Zheltikov, "Asymmetric spectral broadening and temporal evolution of cross-phase-modulated third-harmonic pulses," Opt. Express **10**(2), 122–127 (2002).

14.   A. M. Zheltikov, "Third-harmonic generation with no signal at 3 ω," Phys. Rev. A **72**(4), 043812 (2005).

15.   T. Lee, Y. Jung, C. A. Codemard, M. Ding, N. G. R. Broderick, and G. Brambilla, "Broadband third harmonic generation in tapered silica fibres," Opt. Express **20**(8), 8503–8511 (2012).

16.   S. C. Warren-Smith, K. Schaarschmidt, M. Chemnitz, E. P. Schartner, H. Schneidewind, H. Ebendorff-Heidepriem, and M. A. Schmidt, "Tunable multi-wavelength third-harmonic generation using exposed-core microstructured optical fiber," Opt. Lett. **44**(3), 626–629 (2019).

17.   K. Bencheikh, S. Richard, G. Mélin, G. Krabshuis, F. Gooijer, and J. A. Levenson, "Phase-matched third-harmonic generation in highly germanium-doped fiber," Opt. Lett. **37**(3), 289–291 (2012).

18.   A. B. Fedotov, A. A. Voronin, E. E. Serebryannikov, I. V. Fedotov, A. V. Mitrofanov, A. A. Ivanov, D. A. Sidorov-Biryukov, and A. M. Zheltikov, "Multifrequency third-harmonic generation by red-shifting solitons in a multimode photonic-crystal fiber," Phys. Rev. E - Stat. Nonlinear, Soft Matter Phys. **75**(1), 1–7 (2007).

19.   T. Cheng, X. Zhou, Y. Sun, X. Yan, X. Zhang, F. Wang, S. Li, T. Suzuki, and Y. Ohishi, "Supercontinuum-induced multi-wavelength third-harmonic generation in a suspended-core microstructured optical fiber," Opt. Express **28**(20), 28750–28761 (2020).

20.   F. van Beurden, D. M. van Willigen, B. Vojnovic, M. N. van Oosterom, O. R. Brouwer, H. G. va. der Poel, H. Kobayashi, F. W. B. van Leeuwen, and T. Buckle, "Multi-Wavelength Fluorescence in Image-Guided Surgery, Clinical Feasibility and Future

Perspectives," Mol. Imaging **19**, 1–18 (2020).

21. D. Chorvat and A. Chorvatova, "Multi-wavelength fluorescence lifetime spectroscopy: A new approach to the study of endogenous fluorescence in living cells and tissues," Laser Phys. Lett. **6**(3), 175–193 (2009).

22. M. Corona, K. Garay-Palmett, and A. B. U'Ren, "Experimental proposal for the generation of entangled photon triplets by third-order spontaneous parametric downconversion in optical fibers," Opt. Lett. **36**(2), 190–192 (2011).

23. M. Corona, K. Garay-Palmett, and A. B. U'Ren, "Third-order spontaneous parametric down-conversion in thin optical fibers as a photon-triplet source," Phys. Rev. A **84**(3), 033823 (2011).

24. S. Richard, K. Bencheikh, B. Boulanger, and J. A. Levenson, "Semiclassical model of triple photons generation in optical fibers," Opt. Lett. **36**(15), 3000–3002 (2011).

25. R. Ismaeel, T. Lee, M. Ding, N. G. R. Broderick, and G. Brambilla, "Nonlinear microfiber loop resonators for resonantly enhanced third harmonic generation," Opt. Lett. **37**(24), 5121–5123 (2012).

26. A. Borne, T. Katsura, C. Félix, B. Doppagne, P. Segonds, K. Bencheikh, J. A. Levenson, and B. Boulanger, "Anisotropy analysis of third-harmonic generation in a germanium-doped silica optical fiber," Opt. Lett. **40**(6), 982–985 (2015).

27. S. C. Warren-Smith, M. Chemnitz, H. Schneidewind, R. Kostecki, H. Ebendorff-Heidepriem, T. M. Monro, and M. A. Schmidt, "Nanofilm-induced spectral tuning of third harmonic generation," Opt. Lett. **42**(9), 1812–1815 (2017).

28. J. Hammer, A. Cavanna, R. Pennetta, M. V. Chekhova, P. S. J. Russell, and N. Y. Joly, "Dispersion tuning in sub-micron tapers for third-harmonic and photon triplet generation," Opt. Lett. **43**(10), 2320–2323 (2018).

29. A. Cavanna, F. Just, X. Jiang, G. Leuchs, M. V. Chekhova, P. St.J. Russell, and N. Y. Joly, "Hybrid photonic-crystal fiber for single-mode phase matched generation of third harmonic and photon triplets," Optica **3**(9), 952–955 (2016).

30. X. Jiang, D. Zhang, T. Lee, and G. Brambilla, "Optimized microfiber-based third-harmonic generation with adaptive control of phase mismatch," Opt. Lett. **43**(12), 2728–2731 (2018).

31. C. K. Ha, K. H. Nam, and M. S. Kang, "Efficient harmonic generation in an adiabatic

multimode submicron tapered optical fiber," Commun. Phys. **4**(1), 1–9 (2021).

32. M. I. M. A. Khudus, T. Lee, P. Horak, and G. Brambilla, "Effect of intrinsic surface roughness on the efficiency of intermodal phase matching in silica optical nanofibers," Opt. Lett. **40**(7), 1318 (2015).

33. S. Kedenburg, A. Steinmann, R. Hegenbarth, and T. Steinle, "Nonlinear refractive indices of nonlinear liquids : wavelength dependence and influence of retarded response," Appl. Phys. B **117**, 803–816 (2014).

34. M. Reichert, H. Hu, M. R. Ferdinandus, M. Seidel, P. Zhao, T. R. Ensley, D. Peceli, J. M. Reed, D. A. Fishman, S. Webster, D. J. Hagan, and E. W. Van Stryland, "Temporal, spectral, and polarization dependence of the nonlinear optical response of carbon disulfide," Optica **1**(6), 436–445 (2014).

35. P. Zhao, M. Reichert, S. Benis, D. J. Hagan, and E. W. Van Stryland, "Temporal and polarization dependence of the nonlinear optical response of solvents," Optica **5**(5), 583–594 (2018).

36. D. Churin, T. N. Nguyen, K. Kieu, R. A. Norwood, and N. Peyghambarian, "Mid-IR supercontinuum generation in an integrated liquid-core optical fiber filled with CS2," Opt. Mater. Express **3**(9), 1358–1364 (2013).

37. S. Kedenburg, T. Gissibl, T. Steinle, A. Steinmann, and H. Giessen, "Towards integration of a liquid-filled fiber capillary for supercontinuum generation in the 1.2–2.4 μm range," Opt. Express **23**(7), 8281–8289 (2015).

38. M. Chemnitz, M. Gebhardt, C. Gaida, F. Stutzki, J. Kobelke, J. Limpert, A. Tünnermann, and M. A. Schmidt, "Hybrid soliton dynamics in liquid-core fibres," Nat. Commun. **8**(42), 1–11 (2017).

39. M. Chemnitz, C. Gaida, M. Gebhardt, F. Stutzki, J. Kobelke, A. Tünnermann, J. Limpert, and M. A. Schmidt, "Carbon chloride-core fibers for soliton mediated supercontinuum generation," Opt. Express **26**(3), 3221–3235 (2018).

40. M. Chemnitz, R. Scheibinger, C. Gaida, M. Gebhardt, F. Stutzki, S. Pumpe, J. Kobelke, A. Tünnermann, J. Limpert, and M. A. Schmidt, "Thermodynamic control of soliton dynamics in liquid-core fibers," Optica **5**(6), 695–703 (2018).

41. S. Junaid, K. Schaarschmidt, M. Chemnitz, M. Chambonneau, S. Nolte, and M. A. Schmidt, "Tailoring modulation instabilities and four-wave mixing in dispersion-

managed composite liquid-core fibers," Opt. Express **28**(3), 3097–3106 (2020).

42. M. Chemnitz, S. Junaid, N. Walther, R. Scheibinger, K. Schaarschmidt, J. Kobelke, and M. Schmidt, "Tailoring soliton fission at telecom wavelengths using composite-liquid-core fibers," Opt. Lett. **45**(11), 2985–2988 (2020).

43. M. Vieweg, T. Gissibl, S. Pricking, B. T. Kuhlmey, D. C. Wu, B. J. Eggleton, and H. Giessen, "Ultrafast nonlinear optofluidics in selectively liquid-filled photonic crystal fibers," Opt. Express **18**(24), 25232–25240 (2010).

44. V. T. Hoang, R. Kasztelanic, A. Anuszkiewicz, G. Stepniewski, A. Filipkowski, S. Ertman, D. Pysz, T. Wolinski, K. D. Xuan, M. Klimczak, and R. Buczynski, "All-normal dispersion supercontinuum generation in photonic crystal fibers with large hollow cores infiltrated with toluene," Opt. Mater. Express **8**(11), 3568–3582 (2018).

45. V. T. Hoang, R. Kasztelanic, A. Filipkowski, G. Stępniewski, D. Pysz, M. Klimczak, S. Ertman, V. C. Long, T. R. Woliński, M. Trippenbach, K. D. Xuan, M. Śmietana, and R. Buczyński, "Supercontinuum generation in an all-normal dispersion large core photonic crystal fiber infiltrated with carbon tetrachloride," Opt. Mater. Express **9**(5), 2264–2278 (2019).

46. V. T. Hoang, R. Kasztelanic, G. Stępniewski, K. D. Xuan, V. C. Long, M. Trippenbach, M. Klimczak, R. Buczyński, and J. Pniewski, "Femtosecond supercontinuum generation around 1560 nm in hollow-core photonic crystal fibers filled with carbon tetrachloride," Appl. Opt. **59**(12), 3720–3725 (2020).

47. S. Pumpe, M. Chemnitz, J. Kobelke, and M. A. Schmidt, "Monolithic optofluidic mode coupler for broadband thermo-and piezo-optical characterization of liquids," Opt. Express **25**(19), 22932–22946 (2017).

48. C. Conti, M. A. Schmidt, P. S. J. Russell, and F. Biancalana, "Highly noninstantaneous solitons in liquid-core photonic crystal fibers," Phys. Rev. Lett. **105**(26), 1–4 (2010).

49. M. Chemnitz, M. Gebhardt, C. Gaida, F. Stutzki, J. Kobelke, J. Limpert, A. Tünnermann, and M. A. Schmidt, "Hybrid soliton dynamics in liquid-core fibres Supplementary Note 1 : Reinvestigation of Refractive Index Dispersion of Carbon Disulfide Supplementary Note 2 : Impact of Model Uncertainties on Simulation

Results," Nat. Commun. **8**(42), (2017).

50. R. Vasantha Jayakantha Raja, A. Husakou, J. Hermann, and K. Porsezian, "Supercontinuum generation in liquid-filled photonic crystal fiber with slow nonlinear response," J. Opt. Soc. Am. B **27**(9), 1763–1768 (2010).

51. M. Barbier, I. Zaquine, and P. Delaye, "Spontaneous four-wave mixing in liquid-core fibers: Towards fibered Raman-free correlated photon sources," New J. Phys. **17**, 053031 (2015).

52. M. Cordier, A. Orieux, R. Gabet, T. Harlé, N. Dubreuil, E. Diamanti, P. Delaye, and I. Zaquine, "Raman-tailored photonic crystal fiber for telecom band photon-pair generation," Opt. Lett. **42**(13), 2583–2586 (2017).

53. A. Sudirman and W. Margulis, "All-Fiber Optofluidic Component to Combine Light and Fluid," IEEE Photonics Technol. Lett. **26**(10), 1031–1033 (2014).

54. L. Xiao, N. V Wheeler, N. Healy, and A. C. Peacock, "Integrated hollow-core fibers for nonlinear optofluidic applications," Opt. Express **21**(23), 28751–28757 (2013).

55. K. Kieu, L. Schneebeli, R. A. Norwood, and N. Peyghambarian, "Integrated liquid-core optical fibers for ultra- efficient nonlinear liquid photonics," Opt. Express **20**(7), 8148–8154 (2012).

56. D. Lopez-Cortes, O. Tarasenko, and W. Margulis, "All-fiber Kerr cell," Opt. Lett. **37**(15), 3288–3290 (2012).

57. R. M. Gerosa, A. Sudirman, L. de S. Menezes, W. Margulis, and C. J. S. de Matos, "All-fiber high repetition rate microfluidic dye laser," Optica **2**(2), 186–193 (2015).

58. M. Chemnitz and M. A. Schmidt, "Verfahren zur Herstellung von vollständig System-integrierbaren Flüssig-Kern-Fasern und deren Verwendung," U.S. patent DE102018115194A (2018).

59. R. W. Boyd, "Chapter 1 - The Nonlinear Optical Susceptibility," in *Nonlinear Optics (Fourth Edition)*, R. W. Boyd, ed., Fourth Edi (Academic Press, 2020), pp. 1–64.

60. R. L. Sutherland, *Handbook of Nonlinear Optics* (1997), **36**(3).

61. F. Zernike and J. E. Midwinter, *Applied Nonlinear Optics* (Joh Wiley, 1973).

62. G. Agrawal, "Chapter 2 - Pulse Propagation in Fibers," in *Nonlinear Fiber Optics*

(Fifth Edition), G. Agrawal, ed., Fifth Edit, Optics and Photonics (Academic Press, 2013), pp. 27–56.

63. C. Yeh and F. I. Shimabukuro, *The Essence of Dielectric Waveguides*, 1st ed. (Springer US, 2008).

64. A. W. Snyder and J. D. Love, *Optical Waveguide Theory*, 2nd ed. (Chapman and Hall, 1983).

65. K. Okamoto, *Fundamentals of Optical Waveguides*, 2nd ed. (Elsevier, 2006).

66. P. L. François, "Nonlinear propagation of ultrashort pulses in optical fibers: total field formulation in the frequency domain," J. Opt. Soc. Am. B **8**(2), 276–293 (1991).

67. M. Kolesik and J. V. Moloney, "Nonlinear optical pulse propagation simulation: From Maxwell's to unidirectional equations," Phys. Rev. E **70**(3), 036604 (2004).

68. A. Couairon, E. Brambilla, T. Corti, D. Majus, O. de, and M. Kolesik, "Practitioner's guide to laser pulse propagation models and simulation," Eur. Phys. J. Spec. Top. **199**(1), 5–76 (2011).

69. J. M. Dudley, G. Genty, and S. Coen, "Supercontinuum generation in photonic crystal fiber," Rev. Mod. Phys. **78**(4), 1135–1184 (2006).

70. D. V. Skryabin and A. V. Gorbach, "Colloquium: Looking at a soliton through the prism of optical supercontinuum," Rev. Mod. Phys. **82**(2), 1287–1299 (2010).

71. A. V. Husakou and J. Herrmann, "Supercontinuum generation of higher-order solitons by fission in photonic crystal fibers," Phys. Rev. Lett. **87**(20), 203901-1-203901–4 (2001).

72. B. Kibler, J. M. Dudley, and S. Coen, "Supercontinuum generation and nonlinear pulse propagation in photonic crystal fiber: Influence of the frequency-dependent effective mode area," Appl. Phys. B Lasers Opt. **81**(2–3), 337–342 (2005).

73. J. Laegsgaard, "Mode profile dispersion in the generalised nonlinear Schrödinger equation," Opt. Express **15**(24), 16110–16123 (2007).

74. A. M. Zheltikov, "Let there be white light: Supercontinuum generation by ultrashort laser pulses," Physics-Uspekhi **49**(6), 605–628 (2006).

75. G. P. Agrawal, *Nonlinear Fiber Optics*, 5th ed. (Elsevier, 2013).

76. J. M. Dudley and J. R. Taylor, eds., *Supercontinuum Generation in Optical Fibers* (Cambridge University Press, 2010).

77. R. R. Alfano, *The Supercontinuum Laser Source*, 3rd ed. (Springer New York, 2016).

78. J. C. Travers, M. H. Frosz, and J. M. Dudley, "Nonlinear fibre optics overview," in *Supercontinuum Generation in Optical Fibers*, J. M. Dudley and J. R. Taylor, eds. (Cambridge University, 2010), pp. 32–51.

79. A. M. Heidt, "Efficient Adaptive Step Size Method for the Simulation of Supercontinuum Generation in Optical Fibers," J. Light. Technol. **27**(18), 3984–3991 (2009).

80. A. A. Rieznik, A. M. Heidt, P. G. König, V. A. Bettachini, and D. F. Grosz, "Optimum integration procedures for supercontinuum simulation," IEEE Photonics J. **4**(2), 552–560 (2012).

81. J. Hult, "A fourth-order Runge-Kutta in the interaction picture method for simulating supercontinuum generation in optical fibers," J. Light. Technol. **25**(12), 3770–3775 (2007).

82. S. Roy, S. K. Bhadra, and G. P. Agrawal, "Dispersive wave generation in supercontinuum process inside nonlinear microstructured fibre," Curr. Sci. **100**(3), 321–342 (2011).

83. G. P. Agrawal, "Chapter 5 - Optical Solitons," in *Nonlinear Fiber Optics (Fifth Edition)*, G. Agrawal, ed., Fifth Edit, Optics and Photonics (Academic Press, 2013), pp. 129–191.

84. D. McMorrow, W. T. Lotshaw, and G. A. Kenney-wallace, "Femtosecond Optical Kerr Studies on the Origin of the Nonlinear Responses in Simple Liquids," J. Quantum Electron. **24**(2), 443–454 (1988).

85. G. Agrawal, "Chapter 4 - Self-Phase Modulation," in *Nonlinear Fiber Optics (Fifth Edition)*, G. Agrawal, ed., Fifth Edit, Optics and Photonics (Academic Press, 2013), pp. 87–128.

86. S. Pricking and H. Giessen, "Generalized retarded response of nonlinear media and its influence on soliton dynamics," Opt. Express **19**(4), 2895–2903 (2011).

87. M. Reichert, H. Hu, M. R. Ferdinandus, M. Seidel, P. Zhao, T. R. Ensley, D. Peceli, J. M. Reed, D. A. Fishman, S. Webster, D. J. Hagan, and E. W. Van Stryland, "Temporal,

spectral, and polarization dependence of the nonlinear optical response of carbon disulfide: erratum," Optica **3**(6), 657–658 (2016).

88. D. J. Hagan, S. Tofighi, S. Benis, H.-J. Chang, R. M. O'Donnell, J. Shi, M. V Bondar, and E. W. Van Stryland, "Characterization of the ultrafast nonlinear response of new organic compounds," in *Organic Photonic Materials and Devices XXII*, C. E. Tabor, F. Kajzar, and T. Kaino, eds. (SPIE, 2020), **11277**, pp. 37–48.

89. R. H. Stolen, W. J. Tomlinson, H. A. Haus, and J. P. Gordon, "Raman response function of silica-core fibers," J. Opt. Soc. Am. B **6**(6), 1159–1166 (1989).

90. Tzer-Hsiang Huang, Chia-Chen Hsu, Tai-Huei Wei, Springfield Chang, Shih-Ming Yen, Chi-Pin Tsai, Ray-Tang Liu, Chie-Tong Kuo, Wan-Sun Tse, and Chihta Chia, "The transient optical Kerr effect of simple liquids studied with an ultrashort laser with variable pulsewidth," IEEE J. Sel. Top. Quantum Electron. **2**(3), 756–768 (1996).

91. I. A. Heisler, R. R. B. Correia, T. Buckup, S. L. S. Cunha, and N. P. Da Silveira, "Time-resolved optical Kerr-effect investigation on CS 2/polystyrene mixtures," J. Chem. Phys. **123**, 054509 (2005).

92. D. Mcmorrow, N. Thantu, V. Kleiman, J. S. Melinger, and W. T. Lotshaw, "Analysis of Intermolecular Coordinate Contributions to Third-Order Ultrafast Spectroscopy of Liquids in the Harmonic Oscillator Limit," J. Phys. Chem. A **105**(34), 7960–7972 (2001).

93. M. Sheik-Bahae, A. A. Said, T.-H. Wei, D. J. Hagan, and E. W. Van Stryland, "Sensitive measurement of optical nonlinearities using a single beam," IEEE J. Quantum Electron. **26**(4), 760–769 (1990).

94. R. Stolen and J. Bjorkholm, "Parametric amplification and frequency conversion in optical fibers," IEEE J. Quantum Electron. **18**(7), 1062–1072 (1982).

95. A. Coillet and P. Grelu, "Third-harmonic generation in optical microfibers: From silica experiments to highly nonlinear glass prospects," Opt. Commun. **285**(16), 3493–3497 (2012).

96. T. Lee, "Nonlinear Properties of Optical Microfibres," PhD Thesis, University of Southampton, Faculty of Physical Sciences and Engineering (2013).

97. E. M. Dianov, P. V Mamyshev, A. M. Prokhorov, and S. V Chernikov, "Compression

of laser pulses based on the phase cross-modulation effect in fiber waveguides," Sov. J. Quantum Electron. **18**(10), 1211–1212 (1988).

98. N. I. Koroteev and A. M. Zheltikov, "Chirp control in third-harmonic generation due to cross-phase modulation," Appl. Phys. B Lasers Opt. **67**(1), 53–57 (1998).

99. A. M. Zheltikov, N. I. Koroteev, and A. N. Naumov, "Self- and cross-phase modulation accompanying third-harmonic generation in a hollow waveguide," J. Exp. Theor. Phys. **88**(5), 857–867 (1999).

100. F. Kajzar and J. Messier, "Third-harmonic generation in liquids," Phys. Rev. A **32**(4), 2352–2363 (1985).

101. G. R. Meredith, B. Buchalter, and C. Hanzlik, "Third-order susceptibility determination by third harmonic generation II," J. Chem. Phys. **78**(3), 15431551 (1983).

102. G. R. Meredith, B. Buchalter, and C. Hanzlik, "Third-order optical susceptibility determination by third harmonic generation I," J. Chem. Phys. **78**(3), 1533–1542 (1983).

103. I. Rau, F. Kajzar, J. Luc, B. Sahraoui, and G. Boudebs, "Comparison of Z-scan and THG derived nonlinear index of refraction in selected organic solvents," J. Opt. Soc. Am. B **25**(10), 1738–1747 (2008).

104. A. W. Snyder and D. J. Mitchell, "Accessible solitons," Science (80-.). **276**(5318), 1538 (1997).

105. W. Królikowski, O. Bang, N. I. Nikolov, D. Neshev, J. Wyller, J. J. Rasmussen, and D. Edmundson, "Modulational instability, solitons and beam propagation in spatially nonlocal nonlinear media," J. Opt. B Quantum Semiclassical Opt. **6**(5), (2004).

106. A. Alberucci, C. P. Jisha, and G. Assanto, "Breather solitons in highly nonlocal media," J. Opt. (United Kingdom) **18**(12), (2016).

107. A. M. Zheltikov, "Understanding the nonlinear phase and frequency shift of an ultrashort light pulse induced by an inertial third-order optical nonlinearity," Phys. Rev. A - At. Mol. Opt. Phys. **79**(2), 1–7 (2009).

108. S. Junaid, J. Bierlich, A. Hartung, T. Meyer, M. Chemnitz, and M. A. Schmidt, "Supercontinuum generation in a carbon disulfide core microstructured optical fiber," Opt. Express **29**(13), 19891–19902 (2021).

109. J. P. Gordon, "Theory of the soliton self-frequency shift," Opt. Lett. **11**(10), 662–664 (1986).

110. F. M. Mitschke and L. F. Mollenauer, "Discovery of the soliton self-frequency shift," Opt. Lett. **11**(10), 659–661 (1986).

111. B. Y. Hu, "Kramers–Kronig in two lines," Am. J. Phys. **57**(9), 821–821 (1989).

112. G. P. Agrawal, P. L. Baldeck, and R. R. Alfano, "Temporal and spectral effects of cross-phase modulation on copropagating ultrashort pulses in optical fibers," Phys. Rev. A **40**(9), 5063–5072 (1989).

113. Y. Sato, R. Morita, and M. Yamashita, "Femtosecond optical pulse compressor using CS2 liquid-core fiber with negative delayed nonlinear response," Japanese J. Appl. Physics, Part 1 Regul. Pap. Short Notes Rev. Pap. **36**(11), 6768–6774 (1997).

114. J. Satsuma and N. Yajima, "B. Initial Value Problems of One-Dimensional Self-Modulation of Nonlinear Waves in Dispersive Media," Prog. Theor. Phys. Suppl. **55**(55), 284–306 (1974).

115. N. N. . Akhmediev and V. I. Korneev, "Modulation instability and periodic solutions of the nonlinear Schrodinger equation," Theor. Math. Phys. **69**(2), 1089–1093 (1986).

116. M. Chemnitz, "Soliton Dynamics in Liquid-core Optical Fibers," PhD Thesis, Friedrich Schiller University Jena, Faculty of Physics and Astronomy (2018).

117. G. Agrawal, "Chapter 12 - Novel Nonlinear Phenomena," in *Nonlinear Fiber Optics (Fifth Edition)*, G. Agrawal, ed., Fifth Edit, Optics and Photonics (Academic Press, 2013), pp. 497–552.

118. K. Schaarschmidt, J. Kobelke, S. Nolte, T. Meyer, and M. A. Schmidt, "Ultrafast intermodal third harmonic generation in a liquid core step-index fiber filled with C2Cl4," Opt. Express **28**(17), 25037–25047 (2020).

119. G. Fanjoux, A. Sudirman, J.-C. Beugnot, L. Furfaro, W. Margulis, and T. Sylvestre, "Stimulated Raman-Kerr scattering in an integrated nonlinear optofluidic fiber arrangement," Opt. Lett. **39**(18), 5407–5410 (2014).

120. G. Fanjoux, S. Margueron, J.-C. Beugnot, and T. Sylvestre, "Supercontinuum generation by stimulated Raman–Kerr scattering in a liquid-core optical fiber," J. Opt. Soc. Am. B **34**(8), 1677–1683 (2017).

121. L. C. Van, V. T. Hoang, V. C. Long, K. Borzycki, K. D. Xuan, V. T. Quoc, M. Trippenbach, R. Buczyński, and J. Pniewski, "Supercontinuum generation in photonic crystal fibers infiltrated with nitrobenzene," Laser Phys. **30**(3), (2020).

122. M. Plidschun, M. Chemnitz, and M. A. Schmidt, "Low-loss deuterated organic solvents for visible and near-infrared photonics," Opt. Mater. Express **7**(4), 1122–1130 (2017).

123. M. Reichert, P. Zhao, J. M. Reed, T. R. Ensley, D. J. Hagan, and E. W. Van Stryland, "Beam deflection measurement of bound-electronic and rotational nonlinear refraction in molecular gases: erratum," Opt. Express **24**(17), 19122 (2016).

124. P. Zhao, M. Reichert, T. R. Ensley, W. M. Shensky, A. G. Mott, D. J. Hagan, and E. W. Van Stryland, "Nonlinear refraction dynamics of solvents and gases," Nonlinear Freq. Gener. Convers. Mater. Devices, Appl. XV **9731**, 97310F (2016).

125. D. Hollenbeck and C. D. Cantrell, "Multiple-vibrational-mode model for fiber-optic Raman gain spectrum and response function," J. Opt. Soc. Am. B **19**(12), 2886–2892 (2002).

126. I. H. Malitson, "Interspecimen Comparison of the Refractive Index of Fused Silica*,†," J. Opt. Soc. Am. **55**(10), 1205–1209 (1965).

127. A. A. Ivanov, D. Lorenc, I. Bugar, F. Uherek, E. E. Serebryannikov, S. O. Konorov, M. V. Alfimov, D. Chorvat, and A. M. Zheltikov, "Multimode anharmonic third-order harmonic generation in a photonic-crystal fiber," Phys. Rev. E - Stat. Nonlinear, Soft Matter Phys. **73**(1), 1–7 (2006).

128. S. C. Warren-Smith, J. Wie, M. Chemnitz, M. A. Schmidt, R. Kostecki, H. Ebendorff-Heidepriem, and T. M. Monro, "Third harmonic generation in exposed-core microstructured optical fibers," Opt. Express **24**(16), 17860–17867 (2016).

129. J. Santhanam and G. P. Agrawal, "Raman-induced spectral shifts in optical fibers: general theory based on the moment method," Opt. Commun. **222**(1–6), 413–420 (2003).

130. K. Schaarschmidt, H. Xuan, J. Kobelke, M. Chemnitz, I. Hartl, and M. A. Schmidt, "Long-term stable supercontinuum generation and watt-level transmission in liquid-core optical fibers," Opt. Lett. **44**(9), 2236–2239 (2019).

131. J. Meister, S. Diemer, R. Jung, S. Klein, W. Fuss, and P. Hering, "Liquid-core fused

silica capillary lightguides for applications in the UV/VIS and NIR spectral range," in *BiOS'97, Part of ...*, A. Katzir and J. A. Harrington, eds. (1997), **2977**, pp. 58–66.

132. S. Diemer, J. Meister, R. Jung, S. Klein, M. Haisch, W. Fuss, and P. Hering, "Liquid-core light guides for near-infrared applications.," Appl. Opt. **36**(34), 9075–9082 (1997).

133. K. Schaarschmidt, J. Kobelke, T. Meyer, M. Chemnitz, and M. Schmidt, "Third Harmonic Generation with Tailored Modes in Liquid Core Fibers with Geometric Birefringence," Opt. Lett. **45**(24), 6859–6862 (2020).

134. Z. Zhu and T. G. Brown, "Polarization properties of supercontinuum spectra generated in birefringent photonic crystal fibers," J. Opt. Soc. Am. B **21**(2), 249–257 (2004).

135. H. Tu, Y. Liu, X. Liu, D. Turchinovich, J. Lægsgaard, and S. A. Boppart, "Nonlinear polarization dynamics in a weakly birefringent all-normal dispersion photonic crystal fiber: toward a practical coherent fiber supercontinuum laser," Opt. Express **20**(2), 1113–1128 (2012).

136. I. B. Gonzalo, R. D. Engelsholm, M. P. Sørensen, and O. Bang, "Polarization noise places severe constraints on coherence of all-normal dispersion femtosecond supercontinuum generation," Sci. Rep. **8**(1), 1–13 (2018).

137. A. Antikainen, R.-J. Essiambre, and G. P. Agrawal, "Determination of modes of elliptical waveguides with ellipse transformation perturbation theory," Optica **4**(12), 1510–1513 (2017).

138. R. B. Dyott, R. B. Dyott, J. R. Cozens, and D. G. Morris, "Preservation of polarisation in optical-fibre waveguides with elliptical cores," Electron. Lett. **15**(13), 380–382 (1979).

139. D. Gloge, "Weakly Guiding Fibers," Appl. Opt. **10**(10), 2252 (1971).

140. U. T. Schwarz, M. A. Bandres, and J. C. Gutiérrez-Vega, "Observation of Ince–Gaussian modes in stable resonators," Opt. Lett. **29**(16), 1870–1872 (2004).

141. A. Borne, T. Katsura, C. Félix, B. Doppagne, P. Segonds, K. Bencheikh, J. A. Levenson, and B. Boulanger, "Ince-gauss based multiple intermodal phase-matched third-harmonic generations in a step-index silica optical fiber," Opt. Commun. **358**, 160–163 (2016).

142. R. Scheibinger, N. M. Lüpken, M. Chemnitz, K. Schaarschmidt, J. Kobelke, C. Fallnich, and M. A. Schmidt, "Higher-order mode supercontinuum generation in dispersion-engineered liquid-core fibers," Sci. Rep. **11**(1), 5270 (2021).

143. H. Zia, N. M. Lüpken, T. Hellwig, C. Fallnich, and K. J. Boller, "Supercontinuum Generation in Media with Sign-Alternated Dispersion," Laser Photonics Rev. **14**(7), 1–11 (2020).

144. N. M. Lüpken, M. Timmerkamp, R. Scheibinger, K. Schaarschmidt, M. A. Schmidt, K. Boller, and C. Fallnich, "Numerical and Experimental Demonstration of Intermodal Dispersive Wave Generation," Laser Photon. Rev. **2100125**, 2100125 (2021).

Attachments

Acknowledgements

Publication List

1. **K. Schaarschmidt**, S. Weidlich, D. Reul, and M. A. Schmidt, "Bending losses and modal properties of nano-bore optical fibers," Opt. Lett. **43**(17), 4192–4195 (2018).

2. S. Jiang, **K. Schaarschmidt**, S. Weidlich, and M. A. Schmidt, "Fiber-Integrated Absorption Spectroscopy Using Liquid-Filled Nanobore Optical Fibers," J. Light. Technol. **36**(18), 3970–3975 (2018).

3. **K. Schaarschmidt**, M. Chemnitz, R. Scheibinger, and M. A. Schmidt, "Third Harmonic Generation with Ultrashort Pulses in a C2Cl4 filled Liquid Core Fiber," in *2019 Conference on Lasers and Electro-Optics Europe and European Quantum Electronics Conference* (Optical Society of America, 2019), p. cd_12_3.

4. **K. Schaarschmidt**, H. Xuan, J. Kobelke, M. Chemnitz, I. Hartl, and M. A. Schmidt, "Long-term stable supercontinuum generation and watt-level transmission in liquid-core optical fibers," Opt. Lett. **44**(9), 2236–2239 (2019).

5. S. C. Warren-Smith, **K. Schaarschmidt**, M. Chemnitz, E. P. Schartner, H. Schneidewind, H. Ebendorff-Heidepriem, and M. A. Schmidt, "Tunable multi-wavelength third-harmonic generation using exposed-core microstructured optical fiber," Opt. Lett. **44**(3), 626–629 (2019).

6. **K. Schaarschmidt**, J. Kobelke, T. Meyer, M. Chemnitz, and M. Schmidt, "Third Harmonic Generation with Tailored Modes in Liquid Core Fibers with Geometric Birefringence," Opt. Lett. **45**(24), 6859–6862 (2020).

7. **K. Schaarschmidt**, J. Kobelke, S. Nolte, T. Meyer, and M. A. Schmidt, "Ultrafast intermodal third harmonic generation in a liquid core step-index fiber filled with C2Cl4," Opt. Express **28**(17), 25037–25047 (2020).

8. S. Junaid, **K. Schaarschmidt**, M. Chemnitz, M. Chambonneau, S. Nolte, and M. A. Schmidt, "Tailoring modulation instabilities and four-wave mixing in dispersion-managed composite liquid-core fibers," Opt. Express **28**(3), 3097–3106 (2020).

9. M. Chemnitz, S. Junaid, N. Walther, R. Scheibinger, **K. Schaarschmidt**, J. Kobelke, and M. Schmidt, "Tailoring soliton fission at telecom wavelengths using composite-liquid-core fibers," Opt. Lett. **45**(11), 2985–2988 (2020).

10. T. A. K. Lühder, **K. Schaarschmidt**, S. Goerke, E. P. Schartner, H. Ebendorff-Heidepriem, and M. A. Schmidt, "Resonance-Induced Dispersion Tuning for Tailoring Nonsolitonic Radiation via Nanofilms in Exposed Core Fibers," Laser Photonics Rev. **1900418**, (2020).

11. X. Qi, **K. Schaarschmidt**, M. Chemnitz, and M. A. Schmidt, "Essentials of resonance-enhanced soliton-based supercontinuum generation," Opt. Express **28**(2), 2557–2571 (2020).

12. N. M. Lüpken, M. Timmerkamp, R. Scheibinger, **K. Schaarschmidt**, M. A. Schmidt, K. Boller, and C. Fallnich, "Numerical and Experimental Demonstration of Intermodal Dispersive Wave Generation," Laser Photon. Rev. **2100125**, 2100125 (2021).

13. R. Scheibinger, N. M. Lüpken, M. Chemnitz, **K. Schaarschmidt**, J. Kobelke, C. Fallnich, and M. A. Schmidt, "Higher-order mode supercontinuum generation in dispersion-engineered liquid-core fibers," Sci. Rep. **11**(1), 5270 (2021).

14. X. Qi, **K. Schaarschmidt**, G. Li, S. Junaid, R. Scheibinger, T. Lühder, and M. A. Schmidt, "Understanding Nonlinear Pulse Propagation in Liquid Strand-Based Photonic Bandgap Fibers," Crystals **11**(305), 1–11 (2021).

Ehrenwörtliche Erklärung

Ich erkläre hiermit ehrenwörtlich, dass ich die vorliegende Arbeit selbständig, ohne unzulässige Hilfe Dritter und ohne Benutzung anderer als der angegebenen Hilfsmittel und Literatur angefertigt habe. Die aus anderen Quellen direkt oder indirekt übernommenen Daten und Konzepte sind unter Angabe der Quelle gekennzeichnet.

Bei der Auswahl und Auswertung folgenden Materials haben mir die nachstehend aufgeführten Personen in der jeweils beschriebenen Weise entgeltlich/unentgeltlich geholfen:

1.   Franka Jahn: Elektronenmikroskopie Aufnahmen und Vermessung von Kapillarfasern

Weitere Personen waren an der inhaltlich-materiellen Erstellung der vorliegenden Arbeit nicht beteiligt. Insbesondere habe ich hierfür nicht die entgeltliche Hilfe von Vermittlungs- bzw. Beratungsdiensten (Promotionsberater oder andere Personen) in Anspruch genommen. Niemand hat von mir unmittelbar oder mittelbar geldwerte Leistungen für Arbeiten erhalten, die im Zusammenhang mit dem Inhalt der vorgelegten Dissertation stehen.

Die Arbeit wurde bisher weder im In- noch im Ausland in gleicher oder ähnlicher Form einer anderen Prüfungsbehörde vorgelegt.

Die geltende Promotionsordnung der Physikalisch-Astronomischen Fakultät ist mir bekannt.

Ich versichere ehrenwörtlich, dass ich nach bestem Wissen die reine Wahrheit gesagt und nichts verschwiegen habe.

Ort, Datum   Kay Schaarschmidt